DOI: 10.15388/vu.thesis.354
https://orcid.org/0000-0001-6492-7540

VILNIUS UNIVERSITY
CENTER FOR PHYSICAL SCIENCES AND TECHNOLOGY

Kornelijus Pūkas

Technologies of dosimetry in applications of high energy physics and radiation medicine

DOCTORAL DISSERTATION

Technological Sciences,
Material Engineering (T 008)

VILNIUS 2022

The dissertation was prepared between 2019 and 2022 at Institute of Photonics and Nanotechnology, Vilnius University.

Academic Supervisor – Prof. Habil. Dr. Eugenijus Gaubas (Vilnius University, Technological Sciences, Material Engineering, T 008).
Academic Consultant – Dr. Tomas Čeponis (Vilnius University, Technological Sciences, Material Engineering, T 008).

This doctoral dissertation will be defended in a public meeting of the Dissertation Defence Panel:

Chairman – Prof. Dr. Vincas Tamošiunas ((Vilnius University, Technological Sciences, Material Engineering, T 008).
Members:
Prof. Dr. Sc., Arturs Medvids (Riga Technical university, Technological Sciences, Material Engineering, T 008),
Assoc. Prof. Dr. Artūras Plūkis (Center for Physical Sciences and Technology, Technological Sciences, Material Engineering, T 008),
Assoc. Prof. Dr. Tomas Šalkus (Vilnius university, Technological Sciences, Material Engineering, T 008),
Dr. Aldis Šilėnas (Center for Physical Sciences and Technology, Natural Sciences, Physics, N 002).

The dissertation shall be defended at a public meeting of the Dissertation Defence Panel at 16:00 o'clock on 7th of October 2022 in "Didžioji Fizikos Auditorija" of the Faculty of Physics, Vilnius University.
Address: Saulėtekio av. 9, Faculty of Physics, Vilnius University, Room "Didžioji Fizikos Auditorija", Vilnius, Lithuania
Tel. +37052366000; e-mail: ff@ff.vu.lt

The text of this dissertation can be accessed at the libraries of Vilnius University as well as on the website of Vilnius University:
www.vu.lt/lt/naujienos/ivykiu-kalendorius

DOI: 10.15388/vu.thesis.354
https://orcid.org/0000-0001-6492-7540

VILNIAUS UNIVERSITETAS
FIZINIŲ IR TECHNOLOGIJOS MOKSLŲ CENTRAS

Kornelijus Pūkas

Dozimetrijos technologijos aukštųjų energijų fizikos ir radiacinės medicinos taikymams

DAKTARO DISERTACIJA

Technologijos mokslai,
Medžiagų inžinerija (T 008)

VILNIUS 2022

Disertacija rengta 2019 – 2022 metais Fotonikos ir Nanotechnologijų institute, Vilniaus universitete.

Mokslinis vadovas – prof. habil. dr. Eugenijus Gaubas (Vilniaus universitetas, technologijos mokslai, medžiagų inžinerija, T 008).
Mokslinis konsultantas – dr. Tomas Čeponis (Vilniaus universitetas, technologijos mokslai, medžiagų inžinerija, T 008).

Gynimo taryba:
Pirmininkas (-ė) – prof. dr. Vincas Tamošiūnas (Vilniaus universitetas, technologijos mokslai, medžiagų inžinerija, T 008).
Nariai:
prof. habil. dr. Arturs Medvids (Rygos Technikos universitetas, technologijos mokslai, medžiagų inžinerija, T 008),
doc. dr. Artūras Plūkis (Fizinių ir technologijos mokslų centras, technologijos mokslai, medžiagų inžinerija, T 008),
doc. dr. Tomas Šalkus (Vilniaus universitetas, technologijos mokslai, medžiagų inžinerija, T 008),
dr. Aldis Šilėnas (Fizinių ir technologijos mokslų centras, gamtos mokslai, fizika, N 002).

Disertacija ginama viešame Gynimo tarybos posėdyje 2022 m. spalio mėn. 7 d. 16 val. Vilniaus universiteto Fizikos fakulteto Didžiojoje fizikos auditorijoje.
Adresas: Saulėtekio al. 9, Vilniaus universiteto Fizikos Fakultetas, Didžioji Fizikos Auditorija, Vilnius, Lietuva
Tel. +37052366000 ; el. paštas ff@ff.vu.lt

Disertaciją galima peržiūrėti VU bibliotekose ir VU interneto svetainėje adresu: *https://www.vu.lt/naujienos/ivykiu-kalendorius*

ABBREVIATIONS

AT – Ammono-Thermal
BELIV – Barrier evaluation by linearly increasing voltage
CCE – charge collection efficiency
CERN - European Organization for Nuclear Research
CT – computed tomography
CZ – Czochralski pulling technique
DD - Drift-Diffusion
DLTS – Deep Level Transient Spectroscopy
DUT – device under test
ELOG – Epitaxial lateral overgrown
EM – electromagnetic
GLIV – generator of linearly increasing voltage
HVPE – Hydride Vapor Phase Epitaxy
LED – light emitting diode
LGAD – Low Gain Avalanche Diodes
LHC – large hadron collider
MC-DLT – minority carrier deep level transient spectroscopy
MCT – minority carrier transients
MOCVD - Metal-Organic Chemical Vapour Deposition
MOSFET – metal oxide field effect transistor
MW-PCT – microwave probed photoconductivity transient
NAS - National Academy of Science
NIEL – non-ionizing energy loss
OPO – optical parametric oscillators
OSLD – optical stimulated luminescence dosimeter
PCB – printed circuit board
PL – photoluminescence
RPVD – remote position verification devices
SP-MRC - Scientific-Practical Materials Research Centre
SS -steady state
SS-PIS – steady-state photo-ionization spectroscopy
TCAD - Technology Computer-Aided Design
TCT – Transient Current Technique
TI – time integration
TLD – thermo-luminescence dosimeter
TR – time resolved
UV – ultraviolet

CONTENT

INTRODUCTION

Research problem. Development of nowadays particle sensors intended for high energy physics experiments [1, 2] is addressed to increase of detector radiation hardness, to speeding-up of sensor response, to enhancement of sensor internal amplification, to advanced design of detector structure. In many experiments of high energy physics at European Organization for Nuclear Research (CERN) [3], high resistivity Si particle detectors of *pin* structure are employed for tracking of the ionizing particles. These detectors should be capable to survive radiation fluences up to 10^{17} cm^{-2} [1]. However, radiation induced defects in Si material, acting mainly as generation/recombination and carrier capture centres, affect the detector functional parameters. Therefore, a lot of efforts are made to unveil the radiation damage mechanisms and their impact on detector functional parameters. Consequently, search of new materials with enhanced potential of radiation hardness, of radiation induced effective charge, of high sensor response speed is desirable.

The GaN and SiGe alloys are considered as the most promising materials for fabrication of the radiation damage proof sensors [4-9]. The radiation hardness of these materials is enhanced by relatively heavy components of Ga and Ge. GaN has also prospects in manufacturing of double response sensors generating scintillation and charge collection devices. These materials owing to high densities of intrinsic defects show short carrier lifetime and fast response, as well. However, technology of GaN growth is at the adolescence maturity level, and a lot of problems should be solved in governing of efficient doping, in combining of thermal and pressure crystal growth regimes to suppress the high densities of technological extended defects (such as dislocations). Several technological trends [10-13] are developed in production of thin and thick material substrates of relevant quality in sensor manufacturing. The Metal-Organic Chemical Vapour Deposition (MOCVD) technology prevails in thin layer growth on sapphire, silicon, silicon carbide and other substrates. The Ammono-Thermal (AT) GaN growth [12-13] and Hidride Vapour Phase Epitaxy (HVPE) are the most promising technological solutions in mass-production of rather thick materials with acceptable dislocation densities of $< 10^4$ cm^{-2}. Nevertheless, the high densities of point defects, due to detrimental impurities appeared in crystal growth, determine the elevated conductivity of initial GaN materials, and doping with Mg, Mn and other elements [14, 15] is necessary to produce the high resistivity or even semi-insulating bulk materials in fabrication of thick radiation sensors, proper for reaching of the necessary amplitude electrical signals.

Technology in formation of $Si_{1-x}Ge_x$ alloys with $x<0.25$ and $x>0.9$ allows production of bulk materials [16-20] with enhanced radiation hardness and similar to Si electrical characteristics. The main difficulty in functioning of Si based particle detectors is irradiation caused removal of dopants leading to the change of material conductivity type. The inversion of conductivity type and extent determines a destroy of junction characteristics and either semiconductor transformation to insulator or increase of leakage current to unacceptable level. Therefore, the understanding of reactions among dopants and radiation defects should be enhanced. Also, the dopant activity transforms under local strain due to introduction of Ge atoms within Si lattice should be examined. The technology of material anneal modes should be invented to modify concentration of reasonable point defect complexes in acceptor/donor removal in SiGe alloys.

Despite the technological stride in fabrication of radiation hard new materials, the highest irradiation fluences of $\Phi > 10^{15}$ cm^{-2} lead to a decrease of the charge carrier concentrations those are insufficient to generate the measurable electrical signals. This needs to invent detector structures with internal gain sufficient to compensate carrier density loss in diode base region. One of the ways is to form an additional avalanche layer within sensor structure to gain the collected charge value to the appropriate level. This needs to clarify mechanisms of low gain avalanche processes and fabrication technologies of so-called Low Gain Avalanche Diodes (LGAD) by avoiding exponential rise of signal output and by creating structure of sensors of to have high speed detectors. Solution of the mentioned tasks also requires the specialized measurement methods and technologies for control of carrier lifetime, of defect spectrum, of carrier drift velocity and other material characteristics.

Evaluation of the mechanisms of radiation damage of particle detectors in the range of high fluences is commonly implemented by combining of several techniques [21-23]. Examination of carrier lifetime is performed by capacitance deep level transient spectroscopy (DLTS) and by exploiting measurements of drift current transients (TCT) in analysis of the post-irradiation state of devices. However, capacitance and depletion-based measurements (DLTS, C-V and TCT) become complicated when high resistivity material is exploited in fabrication of radiation sensors. Then, heavily irradiated diodes may experience a transition to an insulating substance state with rather small free carrier concentration, insufficient to sustain a depletion boundary. Therefore, the pulsed techniques of barrier capacitance transients under external illumination and pulsed spectroscopy of

the material photo-ionisation have to be involved in measurements of the interplay of radiation and technological defects.

The developed advanced radiation sensors were foreseen for medical applications, namely, for verification of the brachytherapy planning. This destination needs a design the miniature pin and LGAD radiation sensors of relevant signals, appropriate for installing into medicine catheters, and creation of the technologies of dosimetry probe positioning combined with dose measurements.

The above-mentioned problems comprise the research item of this dissertation.

Objectives of research. The aim of this work is addressed to developments of defect engineering in new materials of elevated radiation hardness and modelling of irradiation caused removal of dopants as well as dopant activity transforms under local strain in SiGe alloys. Also, issues of production of thin and thick GaN material of relevant quality in sensor manufacturing are anticipated to be considered. There, the peculiarities of GaN doping with several elements are foreseen in order to manufacture the high resistivity or semi-insulating bulk materials. suitable to govern the low gain avalanche processes and development of fabrication technologies of LGAD sensors [24].

The main objectives were concentrated on:

- search of the anneal regimes for the purposeful dopant activity transforms by introduction of Ge atoms into Si lattice and development of the technology of material anneal modes to modify concentration of reasonable point defect complexes in governing of the acceptor/donor removal within SiGe alloys;

- reveal of the efficient doping of GaN modes combined with thermal and pressure crystal growth regimes to suppress the high densities of technological defects in production of materials of relevant quality in sensor production;

- search of the optimized LGAD sensor structure in fabrication of the enhanced signal and fast response radiation detectors;

- development of the pulsed techniques in evaluation of the barrier capacitance changes transients and spectroscopy of the material photo-ionisation to unveil interplay of radiation and technological defects in SiGe and GaN materials;

- selection of the advanced radiation sensors for medical applications in verification of the brachytherapy planning and creation of the software means for the simultaneous dosimetry probe positioning and profiling of the accumulated dose.

Relevance and scientific novelty. The unveiled reactions among dopants and radiation defects and the dopant activity transforms under local strain due to introduction of Ge atoms within Si lattice comprise novelty in this work. Governing of efficient doping, in combining of thermal and pressure GaN crystal growth regimes to suppress the high densities of technological extended defects, expedient introduction of Mg and Mn elements in order to grow the high resistivity bulk materials in fabrication of thick GaN radiation sensors also comprise scientific and technological novelty of this research. Comprehensive control techniques and regimes of thermal anneal procedures in suppression and manipulation of the electrical activity of the radiation induced defects also contains technological novelty. Models describing detector current components are proposed and approved for analysis of carrier transport and recombination and thermal emission parameters compose methodical novelties. The methods of the simultaneous dosimetry probe positioning and profiling of the accumulated dose for medical applications and creation of technology of verification of the brachytherapy planning embody technological novelty of this study.

Practical importance. The comparative analysis of thick and thin GaN and SiGe structures grown by using various technologies revealed prospects of these materials in fabrication of advanced radiation hardness sensors generating scintillation and charge collection signals.

The anneal regimes for the purposeful dopant activity transforms by introduction of Ge atoms within Si lattice have been invented and the technology of creation of reasonable point defect complexes in governing of the acceptor/donor removal within SiGe alloys has been developed. The efficient doping of GaN modes combined with thermal and pressure crystal growth regimes for production of materials of relevant quality in sensor fabrication. It has been demonstrated methodical merits of pulsed techniques in evaluation of the barrier capacitance changes transients and spectroscopy of the material photo-ionisation to unveil interplay of radiation and technological defects in SiGe and GaN materials. It has been demonstrated the practical importance of modelling and experimental verification of the LGAD detector characteristics in creating the high sensitivity sensors of fast response operational in the range of high fluence irradiations.

The approved technology of verification of the brachytherapy planning and creation of the tentative hardware as well as software means for the simultaneous dosimetry probe positioning and profiling of the accumulated dose also comprise practical importance of this work.

Statements in defence. The main statements in defence of this thesis are as follows:

1. The density of trapping centres introduced by electron beam into $Si_{0.95}Ge_{0.05}$ diodes might be 1.8 times larger relative to the Si material diode, at the same collected fluence, and it testifies that the prevailing thermal emission centres in $Si_{0.95}Ge_{0.05}$ diodes are shallower by 15 meV than those, radiation induced into Si diodes. The carbon–oxygen metastable complexes (C_iO_i *) are transformed into stable-state complexes (C_iO_i) under 125 °C annealing of the 5 MeV electron irradiated samples, while the activation energy shifts of radiation-induced deep traps to low values appear under an increase in the Ge content of the SiGe alloy.

2. The carrier recombination lifetime, governed by radiation defects introduced by strongly absorbed proton irradiation, is longer for the SiGe alloy containing the larger Ge content (of 5%) due to prevailing of the acceptor-like radiation defects in p-type SiGe alloy containing the enhanced content of Ge.

3. Separation of the generation current components within BELIV transients enables estimation of the thermal emission lifetime and, consequently, thermal activation energy E_{tr}.

4. The bi-stable boron–oxygen (B_iO_i) complex is the prevailing minority carrier trap in *p*-type $Si_{1-x}Ge_x$ alloy and it is responsible for the *B* acceptor removal leading to degradation of sensor radiation hardness. The boron-doped $Si_{0.95}Ge_{0.05}$ diodes are more resistive to the appearance of the "acceptor removing" effect under heavy irradiations in comparison with boron-doped Si and $Si_{0.99}Ge_{0.01}$ diodes. The role of the boron–oxygen (B_iO_i) complex is significantly reduced in $Si_{0.95}Ge_{0.05}$ alloy due to local strain. Thereby, transformations of the radiation-induced B_iO_i defect in $Si_{0.95}Ge_{0.05}$ diodes can pave an advanced technology in enhancement of the detector radiation hardness based on SiGe alloys with elevated Ge content.

Author's contribution. Over this study author made analysis of carrier recombination and capture characteristics by combining various methods. Author performed modelling and measurements current-voltage, capacitance-voltage as well as TCT characteristics, part of DLTS characteristics on pin and LGAD Si and SiGe sensors. Author also contributed in characterization of GaN materials. He made most of the experimental and simulation research presented in this dissertation. The main results were presented at national (LNFK) conference and school. Several drafts of the published manuscripts were prepared by the author.

Several material characterisation experiments were performed in collaboration with PHD students D. Meškauskaitė and L. Deveikis. Most of DLTS characterisation K. Pūkas implemented together with dr. J. Pavlov. K. Pukas created a software for creation of technology of verification of the brachytherapy planning. K. Pūkas together with consultant dr. T. Čeponis and

dr.V. Rumbauskas improved instrumentation for brachytherapy applications. All the investigations, data analysis and preparation of manuscripts were made under supervision of prof. Dr. Sc. E. Gaubas.

The SiGe diode structures were produced and electron irradiations were performed at Minsk university. Proton irradiations of SiGe diodes and GaN materials were made at Centre for Physical Sciences and Technology, Vilnius. The neutron irradiation of GaN materials were carried out using Ljubljana TRIGA reactor.

Publications. The main results of this study are published within 4 scientific articles, 1 application for EPO patent and presented at 3 national conferences and schools of PHD student. Publications are listed below:

Articles:

A1. J. Pavlov, T. Ceponis, **K.Pukas**, L.Makarenko, and E. Gaubas,. *5.5 MeV Electron irradiation-induced transformation of minority carrier traps in p-type Si and $Si_{1-x}Ge_x$ alloys*, Materials 2022, 15, 1861. https://doi.org/10.3390/ma15051861.

A2. T. Ceponis, L. Deveikis, S. Lastovskii, L. Makarenko, J. Pavlov, **K. Pukas**, V. Rumbauskas, E. Gaubas, *Transient electrical and optical characteristics of electron and proton irradiated SiGe detectors*, Sensors **20** (2020) 6884.

A3. T. Ceponis, S. Lastovskii, L. Makarenko, J. Pavlov, **K. Pukas**, E. Gaubas, *Study of radiation-induced defects in p-type $Si_{1-x}Ge_x$ diodes before and after annealing*, Materials **13** (2020) 5684.

A4. E. Gaubas, T. Ceponis, L. Deveikis, D. Meskauskaite, S. Miasojedovas, J. Mickevicius, J. Pavlov, **K. Pukas**, J. Vaitkus, M. Velicka, M. Zajac, and R. Kucharski, *Study of neutron irradiated structures of ammonothermal GaN*, J. Phys. D: Appl. Phys. 50 (2017) 135102.

Patents:

EPO-1. E.Gaubas, T.Ceponis, **K.Pukas**, V.Rumbauskas, M.Uzgirytė, J.Venius, K.Akelaitis, A.Cicinas, *System and method for brachytherapy procedure planning and verification*, Application for EU patent V83-82 EP.

Presentations at conferences and PHD schools:

P1. **K.Pukas**, T. Ceponis, E. Gaubas; TCAD simulations of p-type Si and Si(1-x)Ge(x) low gain avalanche detector characteristics; Open Readings 2021; March 16-19, Vilnius (nuotolinė).

P2. **K.Pukas**, T. Čeponis, E. Gaubas; Comparison of Simulated p-type Si1−xGex and Si LGAD with Traps; Advanced materials and Technologies 2021, August 23-27, Palanga, Lietuva.

P3. **K. Pukas**, L.Dundulis, J.Vyšniauskas, E.Gaubas, TCAD simulations of functional characteristics for silicon low gain avalanche detectors, LNFK, 2018, Vilnius.

1. MOTIVATION OF RESEARCH OF THE OPERATIONAL CHARACTERISTICS OF SiGe AND GaN RADIATION DETECTORS

The state of knowledge about characteristics of SiGe [25-34] and GaN [7, 35-43] materials and operational features of radiation detectors made of these materials at the beginning of the PHD course are briefly reviewed in this chapter.

1.1. Radiation induced interactions and damage mechanisms in Si and SiGe materials

Silicon–germanium alloys are promising materials for the fabrication of photocells and powering space applications [44]. This alloy is also employed in the production of high-frequency heterojunction bipolar transistors for operation in the near THz range [45]. Silicon–germanium provides a novel approach to the formation of high-conversion efficiency and highly scalable thermoelectric materials. Silicon–germanium alloys have recently been reported [46] to function well as the lithium-ion battery anodes. This alloy is also prospective for the fabrication of microelectronic and optoelectronic devices such as high-speed temperature sensors, Hall effect transducers and γ-ray detectors [47,48]. Therefore, the spectrum of carrier traps is a desirable characteristic for material quality evaluation.

Silicon–germanium material-based devices are capable of operating in harsh radiation environments [26, 27]. Silicon–germanium-based pixel detectors with enhanced radiation tolerance are promising for applications in the future High-Luminosity Large Hadron Collider [1]. However, there are difficulties in growing bulk SiGe single-crystals due to the differences in the physical properties of silicon and germanium such as density and melting temperature. For example, single crystals have only been obtained for alloys containing either $0 < x < 0.1$ or $0.85 < x < 1$ of Ge when using the Czochralski technique. The alloy usually becomes polycrystalline for the other range of Ge content [48, 49].

The radiation damage of the $Si_{1-x}Ge_x$ devices related with introduction of radiation defects [1, 40, 49] can be healed by the atomic reconfiguration of the crystal structure during material anneal [50–52]. The particle detector degradation [53–56] usually appears through decrease of carrier recombination lifetime.

Carrier recombination lifetime in SiGe materials specifies the fast component of carrier density relaxation within transients of carrier decay via carrier-pair annihilation through deep centers. The decrease of recombination lifetime testifies an enhancement of radiation defect concentration which reduces signals and efficiency of detectors [54, 57, 58]. The carrier trapping is additionally associated with the single-type carrier emission centers. Capture of the single type carriers to these centers proceeds simultaneously with carrier annihilation, while subsequent thermal emission from these centers delays recombination process. Thereby, the asymptotic component of carrier density relaxation appears in carrier decay transients [58]. The rather shallow levels are usually associated with thermal emission centers which are responsible for the delayed responses of radiation sensors and leakage current [54]. Recombination characteristics of the irradiated materials specifies the evolution of radiation defect introduction, their types and densities [57, 58]. However, reports on investigations of the carrier recombination characteristics in SiGe alloys irradiated with various species of particles are scarce [50] in literature.

1.2. Impurities and defects in SiGe materials

The deep carrier traps affect the characteristics of the semiconductor particle detector [50, 59]. Impurities, such as oxygen and carbon in SiGe materials, play an important role in the formation of the irradiation-induced deep traps [50–52]. Vacancies and their complexes affect the switching properties of the SiGe-based devices [53, 54]. In some cases, radiation damage to the $Si_{1-x}Ge_x$ devices related to the introduction of radiation defects can be “removed” by annealing [55]. This can be implemented by the atomic reconfiguration of the crystal structure during material annealing [56]. However, the radiation defect spectrum in *p*-type $Si_{1-x}Ge_x$ detectors has been poorly examined. Thus, it is necessary to study the growth and radiation defects in SiGe materials as well as their transformations under annealing.

The radiation-induced boron dopant transformations in *p*-type Si lead to the so-called effect of ‘acceptor removal’ [16-19], which degrades the performance of particle detectors. This happens due to the substitutional lattice site boron (B_s) transformation into interstitial (B_i) boron under irradiation. Further migration of this B_i dopant and its reaction with interstitial oxygen impurity (O_i) in silicon crystal determines the formation of the interstitial boron–interstitial oxygen complex (B_iO_i). Thereby, the shallow acceptor (B_s) in Si becomes the deep-level trap (B_iO_i) of minority carriers

(electrons) with activation energy of about 0.25 eV. As a result, the space charge of the depleted base region and electric field in the active detector range are decreased, thereby reducing the signals of radiation detectors.

Additionally, some of radiation induced defects in Si are thermodynamically metastable [20], such as interstitial carbon–interstitial oxygen (C_iO_i*) complexes in *p*-type Si. The bi-stable defects can change their state under certain conditions. The metastable state can be frozen at low temperatures. The change of this state can be modified by illumination, temperature jump or applied external electrical field, where the transformations are mediated by electron–phonon interaction [20]. The B_iO_i complex in Si is also a metastable defect existing in at least two configurations, namely [$B_iO_i^A$] and [$B_iO_i^B$] [17, 18]. The density of the [$B_iO_i^A$] configuration complexes is usually reduced under external perturbation using light or temperature (heating to 353 K) due to their transformations to [$B_iO_i^B$] state [18]. However, the maximum concentration of [$B_iO_i^A$] can then be restored [17, 18] by retention in dark at reduced temperatures [18]. It has been reported [26–27] that silicon–germanium ($Si_{1-x}Ge_x$) alloys are promising for the production of detectors operational in radiation harsh environments. For *p*-type SiGe alloys, it is therefore necessary to study the acceptor removal effect in boron-doped SiGe materials. Modifications of the activation energy of electron traps in $Si_{1-x}Ge_x$, related to an increase in Ge content, should also be clarified [4].

The spectrum of deep traps of majority carriers in *p*-type Si and SiGe alloys, the meta-stability of the carbon–oxygen complexes and shifts of the activation energy of these defects were partially investigated. In this work, the minority carrier trap spectra obtained in 5.5 MeV electron-irradiated *p*-type $Si_{1-x}Ge_x$ (with x = 0–0.05) materials were considered. The vacancy–oxygen (VO) and the boron-oxygen (B_iO_i) complexes, as well as vacancy clusters, were revealed to be the dominant electron traps. It was proven that boron–oxygen complexes (B_iO_i) of stable form [$B_iO_i^A$] prevail in the temperature range of 65–280 K. It was shown that shifts of activation energy of the minority carrier traps appear due to an increase in Ge content in SiGe alloys.

1.3. Defect spectrum and functional characteristics of GaN based detectors

GaN and diamond exhibit high breakdown field and high threshold displacement energy [60]. These properties are essential for fabrication of radiation tolerant particle detectors. However, the presence of defects usually is unavoidable and plays a crucial role in determining the optical and electrical

properties of GaN materials [61]. The different types of native point defects and their complexes are formed during crystal growth and act as undesirable traps or recombination/generation centres at different energy levels. The radiation defects, introduced by high energy particle energy loss due to ionizing processes and through the non-ionizing energy loss (NIEL) [62, 63], significantly degrade parameters of the particle sensors. Therefore, identification of native and radiation-induced defects is a crucial part of making advantageous GaN devices.

The hexagonal wurtzite phase and cubic zinc blende phase of GaN semiconductors are two different polytypes of the GaN material [64]. The bonds between the Ga ions and the N ions are tetrahedrally coordinated and the inter-ionic distances within the close packed plane crystal are approximately the same for both phases. Sapphire and Si substrates are commonly used as a cost effective way [65] in epitaxial growth of GaN crystals. However, the epitaxial growth of GaN on lattice-mismatched substrates (Sapphire: ~13.7 %, Si: ~17 % [65]) are the main reason resulting in imperfect material and the high density of dislocations. Great progress has been made by growing the buffer layers [66], using ELOG [67] (Epitaxial lateral overgrown) technique [68, 69]. The special technologies like DEEP [70] (Dislocation elimination by epitaxial growth with inverse-pyramidal pits), void-assisted separation [71] or cross-stacked carbon nanotubes [72] have been developed for the production of freestanding GaN. For many detectors and optoelectronics applications (e.g. GaN-on-GaN LEDs and GaN-based laser diodes) the bulk GaN substrate is beneficial owing to reduction of the non-radiative recombination centres [73]. Hydride vapour phase epitaxy (HVPE) and ammonothermal (AT) method are commonly used technologies for large scale GaN substrates growth [74, 75]. These technologies are widely developed to obtain high quality and crack-free bulk GaN [76].

The introduction of point defects, e.g. vacancies, interstitials and substitutional atoms, into a crystal lattice strongly depends on growth conditions. The common unintentional substitutional impurities in GaN are oxygen (O) and carbon (C). Oxygen usually occupies N sites [69]. Calculations show that carbon is an amphoteric impurity in GaN, where C_{cation} is a shallow donor, while carbon on nitrogen sites (C_N) is a shallow acceptor [77]. The incorporation of C_N is preferable since the formation energy is rather low [69].

The dislocation (as a prevailing extended defect) densities can now be reduced as low as 10^3 cm^{-2}. The ammonothermal (AT) GaN crystals grown on HVPE-GaN seeds contain dislocation density of about 7×10^4 cm^{-2} [78] or less than ~10^3 cm^{-2} by using the small-size seeds (‘point seed’) [40]. The most

common planar defects are introduced due to the vertical mismatch of lattices or due to the disordering of crystallographic planes (stacking faults). Epitaxial growth of GaN directly on a Si-substrate leads to formation of volume defects, such cracks, due to strains initiated due to large mismatch of thermal expansion coefficients and lattice constants of GaN and Si [65]. For films that are under a uniform stress σ, cracking occurs when the thickness reaches a critical value. Although the GaN-based devices have been commercialized, a few issues for high reliability and for sensor application in harsh environment of these devices are still attracting considerable investigation.

The GaN based devices have demonstrated numerous benefits as compared to conventional Si based devices, showing the better performance at higher operating temperatures, faster switching speed, high breakdown voltage [73]. As a detector for high radiation environments, GaN benefits substantially from its very low leakage current, low dielectric constant, radiation hardness, and ability to operate at room temperature [78]. Here, characterization of defects is essential to the development of GaN materials. The field-effect transistors and power devices based on GaN are made by the emerging technology that have only recently become available commercially [79]. GaN-based devices are also widely employed for optoelectronic applications (light emitting diodes (LEDs) and laser diodes (LDs)) with remarkable advantages. Various others applications such as high density optical storage, visible light communication, photovoltaics, and biotechnology devices are being developed in early stage of mass production [69]. However, despite the wide applications of GaN-based devices, there are still several issues, including high defect density and strain-induced polarization [80, 81]. Gallium nitride (GaN) and its Al alloys (AlGaN) are becoming preferred materials for ultraviolet (UV) detectors due to their wide bandgap and due to the capability of tuning the direct band gap in energy range from 3.4 eV to 6.2 eV. Studies on advanced properties of GaN material have also been carried out their potential applications as sensing materials for deep UV photodetectors, by using Schottky barrier, metal-semiconductor-metal diode and pin photodiode structures [82]. The phenomenological GaN properties, e.g. the large bandgap (3.39 eV), high thermal stability, and large displacement energy (N: 109 eV and Ga: 45 eV) make it an attractive material for high energy particle detectors and dosimeters in harsh environments. Work in this area is still early in its development, but GaN-based devices, based on sandwich, mesa, pin structures, metal-semiconductor-metal and Schottky diode structures, have already been shown to be able to detect ultraviolet light, x-rays, alpha particles, electrons, and neutrons [60]. Thereby, GaN is a promising material in production of devices for chemical, gas, biological and

pressure sensing [83], for radiation imaging applications [7] and in fabrication of high energy particle detectors [8-10] operating in harsh environments. GaN can be employed for detection and tracking of high-energy particles or dosimetry by recording both the electrical and optical signals [35-38]. Suitability of GaN materials for sensor formation depends on their fabrication technology, doping and compensation level [38, 39]. The main obstacle in these applications of GaN remains high density of intrinsic technological defects, such as dislocations with density of about 10^9 cm^{-2} when GaN is grown by MOCVD technology. These intrinsic point and extended defects determine a rich spectrum of deep levels by affecting carrier lifetime [85] and by modifying electrical conductivity.

To suppress the enhanced un-intentional doping, fast recombination centres are commonly introduced by using the transitional metal impurities (such as Fe), to have a semi-insulating GaN material. However, this leads to the considerably short carrier lifetime, and increasing of the detector thickness, for instance, by applying CVD or HVPE grown GaN, becomes an improper mean for enhancing of an interaction path in particle detectors. Introduction of the radiation defects during operation of particle sensors in harsh areas of particle accelerators considerably depends on quality of the pristine material, exploited for detector fabrication [86-90]. Integral sensor damage by irradiations varies with thickness of sensors depending on particle type and energy, due to different interaction cross-sections, and on penetration paths for incident radiations. To reduce radiation damage of detectors, thin sensor structures with internal amplification [90] can be promising for particle tracking. Thus, the high quality MOCVD GaN might be suitable for fabrication of such type sensors. In order to produce rather thick sensors for recording of the penetrative particles with small interaction cross-section, the ammonothermally [91, 92] grown GaN with significantly reduced ($<10^4$ cm^{-2}) dislocation densities is the most promising material. Therefore, knowledge of the intrinsic and irradiation fluence dependent variations of the optical and electrical characteristics is important. However, production of defects by hadron irradiations, radiation hardness and charge collection efficiency of sensors fabricated on different technology GaN materials are examined insufficiently.

The ammonothermal (AT) GaN is the most promising material for high quality particle detector fabrication due to significantly reduced densities of the intrinsic defects (e.g. dislocation densities) relative to other technology GaN (HVPE, MOCVD) materials (cf. dislocation density is $<10^4$ cm^{-2} in AT GaN, $\geq 10^6$ cm^{-2} HVPE GaN and $\geq 10^9$ cm^{-2} in MOCVD GaN). Moreover, rather thick and homogeneous AT GaN single-crystals can be grown and

applied in production of sensors for detection of penetrative, high energy particles. The AT GaN materials doped with different impurities (Mn, Mg) were studied in order to estimate possibilities in fabrication of either fast or extremely sensitive particle detectors. The Mn impurities in GaN (GaN: Mn) may act as fast carrier traps and compensating centres for unintentionally introduced donor-type defects, inherent for GaN materials. Such the GaN: Mn mterial is suitable for formation of the high resistivity base diodes. The SI GaN:Mn can thereby be appropriate for production of fast and rather sensitive detectors, - as short carrier lifetime determines fast recovery of the sensor, while the depletion layer in SI GaN:Mn junction structure will be thick and easily governed by small concentrations of radiation generated secondary pairs of the excess carriers. The Mg impurities serve as the main dopants in formation of the p-type conductivity GaN. Thus, AT GaN:Mg material, especially with long carrier lifetimes, is the most suitable for production of thick junction-structure (for instance, pin diode) particle detectors. Thick sensors are inevitable in detection of high energy particles, where interaction cross-section is rather small, and long particle path within sensor is necessary for generation of secondary carrier pairs of recordable amount. The parameter of the carrier pair generation per detector length unit (~90 pairs/μm is inherent for GaN materials [7 – 10]) determines the required detector thickness to reach the recordable collected charge. The parameter of defect introduction rate serves as another important characteristic of the detector radiation hardness. Alternatively, a characteristic of carrier recombination/trapping lifetime as a function of irradiation fluence can be employed for estimation of material tolerance to heavy irradiations. In GaN materials, excess carrier annihilation appears due to radiative and non-radiative channels. Therefore, comprehensive characterization of the irradiated material should be applied to predict operational features of the designed particle sensors, especially for future, very high luminosity LHC experiments (e.g. CMS detectors, installed within harsh area of the CMS forward calorimeter, should sustain 10^{17} cm^{-2} fluences). The elevated doping densities of sensor materials can thereby be preferential to increase radiation tolerance of sensors by enhancing the ratio of dopant density relative to radiation defect concentration. The trade-off should often be found to harmonize the parameters of sensor thickness, speed, sensitivity, radiation hardness, etc. The irradiations of high energy particles (1 -10 MeV) lead to prevailing of NIEL processes in radiation damage of detectors [2, 9, 62]. The NIEL material damage by different type particle (neutrons, protons, pions, electrons) becomes then similar. Therefore, the 1 MeV neutron equivalent relative to NIEL damage is widely used [2, 9, 62] for estimation of the effective fluence within sensor characteristics such as charge

collection efficiency, carrier trapping lifetime, defect introduction rate. Complementarily, reactor neutron irradiations are rather suitable for emulation of the evolution of the particle detector functionality during LHC experiments, as homogeneous damage can there be easily reached.

2. MATERIAL AND DEVICE CHARACTERIZATION TECHNIQUES

The main techniques employed in this work for material and detector characterisation are briefly discussed in this chapter.

2.1. Characterization techniques based on I-V and C-V measurements

The standard approach in primary sensor characterization is based on measurements of junction current (I) and capacitance (C) dependences on applied voltage (V) , the so called I-V and C-V evaluations.

The I-V characteristic of the idealized junction is described by Shockley equation which consists of diffusion currents of minority carriers, as holes (I_p) and (I_n) electrons [93,94] and saturation current I_0:

$$I_D = I_p + I_n = I_0\left[\exp\left(\frac{qV}{kT}\right)-1\right] \tag{2.1}$$

expressed as

$$I_0 = \frac{qD_p p_{n0}}{L_p} + \frac{qD_n p_{p0}}{L_n} = \frac{qD_p n_i^2}{L_p N_D} + \frac{qD_n n_i^2}{L_n N_A}, \tag{2.2}$$

respectively. Here q is the elementary charge, V – voltage applied, k – Boltzmann's constant, T – absolute temperature, D_p and D_n – diffusion coefficients of holes and electrons, respectively, n_i – intrinsic carrier density, L_p and L_n – diffusion lengths of holes and electrons, respectively, N_D and N_A – donor and acceptor concentrations, respectively. Current of the forward biased junction of a unit area (S=1) is a sum of components determined by carrier recombination $I_R=(qn_iW_DS/\tau_{SC})\exp(qV/2kT)$ with inherent lifetime τ_{SC} in space charge region of width W_D and diffusion (eq. 2.2). In the case of high injection, the current is governed by carrier recombination lifetime τ_{HL} at high level (HL) excitation $I_T=2qn_{av}dS/\tau_{HL}$ and series resistance of quasi-neutral region of a diode length d (with average conductivity carrier density n_{av}). The current of the reverse biased junction $I_{SC}=qW_Dn_iS/\tau_{SC}$ is determined by generation processes within the depleted region. Thereby detector characterization employing the I-V dependences enables control the carrier recombination/generation parameters ascribed to the impact of the intrinsic and radiation induced defects.

The C-V characteristics are analysed using depletion approximation [57] where barrier capacitance of asymmetric p^+n junction is expressed as [57]:

$$C = \frac{\varepsilon\varepsilon_0 S}{W_D}. \tag{2.3}$$

Here

$$W_D = \sqrt{\frac{2\varepsilon\varepsilon_0 (V_R + V_{bi})}{eN_D}} \tag{2.4}$$

is a depletion width governed by the applied reverse voltage V_R and built-in potential of junction barrier V_{bi}, ε and ε_0 are the dielectric constants of material and vacuum, respectively, and N_D is dopant concentration. At $V_R >> V_{bi}$, the slope of capacitance characteristic C^{-2} vs. V_R enables evaluation the effective doping concentration as

$$N_{eff} = \frac{2}{e\varepsilon\varepsilon_0 S^2}\left(\frac{C^{-2}}{V_R}\right)^{-1}. \tag{2.5}$$

Actually, free carrier density decreases approximately exponentially with distance from the junction boundary within the depletion region, characterized by the Debye length L_D:

$$L_D = \left(\frac{\varepsilon\varepsilon_0 kT}{q^2 N_D}\right)^{\frac{1}{2}}. \tag{2.6}$$

In dc measurements of C-V characteristics, the effective density of dopants N_{eff} is evaluated by control of saturation voltage V_{FD}, where $W_{FD}=d$ is evaluated with precision of $\pm L_D$ [57].

In practice barrier capacitance evaluations are based on measurements of small ac test signal u phase shifts due to displacement current. The displacement current, represented as

$$i_C = C(V_R)(du/dt) \tag{2.7}$$

and generation current expressed as

$$i_g = qn_i S\delta/\tau_g, \tag{2.8}$$

are really controlled. The LRC-meter response proportional to the test current peak, is caused by a width of damaged layer δ and by the ratio of test signal frequency ω and generation lifetime τ_g, i.e. $\omega\tau_g$. C-V characteristics are commonly measured by employing small signal impedance measurements. Since diode is non-linear element, equivalent circuits are employed for the extraction of parameters [52]. The equivalent circuit of the diode is comprised of junction capacitance C, conductance G and serial resistance r_S [95]. The conductance depends on diode leakage current. Serial resistance r_S is

determined by the volume and electrodes resistance. The dissipation factor D_S of parallel (*p)* and serial (*s*) circuit in test signal ac current measurement regimes is related to quality factor *Q* as:

$$Q_S = \frac{1}{D_S} = \frac{1}{\omega C_S R_S};\ Q_P = \frac{1}{D_P} = \frac{\omega C_P}{G_P}. \tag{2.9}$$

It has been shown [95] that measurement of diode capacitance is correct when $Q \geq 5$. Then C_p coincides with C_s. When $Q<5$, a difference between C_p and C_s appears. These qualitative ratios enable control whether the relevant measurement modes are applied.

Measurements of I-V characteristics in this study were performed by employing a commercial sub-femtoamp source-meter Keithley 6430 instrument, while C-V characteristics were measured by a high precision QuadTech 7600 LRC-meter using small ac signals within frequency range of 20 Hz – 2 MHz.

2.2. Deep level transient spectroscopy technique

Deep level transient spectroscopy (DLTS) technique is addressed to evaluating of the thermal activation energy (E_T), concentration (N_T) and capture cross-section (σ) of defect associated carrier traps [57]. This technique is implemented by measurements of barrier capacitance transients caused by filling and release of defect levels through free carrier (holes-*p* and electrons-*n*) capture (*c*) and (*e*) emission within depletion region. These processes are described by the rate equations:

$$c_n = \sigma_n \langle v_n \rangle n \text{ and } c_p = \sigma_p \langle v_p \rangle p, \tag{2.10}$$

$$e_n = \sigma_n \langle v_n \rangle N_C \exp\left(-\frac{E_C - E_t}{kT}\right) \text{ as well as}$$

$$e_p = \sigma_p \langle v_p \rangle N_V \exp\left(-\frac{E_t - E_V}{kT}\right). \tag{2.11}$$

Here, $\langle v_{n,p} \rangle$ represent thermal velocities and *n, p* denote density of electrons and holes, respectively, N_C, N_V represent density of states in conduction and valence bands, respectively. $E_{C,V}$ is energy ascribed to conduction band minimum or valence band maximum, *k* is Boltzmann's constant, *T* is the absolute temperature. Carrier thermal velocities $\langle v_n \rangle$, $\langle v_p \rangle$ are dependent on $T^{1/2}$, and while state densities N_C, N_V are dependent on $T^{3/2}$, then e_n, e_p are

proportional to T^2. Variation of electron occupancy with time in DLTS transients is described by the rate equation:

$$\frac{dn_t}{dt} = \left(c_n + e_p\right)\left(N_t - n_t\right) - \left(e_n + c_p\right)n_t \tag{2.12}$$

solution of which is obtained as

$$n_t(t) = \frac{c_n + e_p}{c_n + e_p + c_p + e_n} N_T + \frac{e_n + c_p}{c_n + e_p + c_p + e_n} N_T \exp\left[-\left(c_n + e_p + c_p + e_n\right)t\right], \tag{2.13}$$

indicating the exponential n_t relaxation to the steady state level filling with a rate constant $\tau^{-1}=c_n+e_p+c_p+e_n$.

The DLTS transient is formed as a consequence of such processes: in the absence of the reverse voltage, traps are filled by majority carriers, as carrier capture process dominates ($c_n>e_n$). When applied V_R causes a depletion region change, the emission process starts to dominate. The emitted electrons are extracted by the electric field from the depleted region by increasing the positive space charge in the depletion region, which changes the barrier capacitance with asymptotic equilibrium ($t=\infty$) as:

$$C(\infty) = \left\{\frac{\varepsilon\varepsilon_0 S^2 (N_D + N_T)}{2(V_{bi} + V_R)}\right\}^{\frac{1}{2}}. \tag{2.14}$$

The temporal variation of capacitance due to carrier emission is expressed as:

$$C(t) = \left\{\frac{\varepsilon\varepsilon_0 S^2 (N_D + N_T - n_t(t))}{2(V_{bi} + V_R)}\right\}^{\frac{1}{2}} = C(\infty)\left(1 - \frac{n_t(t)}{N_D + N_T}\right)^{\frac{1}{2}}. \tag{2.15}$$

The modulation of capacitance $\Delta C(t)=C(t)-C(\infty)$ in time (t) leads to the transient as:

$$\frac{\Delta C(t)}{C(\infty)} = -\frac{N_T}{2N_D}\exp\left(-e_n t\right). \tag{2.16}$$

The time constant of the capacitance transient gives the thermal emission rate, and the amplitude of the transient $\Delta C(0)/C(\infty)$, being equal to $N_T/2N_D$, gives a measure for traps concentration.

A peculiarity of DLTS method is scanning of emission rate dependence on temperature and usage of correlation functions in recording of transients by applying the "rate windows". The latter feature provides the maximum capacitance variation output when time constant τ is equal to a known time constant τ_{ref} determined by the correlation function. As the emission rate increases with temperature, the peak occurs in the rate window output as $\tau=e_n^{-1}(T)$ by passing through τ_{ref} for each trap. By repeated scans with different values of τ_{ref}, sets of e_n values at fixed peak temperatures T_{pk} are obtained.

These data sets are employed to plot the Arrhenius curves, representing the $\ln(e_n^{-1}T^2)$ dependence on T^{-1}. These Arrhenius plots are exploited for evaluation of E_T and σ_n parameters, determined for each trap. Either the plots of $\ln(e_n^{-1}T^2)$ versus T^{-1} or the sets of E_T and σ_n of parameters are called "trap signatures".

Digital DLTS is implement when records of the whole capacitance transients and time constant L-DLTS (Laplace-DLTS) in one system are performed. In a L-DLTS mode, the capacitance transient is measured with great precision at fixed temperature. These transients are analyzed using Fast-Fourier-Transform-based algorithms to convert the defect relaxation process from the time domain into a spectrum of time constants in the frequency domain.

The DLT spectra were recorded in this research using a commercial HERA-DLTS 1030 instrument (PhysTech GmbH, Moosburg an der Isar, Upper Bavaria, Germany). These DLT spectra were examined in the temperature range of 15–280 K. The majority carrier trap spectra were recorded at reverse bias voltage (U_R) of 3 V and injection pulses (t_p) of 10 ms duration. Each spectrum was analysed by combining correlation functions and the Laplace method. For L-DLTS measurements requires a higher signal-noise ratio and an a-priori knowledge of the temperature interval where the capacitance transient takes place as it is based on isothermal measurements, therefore the analysis of L-DLTS spectra on the defects-rich materials are difficult. Nevertheless, the combination of the special possibilities of all the systems makes the HERA-DLTS much more flexible and reliable for evaluated values of the overlapping processes.

Routine modes of the minority carrier deep-level transient spectroscopy by using electrical (MC-DLT) and optical (MCT) [57, 95, 96] excess carrier injection were applied to highlight the minority carrier traps. A HERA-DLTS 1030 instrument (PhysTech GmbH) was employed to record the MC-DLT and MCT spectra using different correlation functions. The MCT regime was implemented using the continuous-wave IR light laser excitation (λ = 1064 nm) to homogeneously generate excess carriers within the depth of the sample. The IR light excitation was performed using illumination of the edge side of the diodes.

2.3. Pulsed technique of barrier evaluation by linearly increasing voltage

Barrier Evaluation by Linearly Increasing Voltage (BELIV) technique [97] in this research has been implemented by analysis of current transients induced

by charging barrier capacitance. The barrier capacitance (C_b) changes due to time varied reverse bias with a linearly increasing voltage $U=At$ pulse. The C_b dependence on voltage and thereby on time t can be described using the depletion approximation [57] in the analysis of charge extraction transients. This approximation leads to the simple relation $C_b = C_{b0}(1+U/U_{bi})^{-1/2}$ for an abrupt p^+-n junction in the pin diode, where the barrier capacitance C_{b0} for the non-biased diode of area S is given by $C_{b0} = \varepsilon\varepsilon_0 S/W_0 = (\varepsilon\varepsilon_0 S^2 e N_D/2U_{bi})^{1/2}$. Here, $W_0 = (2\varepsilon\varepsilon_0 U_{bi}/eN_D)^{1/2}$ is the width of depletion for non-biased junction, and $A=U_P/\tau_{PL}$ the ramp of the LIV pulse with amplitude U_P and of duration τ_{PL}. The time dependent changes of the charge $q=C_bU$ within the junction, indeed determine the current transient $i_C(t)$:

$$i_C(t) = \frac{dq}{dt} = \frac{\partial U}{\partial t}(C_b + U\frac{\partial C_b}{\partial U}) = \frac{\partial U}{\partial t}\frac{1+\frac{U_C(t)}{2U_{bi}}}{(1+\frac{U_C(t)}{U_{bi}})^{3/2}} \cong AC_{b0}\frac{1+\frac{At}{2U_{bi}}}{(1+\frac{At}{U_{bi}})^{3/2}}. \qquad (2.17)$$

This transient contains an initial (t=0) step AC_{b0} due to displacement current and a descending component governed by charge extraction. Thereby, the value of N_D ($N_{Def}=N_D-N_A$) can be evaluated by substituting the extracted U_{bi} in the initial current expression $i_C(0)=AC_{b0}$. The diffusion current i_{diff} also appears due to carrier induction, however it stabilises rapidly with reverse bias voltage. The diffusion current determines a differential resistance of a junction, and it is expressed as $i_{diff}(t) = i_{diff\infty}[1 - e^{-eAt/kT}] \cong \cong eSn_i^2L_{Dp}/N_D\tau_p[1-e^{-eAt/kT}] \approx eSn_i^2L_{Dp}/N_D\tau_p$. In reality, a delay in the initial part of the transient appears due to external circuit time constant and serial processes of dielectric relaxation within a boundary at quasi-neutral range of the non-depleted n-layer, drift and diffusion of carriers to complete the circuit. The resulting τ_{RC} modifies crucially the initial current step $i_C(0)$ by decreasing its amplitude $i_C(0)$ by a factor $\exp(-t/\tau_{RC})$. The modified current $i_{CM}(t)$ transient, caused by τ_{RC}, is described by using a convolution integral (with $\tau_{RC}=mRC$ dependent on the precision required)

$$i_{CM}(t) = \frac{1}{\tau_{RC}}\int_0^t i_C(x)\exp[-\frac{(t-x)}{\tau_{RC}}]dx. \qquad (2.18)$$

Due to RC both a reduction and a shift of the i_{CM}(t) peak appear. Fitting of the experimental transient $i_{CM}(t)$ with τ_{RC} as fitting parameter, allows extracting U_{bi} and C_{b0}.

In materials containing a considerable density of deep traps, modification of $i_{CM}(t)$ transient by τ_{RC} within the initial part appears to be more complicated

when τ_{RC} is governed by carrier capture/release processes [57]. Radiation induced traps are responsible for a generation current within the depletion region. This current $i_g(t)=en_iSw_0(1+At/U_{bi})^{1/2}/\tau_g$ increases with voltage $U(t)$ and can exceed the barrier charging current in the ulterior range of pulsed transient when the carrier generation lifetime τ_g is rather short.

The transient of the total reverse current is a result of the sum of the ($i_{R\Sigma}(t)= i_C(t)+ i_{diff}(t)+ i_g(t)$) currents:

$$i_{R\Sigma}(t) = AC_{b0}\frac{1+\frac{U_C(t)}{2U_{bi}}}{(1+\frac{U_C(t)}{U_{bi}})^{3/2}} + i_{diff\infty}(1-e^{-\frac{eU_C(t)}{k_BT}}) + \frac{en_iSw_0}{\tau_g}(1+\frac{U_C(t)}{U_{bi}})^{1/2} \quad . \qquad (2.19)$$

Subsequently, the carrier generation lifetime can be determined by using Eq. (2.19).

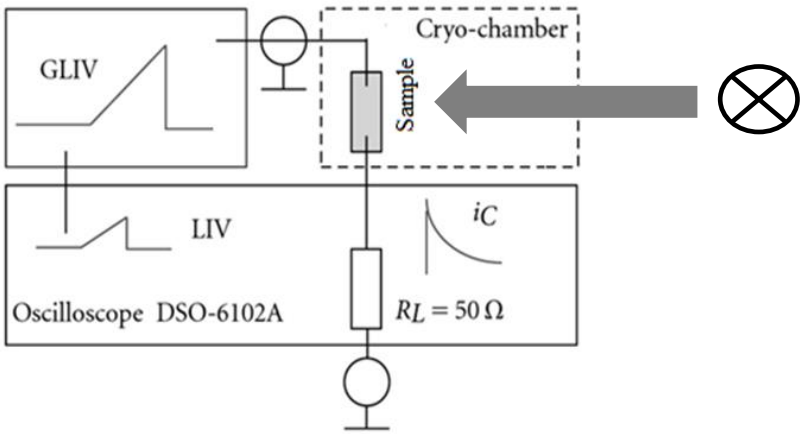

Fig. 2.1. A sketch of circuitry for implementation of the pulsed Barrier Evaluation by Linearly Increasing Voltage (‘) technique

The measurement circuitry (Fig. 2.1) for implementation of the BELIV technique contained an adjusted output of a generator of linearly increasing voltage (GLIV), a diode under investigation, and a load resistor connected in series. Current transients are registered using a 50 Ω external resistor or a load input of the Agilent Technologies DSO6102A oscilloscope. The other channel of the digital oscilloscope is exploited for synchronous control of linearity of a GLIV signal using a signal differentiating procedure installed within DSO oscilloscope. Linearity of the GLIV signal is essential within implementations of the BELIV technique. The diode under test has been mounted on a cold

finger within a vacuumed cryo-chamber for examination of the temperature variations of BELIV characteristics.

2.4. Microwave probed photoconductivity transient technique

Microwave probed photoconductivity transient (MW-PCT) technique is commonly employed in our laboratory for the direct measurements and extraction of carrier lifetimes [21]. The improved measurement regimes using analysis of the shape and constituents of the photoconductivity relaxation transients have been applied in order to clarify the impact of carrier trapping effects, the ion-linear carrier decay processes and to estimate the role of surface recombination.

MW-PCT technique is based on interaction of electromagnetic radiation and material, actually, the MW-PCT characteristics are modified due to absorption of microwaves by free carriers. For microwave region this interaction is described by Drude–Lorentz model when microwave frequency w_{MW} is much smaller than inverse lifetime of carrier scattering τ_S ($w_{MW}\tau_S$ <<1). In this case, a strength of interaction can be evaluated by employing the absorption coefficient α_{MW} parameter, as the coefficient of free carrier absorption is nearly independent of frequency, being far from resonances. However, dispersion of the free carrier absorption determines the enhanced values of α_{MW} relatively to that for infrared light frequencies range α_{IR}., i.e. $\alpha_{MW} >> \alpha_{IR}$. The higher sensitivity of registered signals is thereby achieved for microwave probing regime compared to that for common IR frequencies, in estimation of the free carrier parameters.

Excess carriers photo-generated by short laser pulse modify the microwave absorption. Variations of carrier concentration within the material modify the absorbed or reflected microwave radiation power. The amplitude of response of microwave probed photoconductivity transients $U_{MW\text{-}PC}$ as a function of excitation density and microwave radiation intensity can be written:

$$U_{MW-PC} = \kappa[I_p \Delta K - I_n], \tag{2.20}$$

where I_p is the intensity of MW radiation, I_n – the intensity of scattered radiation noise, κ– the electrical signal transmission function of MW detector. At equilibrium K depends on material conductivity when sample thickness and MW frequency are constant. The resonance of the MW system is achieved by adjusting the MW bridge, by varying the distance between sample and MW probe or by varying the MW frequency. For the case of $\Delta\sigma/\sigma_0$<<1 and

$\Delta K/K<<1$, the change of MW power modulation is a linear function of conductivity changes $U \propto \Delta\sigma \propto \Delta n$, where Δn is a concentration of excess carriers. The recorded a transient photoconductivity response is determined by the decay of excess carrier concentration.

The MW-PC instrument (Fig. 2.2) consists of the microwave bridge connected to either a slit or needle-tip antenna, of a microwave generator (Gunn diode), of a resonance chamber with microwave detector. Excess carriers are generated by a STA-01 microchip YAG:Nd laser with pulse duration of 500 ps at wavelength of 1062 nm. Excitation at 531 nm wavelength via single mode fiber is also applied when carrier lifetime variations within depth of wafer or layered samples are scanned on cross-sectional boundary of the sample. An excited area of the sample is probed by microwaves at 22 GHz by using either a slit antenna for depth integrated lifetime measurements or a needle-tip coaxial antenna for cross-sectional scans to achieve high special resolution. The MW bridge is attenuated using sliding shorts to achieve a resonance of the MW system. The excess carrier decay transients are registered by using a 1 GHz oscilloscope TDS-5104. A PC computer is employed for control of the measurement procedure, and for data sampling, acquisition and recording.

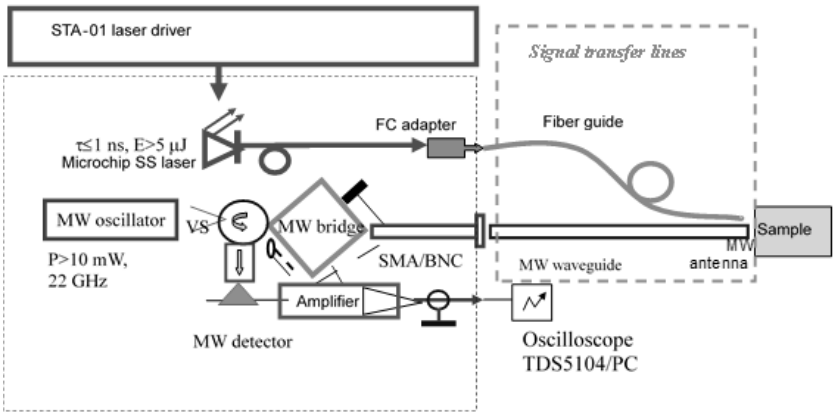

Fig. 2.2. A sketch of circuitry of the instrument for recording of microwave-probed of technique photoconductivity (MW-PC) transients.

The effective lifetime τ_{eff} can be approximated by the phenomenological expression

$$\tau_{eff} = 1/\left[1/\tau_b + 1/\left(\tau_s + \tau_D\right)\right] \tag{2.21}$$

being a result of both the bulk (τ_b) and the surface (τ_s) recombination components. The surface recombination can proceed after carriers diffuse to the surface during time $\tau_D = d_{eff}^2/\pi^2 D$. On the other hand, $\tau_s = d_{eff}/s$ can be

expressed via surface recombination velocity *s*. Here, d_{eff} is the effective sample thickness and *D* is a coefficient of the carrier diffusion. Absolute values of τ_{eff} are rather good characteristics of the material and of surface passivation efficiency within qualitative analysis of recombination rates.

Carrier lifetime, ascribed to the non-radiative carrier recombination, is commonly evaluated from the slope of the MW signal relaxation rate at exp(-1) level using a definition of the instantaneous lifetime $\tau_{inst}=n(t)/(-dn(t)/dt)$. For simple situations of prevailing of the single-type deep centres, the transients of the carrier concentration decay are single-exponential. In the cases of either competition of several centres or dispersive carrier transport with carrier trapping, the carrier decay transient acquires the shape of the multi-exponential relaxation curve. The parameters of excess carrier (n_{ex}) recombination and trapping centres have been obtained by analyzing carrier decay transients recorded by MW-PC technique [21] at relatively low excitation level (with $n_{ex} \leq 10^{15}$ cm^{-3}).

The non-linear decay process with simultaneous action of the radiative (as UV photoluminescence) and non-radiative recombination through deep levels becomes the most realistic. Such a process of the excess carrier variation in time ($n_{ex}(t)$) can be described [21] as follows:

$$n_{ex}(t) = \frac{n_{ex,0} \exp(-\frac{t}{\tau_R})}{1 + B n_{ex,0} \tau_R [1 - \exp(-\frac{t}{\tau_R})]} \qquad (2.22)$$

Here, *B* is the coefficient of radiative recombination, τ_R is the carrier lifetime ascribed to the non-radiative recombination, and $n_{ex,0}$ is the excess carrier concentration at the peak of excitation. The MW-PC signal is proportional to the concentration of free carriers. Thereby, the parameter $n_{ex,0}$ is directly estimated using a transient taken from experiment at fixed excitation density. The excitation density is evaluated using the laser beam parameters and material absorption coefficient at fixed wavelength. The tentative value of carrier lifetime (τ_R) ascribed to each transient can also be estimated from the slope of the asymptotic (close to an exponential: $n_{ex,0}\exp(-t/\tau_R)/[1+B\tau_R n_{ex,0}]$) component within a recorded transient. Thus, value of either *B* or a pair (B, τ_R) is the only adjustable parameter involved into simulation of the experimental transients. It is worth mentioning that even the simple two-exponential relaxation approach includes more than three adjustable parameters to reach fitting of the recorded transients by the simulated ones.

The two-componential decay is there caused by the multi-trapping effect. This two-componential transient appears when carrier lifetime depends on the

excess carrier density. The thermally generated carriers from the emission centers, vary the concentration of the recombining carriers and delay the carrier-pair annihilation process. The latter carrier-pair annihilation process prevails in the initial stage of carrier decay. The initial decay is ascribed [20] to recombination lifetime τ_R while asymptotic decay is characterized by the instantaneous trapping lifetime $\tau_{inst,tr}$ related to trapping coefficient K_{tr} as [21]

$$\tau_{inst,tr} = \tau_R K_{tr};\ \ K_{tr} = 1 + \frac{T_{tr} N_{C,V,e,h,Ttr}}{(N_{C,V,e,h,Ttr} + \Delta n)^2} \tag{2.23}$$

where T_{tr} is a concentration of shallow trapping centers, $N_{C,V,e,h,Ttr} = N_{C,V} exp(-\Delta E_{Ttr}/kT)$ is the effective density of band states, and Δn is the trapping attributed excess carrier density. The quasi-exponential decay with time (t) dependent instantaneous lifetime $\tau_{inst,tr}(\Delta n(t))$ is a reason of the non-linear carrier decay process.

2.5. Injected charge collection current techniques

Analysis of particle detector operation is commonly performed on the basis of consideration of the injected charge drift induced Ramo's current [98-100]. These transients allow to reconstruct an electric field distribution within the active layers of particle detectors [101, 102]. Profiling of both the carrier recombination centres [103, 104] and the injected charge drift velocities [105-109] performed by a cross-sectional scan of the photoconductivity and drift current transients provide rather comprehensive information about charge generation and drift material features. However, a simplified analysis [98, 101] of the drift current transients in detector junction structures is usually applied for the interpreting of the detector signals. The Ramo's derivation [99] gives an algebraic form of current expression obtained from the principles of simultaneous conservation of the electrostatic energy or reciprocity principle [100], of charge and of charge momentum ($q\mathbf{v}$) for the complete closed circuit with fixed electrodes. In our laboratory it has been proved that equal fields [100] superpose in modification of time varied current due to a drifting charge. It has been shown that these fields are time and drifting charge position dependent.

The current density for a drift of the electron monopolar domain and drift velocity (rate) field is described in the scalar form as [109]:

$$j = \frac{d\sigma}{dt} = q_e \frac{1}{d} \frac{dX_e}{dt} = q_e \frac{d\psi_e}{dt}, \tag{2.24}$$

and

$$\frac{d\psi_e}{dt} = \frac{1}{\tau_{TOF}} + \frac{1}{2\tau_{M,NDef}} + \psi_e\left(\frac{1}{\tau_{Mq}} - \frac{1}{\tau_{M,NDef}}\right), \qquad (2.25)$$

respectively. It can be noticed that expression (Eq. 2.23) for the current density coincides with that Ramo's derived. The kinetic equation (Eq. 2.24) for the drift rate satisfies the boundary conditions for the drift time $t_{dr,}$ as:

$$\psi_e = \psi_{e0} \ for\, t = 0; \quad \psi_e = 1 \ for\, t = t_{dr}\,. \qquad (2.26)$$

The bipolar charge initial injection causes a peculiarity in the analysis of the recorded waveforms of the current transients. This injected neutral domain is separated into electron *(q_e)* and hole *(q_h)* sub-domains under the diffusion and external voltage source field (q_C) action. These domains drift in the opposite directions, while diffusion in these (along *x* axis) directions can be ignored if applied voltage is sufficient (i.e. $q_c >> q$). The current density module for the bipolar drift is expressed by

$$j_b = \frac{d\sigma_{e-h}}{dt} = |q|\left(\frac{d\psi_e}{dt} + \frac{d\psi_h}{dt}\right). \qquad (2.27)$$

For the proceeded monopolar drift of electrons with ψ_e^{*0} as an initial position, the current density, in the case of the mixed regime, is expressed by using solution as

$$j(t) = \begin{cases} j_1 = \dfrac{q_e}{\tau_{tr,h}}\{\psi_0[1-\exp(-\dfrac{t}{\tau_{tr,h}})] + \exp(-\dfrac{t}{\tau_{tr,h}})\}, \quad for \quad 0 \le t \le \tau_{tr,h}; \\ j_2 = \dfrac{q_e}{\tau_{Mq,e}}[\exp(1-\dfrac{\tau_{Mq,e}}{\tau_{M,NDef}})\dfrac{t}{\tau_{Mq,e}}(\dfrac{\tau_{Mq,e}}{\tau_{TOF,e}} + \dfrac{1}{2}\dfrac{\tau_{Mq,e}}{\tau_{M,NDef}} - 1 + \dfrac{v_0\tau_{Mq,e}}{d})], \quad for \quad 0 \le t \le \tau_{e,mon}. \end{cases} . \qquad (2.28)$$

Here, the step-like change of field and current density would be obtained for an instant of hole arrival to the grounded electrode. It has been deduced that the suitable injection location ψ_0 for the pure bipolar drift depends on the injected charge density and the ratio of carrier mobilities. Simulated profiling of ICDC transients (Fig. 2.3) implies that the initial current peak increases with approach of the injection point towards electrodes. This can be explained by a shortening of the bipolar drift duration. The current changes during the bipolar drift stage also show that sub-domains of the drifting holes and electrons interact via the induced charges on electrodes (mediated through a voltage source).

Therefore, the ICDC pulse duration increases and a peak amplitude falls down with approach of the injection location to the mid of the inter-electrode spacing. This can be explained by the changes of the instantaneous electric field, ascribed to the injected/drifting charges. Thereby an increase of pulse

duration (for the injection location which satisfies the pure bipolar drift) can also be understood at an assumption that the amount of drifting charge and charge collection efficiency are invariable.

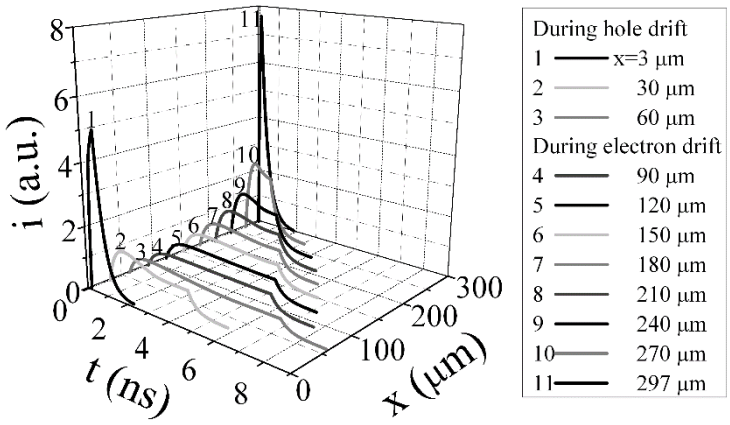

Fig. 2.3. Simulated profiling of the ICDC transients due to the injected charge (3.5×10^{-12} C/cm^2) domain in 300 μm thick n-type conductivity base for U=100 V applied voltage.

The light induced domain of excess electrons on large density is able to dissipate through (be collected at) the n^+ electrode due to diffusion across the base and carrier extraction by the electric field at the external electrode. The simplified approximation in charge collection transient formed by carrier domain drift and diffusion process can be described by a classical expression [110] for carrier density variations dependent on time and position as:

$$n_{R-D}(x,t) = (n_{ex0} - n_{tr}(t))\frac{\Delta}{\sqrt{4\pi D_A t}}\exp\{-[\frac{(x-\mu Et)^2}{4D_A t} + \frac{t}{\tau_R}]\}. \qquad (2.29)$$

Here, n_{ex0} is the initial (t=0) density of bipolar photo-excited carriers, D_A is the coefficient of carrier ambipolar diffusion.

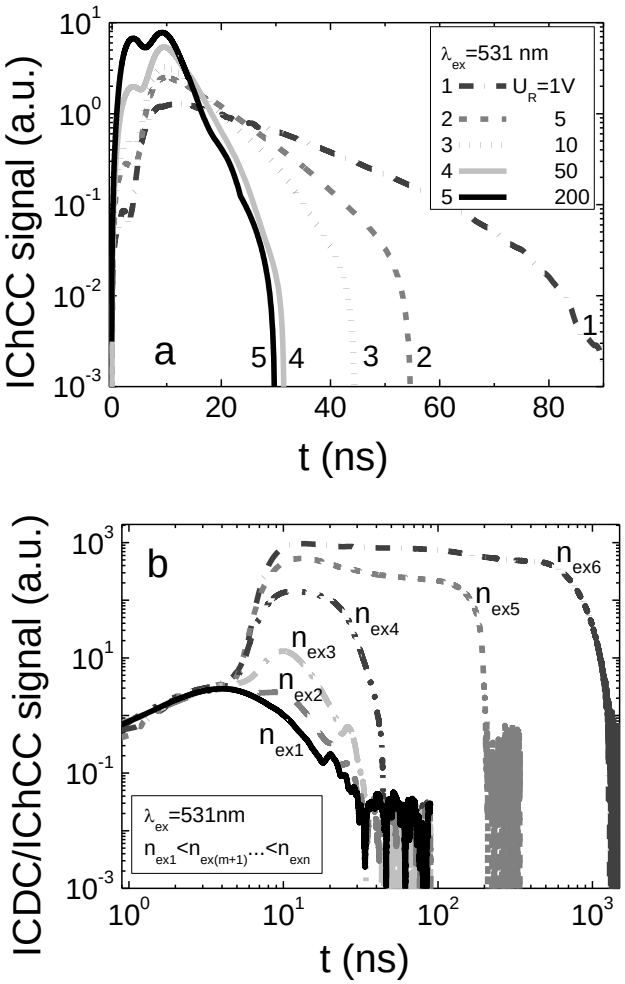

Fig. 2.4. Current transients measured in non-irradiated diode as a function of reverse voltage U_R at constant excitation density (a) and as a function of excitation density at fixed U_R (b).

Depending on the probing (either through electrodes or by microwave antennas MW-PCT-E) regime, the signal is sensitive either to carrier density at the collecting electrode ($n_{R\text{-}D}(t,d)$) or depth integrated carrier density $(1/d)\int_0^d n_{R\text{-}D}(t,x)dx$, respectively. In the pin diode, n^+ electrode collects electrons (and blocks holes), hence the injected charge collection current (IChCC) is measured. The MW-PC-E transient appears as a relaxation pulse with a vertex characterized by the descending slope of a trapezium-like pulse serving for the extraction of recombination lifetime. At a rather high excitation density, $en_{ex}\Delta > CU$, and low applied voltage the IChC current transients (Fig. 2.4) may acquire a rising peak pulse shape with very small amplitude at initial

instants and effective lifetime at the IChCC pulse vertex evaluated as $\tau_s=(\tau_D^{-1}+\tau_R^{-1})^{-1}$ with carrier recombination (τ_R) and diffusion $\tau_D \cong d^2/4\pi^2 D_A$ times.

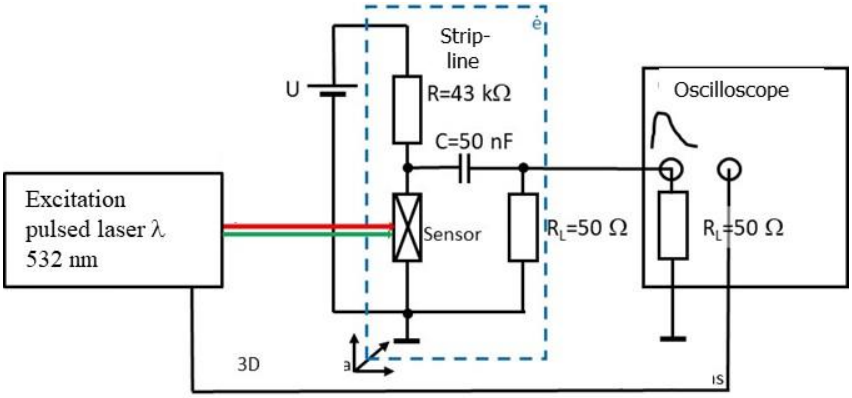

Fig. 2.5. A circuitry for recording of TCT transients using either surface or diode edge excess carrier domain injection by focused laser beam of strongly (surface excitation case) absorbed light or IR beam, respectively.

A setup of the TCT (Fig. 2.5) current profiling measurements have been performed by either surface or diode edge carrier domain injection. The PicoQuant 1064 nm wavelength laser using 120 ps pulses is employed to inject excess carriers. The transients are recorded by a 2 GHz Lecroy 620 Zi oscilloscope. The diode under test is mounted on PCB strip-line.

2.6. Techniques of photo-ionization spectroscopy

The steady-state photo-ionization spectroscopy (SS-PIS) [20,23] was applied to highlight the photo-active centers in the pristine and irradiated diodes with various content of Ge within SiGe alloy. The photometric 800 W lamp served as a source of varied wavelength which light was dispersed through a double-path monochromator DMR4. Thereby, the excitation wavelength was varied in the range of 0.5–3 μm. The Keithley 2635B source-meter was employed to measure the dc photo-current induced by varied excitation wavelength. The sample under test was mounted in a cryostat and cooled by liquid nitrogen to decrease the impact of phonons and leakage current. A photo-ionization spectrum usually shows a step-like structure. The photo-ionization step can be approximated by the Kopylov-Pikhtin model [111, 112]:

$$\sigma_{e-ph} \propto \int_0^{\infty} \frac{e^{-\frac{(E+E_{dl}-h\nu)^2}{\Gamma^2}}}{h\nu(E+E_{dl})^2}\sqrt{E}dE \quad . \tag{2.30}$$

Here, $\sigma_{e\text{-}ph}$ is the photo-ionization cross-section, as a parameter integrated over spectrum of electron energies E, E_{dl} is the photo-activation energy of a definite center and the electron-phonon coupling is defined by the broadening factor Γ. The photo-generated carriers of density $N(h\upsilon)$ induces a photo-current $i(h\upsilon)$ dependent on excitation photon energy $h\upsilon$:

$$i(h\nu) = \frac{q_e N(h\nu) S \mu U_R}{d} \tag{2.31}$$

where q_e is the elementary charge, S is the junction area, d is the diode base thickness, μ is the carrier mobility and U_R is the reverse bias voltage.

The broadening of the absorption onset is also related to the Huang-Rhys [111] and, consequently, to the Franck-Condon shift and the energy of the vibrational mode [111, 112]. The Huang-Rhys factor $S = d_{FC}/h\nu_0$ is a ratio between the Franck-Condon shift d_{FC} and the energy of the vibrational mode $h\nu_0$. The Huang-Rhys factor S quantifies the number of phonons emitted during optical transition [108]. The dependence of broadening parameter at absolute zero temperature can be determined by the equation [111]:

$$\Gamma_0 = \frac{\nu_g}{\nu_e}\sqrt{2d_{FC}\nu_g} \quad . \tag{2.32}$$

Here, ν_g and ν_e are the frequency of the ground and the excited state, receptively. Using $\nu_e = \nu_g = \nu_0$, it becomes:

$$\Gamma_0 = \sqrt{2d_{FC}\nu_0} \approx 1.414\nu_0 S^{1/2}. \tag{2.33}$$

The temperature-dependent broadening is then expressed as:

$$\Gamma = \Gamma_0\sqrt{2coth\,(h\nu_0/k_BT)}. \tag{2.34}$$

The pulsed photo-ionization has been implemented for spectroscopy of defects in GaN structures. There the Optical Parametric Oscillator serves as varied energy photon source. The photo-response of carrier density changes is recorded by microwave-probed photoconductivity (MW-PC) technique. This enables to simultaneously control variations of carrier lifetime. The photon-electron coupling ($\sigma_{e\text{-}ph,}$ Eq. 2.30) for carriers n_{d0} residing on a definite energy E_d level determines values of an absorption coefficient $\alpha(h\nu) = \sigma(h\nu)n_{d0}$ related to this level. The strength of the coupling is characterized by a spectrally varied cross-section $\sigma(h\nu)$. The density of photo-emitted carriers $n^*_d = \alpha(h\nu)F(h\nu)$ determines the peak value ($U_{MW\text{–}PC,0}$)~n^*_d~$\sigma(h\nu)$ at t=0) of the $U_{MW\text{-}PC}$ response for a fixed surface density $F(h\nu)=const$ of the incident photons. The surface density of the incident photons $F(h\nu)$ is evaluated by calibration of the energy/per pulse measurements within incident laser beam. The PPIS steps, recorded as $U_{MW\text{-}PC,0}(h\nu)$, represent spectral distribution of

$\sigma(h\nu)$. The shape $\sigma_L(h\nu)$ of the spectral steps and spectral position ($E_{d,L}$), ascribed to several L centres, serve for evaluation of the photo-activation energy $E_{d,L}$ and identification of the definite (L) defects. As usually, PPI spectrum contains a few spectral steps. The relative concentrations $N_{d,L}$ of different defects L can be evaluated by using a spectrum of an absorption coefficient $\alpha(h\nu)$ is independently measured on the same sample, and its correlation with $\sigma(h\nu) \sim U_{MW-PC,0}$, as $N_{d,L}(h\nu) = \alpha(h\nu)/\sigma_L(h\nu)$ is comprehensively examined. Actually, the density N_d of the L species centres coincides with a partial density of the equilibrium carriers n_{d0L} if L traps are completely filled. The proportionality of the n_{d0L} to N_{dL} can be assumed in the case of the close values of carrier capture lifetimes τ_C and rather large equilibrium carrier concentration in material before introduction of compensating centres. The considerable deviation from the mentioned assumptions leads to errors in estimation of trap concentration. To enhance precision, the dedicated experiments should be involved to determine the equilibrium occupation of definite defect states. The absolute values of $N_d \rightarrow N_T$ are roughly deduced by correlating the relative values of $N_{d,L}$ (re-plotting the $N_d(h\nu)$ scale) with known concentration of centres (for instance, Mg or C dopants) independently obtained for the same sample. The scale of the absolute values of $\sigma(h\nu)$ can then be obtained (by shifting an arbitrary scale to values of $\sigma_h(h\nu) = \alpha_h(h\nu)/N_h$) by using α_h values obtained for the range of rather homogeneous excitation $\alpha_h d << 1$, for the employed samples of thickness $d \approx 400$ μm.

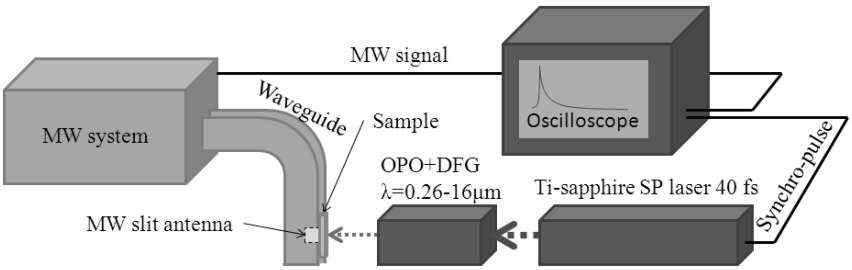

Fig. 2.6. A sketch of photo-ionization spectroscopy implemented by using OPO excitation and MW-PC probe.

The PPI spectroscopy was performed using excitation by fs and ns lasers equipped with optical parametric oscillators (OPO) (Fig. 2.6). The

femtosecond and nanosecond pulsed excitation has been combined to clarify the role of electron-phonon coupling in photo-ionization processes. A nanosecond OPO instrument Ekspla NT342B with pulse duration of 4 ns as well as wavelength tuning range from 210 to 2300 nm, and a Ti:sapphire laser based OPO system with pulse duration of ~40 fs as well as wavelength range of 350 – 2500 nm were employed. The MW-PC signal $U_{MW\text{-}PC}$ is proportional to a density of the photo-excited carriers, while their relaxation rate within a transient represents the carrier lifetime ascribed to later stages of trap filling/emptying. The sample was placed on a slit-antenna of the 21 – 22 GHz MW system and excited by OPO laser beam, starting from long wavelength wing to avoid simultaneous filling of several traps. The transients of the MW-PC response were recorded on 50 Ohm load resistor connected in series with MW detector by using a 2 GHz oscilloscope LeCroy Wave Runner 620Zi.

2.7. Synopsys TCAD platform for simulations of the pin and LGAD Si detectors

Conventional a p-type LGAD consisting of $n^+pp^-p^+$ layers with p-well formed by deep diffusion of boron (B) into p^- layer have been considered. However, it was shown that an effect of the 'acceptor removal' occurs in irradiated LGAD sensors which causes the loss of internal gain [1]. Radiation damage partially removes a boron from the multiplication layer, thereby reducing the effective doping concentration. Description of the acceptor removal has been approximated by phenomenological relation

$$N(\Phi) = N_0 \cdot e^{-b\Phi}, \tag{2.35}$$

where N is the dopant concentration (acceptor density), Φ is the irradiation fluence, and the parameter b is assumed to be a function of N_0. This detrimental effect might be partially suppressed by forming the n-well ($p^+nn^-n^+$) Si structure with the phosphorus doped an epitaxial (n-well) layer. In this work, the simulations of the operational characteristics for the p-type and n-type LGAD devices have been performed.

A functionality of LGAD device has been validated by digital experiments performed using of Technology Computer-Aided Design (TCAD) algorithms using the Drift-Diffusion (DD) approach. Simulations have been carried out employing a Sentaurus Device software platform.

3. EXAMINED CHARACTERISTICS OF THE APPLIED RADIATION DETECTOR MATERIALS

Knowledge about the specific material characteristics of sensors applied in detection of different radiations, exploited in high energy physics and radiation medicine, was collected and enhanced by research of electrical and optical features of materials exploited in fabrication of radiation detectors.

3.1. Transient electrical characteristics determined by majority carrier traps in electron irradiated SiGe detectors

In this section, the analysis of the electrical characteristics in pristine, electron irradiated and subsequently annealed $Si_{1-x}Ge_x$ samples with different Ge contents was performed. The routine capacitance deep-level transient spectroscopy (C-DLTS) and Laplace DLTS (L-DLTS) techniques [57, 58] were combined to clarify the deep trap spectrum. Correlation of the radiation defect parameters and Ge content in SiGe alloys was examined in the 25–260 K temperature range. Moreover, the annealing caused by transformations of the low-activation energy traps were revealed. Additionally, the growth-associated defects were unveiled only in pristine $Si_{1-x}Ge_x$ samples containing the largest Ge content values. The traps were identified by analysing the activation energy values reported in the literature. It was revealed that the carbon–oxygen metastable complexes (C_iO_i *) were transformed into the stable-state complexes (C_iO_i) under 125 °C annealing for 15 min of the irradiated samples.

The pristine and electron-irradiated $Si_{1-x}Ge_x$ diodes with an n^+p structure were examined. The diodes were fabricated using SiGe substrates grown using the Czochralski technique. The diode basis was formed from the *p*-type material (doped with boron), containing either 1%, 1.4% or 5.1% of Ge. For comparison, the diodes made of pure Si used the same (as the SiGe alloys) boron-doping parameters. Irradiation with 5.5 MeV electrons was performed at room temperature using a linear accelerator with electron fluxes of 2×10^{12} $cm^{-2}s^{-1}$. The Si as well as the $Si_{0.99}Ge_{0.01}$ alloy diodes were irradiated with fluence of 2×10^{15} cm^{-2}. The $Si_{0.986}Ge_{0.014}$ and $Si_{0.949}Ge_{0.051}$ alloy-based diodes were irradiated with fluences of 5×10^{13} cm^{-2} and 2×10^{14} cm^{-2}, respectively. The irradiated samples were consequently annealed at 125 °C for 15 min to investigate the changes of DLT spectra under heat treatment.

The DLT spectra were recorded using a commercial HERA-DLTS 1030 instrument (PhysTech GmbH, Moosburg an der Isar, Upper Bavaria, Germany). The DLTS measurements were performed using a routine C-DLTS

regime. These DLT spectra were examined in the temperature range of 15–280 K. The majority carrier trap spectra were recorded at reverse bias voltage (U_R) of 3 V and injection pulses (t_p) of 10 ms duration. Each spectrum was analysed by combining correlation functions and the Laplace method.

Up to seven spectral peaks (assigned to the E_1–E_7 traps, as illustrated in Figure 3.1b) were observed within C–DLT spectra recorded on the 5.5 MeV electron irradiated Si diode when using a fluence of $\Phi = 2 \times 10^{14}$ e/cm^2. Figure 1a shows the barrier capacitance changes with temperature (C_b–T) in the 5.5 MeV electron-irradiated and subsequently annealed Si samples. It can be noticed in Figure 1a that an onset within the C_b–T curves was obtained for the as-irradiated and subsequently annealed Si samples. The shift of the onset may have appeared due to the irradiation- and annealing-induced transformations and density variations of carrier trap species, which caused freezing of carriers within the temperature range under consideration [57]. A few peaks (for instance, E_6) changed their position under annealing relatively to an abscise scale implying the intricate transformation of traps assigned to this spectral peak. Such a spectral range was carefully examined (Figure 3.1d) using routine and Laplace transform DLTS (L-DLTS). It was clarified that the E_6 peak can be composed of two peaks $E_{6\text{-}1}$ and $E_{6\text{-}2}$, just after irradiation. These peaks were ascribed to traps with slightly different activation energies, and their values can be evaluated using Arrhenius plots (as shown within inset (i) for Figure 3.1d). The concentration and activation energy of traps attributed to the $E_{6\text{-}2}$ peak increased after annealing as can be deduced from Figure 3.1b,d. It is worth mentioning that only the $E_{6\text{-}2}$ peak remained after annealing (instead of the $E_{6\text{-}1}$ and $E_{6\text{-}2}$ as well as E_5 peaks), and its amplitude was close to the sum of the $E_{6\text{-}1}$ and $E_{6\text{-}2}$ as well as E_5 peaks before annealing. This implies that the changes in the E_5 and $E_{6\text{-}1}$ as well as $E_{6\text{-}2}$ spectral peaks actually represented transformations of the defects due to the annealing.

The evolution of radiation defects in *p*-type Si introduced by electron beam is rather well understood [29, 56]. Thereby, identification of the most resolved traps in Si can be reliably implemented based on activation energy values reported in the literature. Parameters for all the identified Si traps are presented in Table 3.1.

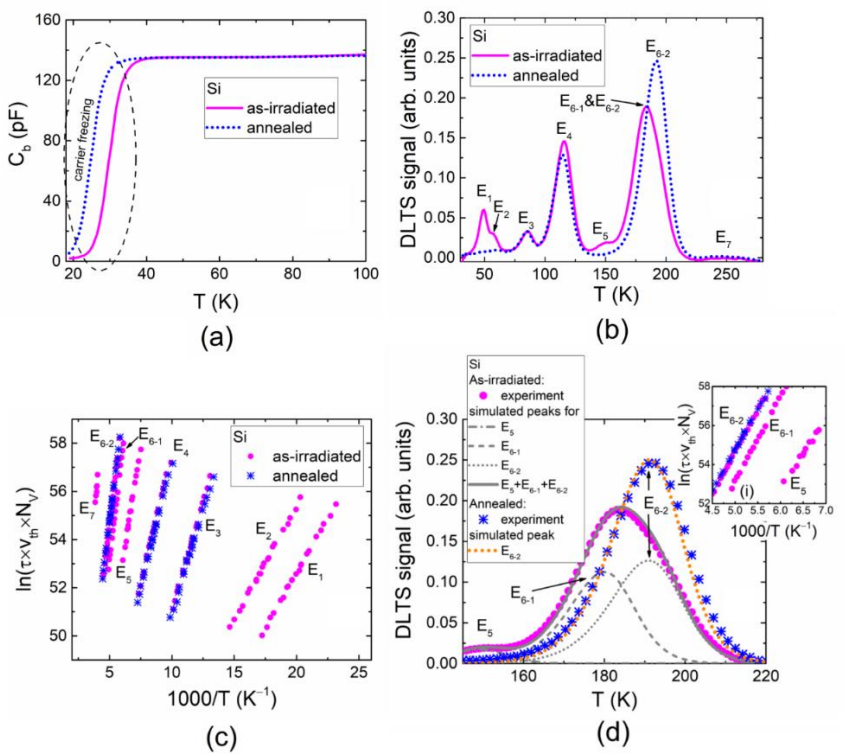

Figure 3.1. (**a**) The barrier capacitance dependence on temperature (C_b–T) obtained for 5.5 MeV electron irradiated and subsequently annealed Si samples. (**b**) Deep-level transient (DLT) spectra of the as-irradiated and annealed Si samples. (**c**) Arrhenius plots made for different traps. (**d**) The highlighted spectral range inherent for the E_5, E_{6-1} and E_{6-2} trap appearances. Inset (i) Arrhenius plots for traps E_{6-1} and E_{6-2}. Here, τ denotes the carrier lifetime relative to emission; υ_{th} is the carrier thermal velocity, and N_V stands for the effective density of hole states in the valence band.

The trap with the activation energy of 0.080 eV (E_1 in Table 1) is attributed to the double interstitial and oxygen (I_2O) complex [56]. The 0.100 eV (E_2) level can be assigned to a triple vacancy (V_3) [56]. The origin of the E_3 trap is not clear, however, it might be related to vacancy (V) [113]. The trap with activation energy of 0.190 eV (E_4) is associated with V_2 + V_3 complex [56, 114]. The trap with activation energy of 0.285 eV (E_5) is associated with a carbon interstitial (C_i) [56], while the close energy duplet of 0.360 (E_{6-1}) and 0.371 (E_{6-2}) are attributed to the metastable and stable forms of the carbon–oxygen (C_iO_i * and C_iO_i) complexes [114-116], respectively. After 15 min annealing at 125 °C, the unstable form of the carbon–oxygen complex seems to become the stable complex according to reactions [114]:

$$C_i + O_i \xrightarrow{reaction} C_iO_i^* + C_iO_i \xrightarrow{annealing} C_iO_i \quad (3.1)$$

The density of traps ascribed to the stable form of the carbon – oxygen (E_{6-2}) complex should hold the density of constituents, represented by the sum of E_5, E_{6-1} and E_{6-2} DLTS peaks before annealing. The alternative sequence of reactions in formation of the stable E_{6-2} complex would be as follows [114]:

$$I_2O \xrightarrow{annealing} I_2 + O \rightarrow O_i + C_i \xrightarrow{annealing} C_iO_i \quad (3.2)$$

The annealing out of E_1 and E_5 traps together with an increase in the amplitude of the E_{6-2} peak (Figure 3.1b) supports the predicted sequences of the reactions denoted in Equations (3.1) and (3.2).

The slight addition of Ge to get the $Si_{0.99}Ge_{0.01}$ alloy should not drastically modify the spectrum of Si radiation defects introduced using the same irradiation conditions ($\Phi = 2 \times 10^{15}$ cm^{-2}). Indeed, the structure of the DLT spectrum (illustrated in Figure 3.2a) and its changes after annealing of the electron-irradiated $Si_{0.99}Ge_{0.01}$ diode resembled that obtained in Figure 3.1. Other parameters for all the revealed traps in the $Si_{0.99}Ge_{0.01}$ alloy are presented in Table 3.2. These results indicate that values of the activation energy, ascribed to the E_1–E_7 traps in Table 3.1, are shifted to the low-energy range relative to those obtained for the Si of the same type and doping level.

Table 3.1. Traps revealed for the 5.5 MeV electron as-irradiated and subsequently annealed Si sample.

Sample	As-Irradiated			Subsequently Annealed			Origin of Defect According to [Reference]
DLTS peak	Activation Energy (eV)	Capture Cross-Section (cm^2)	Density of Traps (cm^{-3})	Activation Energy (eV)	Capture Cross-Section (cm^2)	Density of Traps (cm^{-3})	
E_1	0.080	1.36×10^{-15}	6.40×10^{12}				I_2O [18]
E_2	0.100	1.04×10^{-14}	3.24×10^{12}				V_3 [18]
E_3	0.157	5.72×10^{-15}	3.36×10^{12}	0.150	2.01×10^{-15}	3.55×10^{12}	V-related [23]
E_4	0.190	3.60×10^{-16}	1.55×10^{13}	0.185	1.88×10^{-16}	1.36×10^{13}	$V_2 + V_3$ [18,22]
E_5	0.285	4.69×10^{-15}	1.61×10^{12}				C_i [18,22]
E_{6-1}	0.360	9.32×10^{-15}	1.22×10^{13}				C_iO_i * [22]
E_{6-2}	0.371	4.25×10^{-15}	1.41×10^{13}	0.370	3.90×10^{-15}	2.66×10^{13}	C_iO_i [22]
E_7	0.500	4.46×10^{-15}	6.07×10^{11}				$I\text{-}C_i/I\text{-}B_i$ [25]

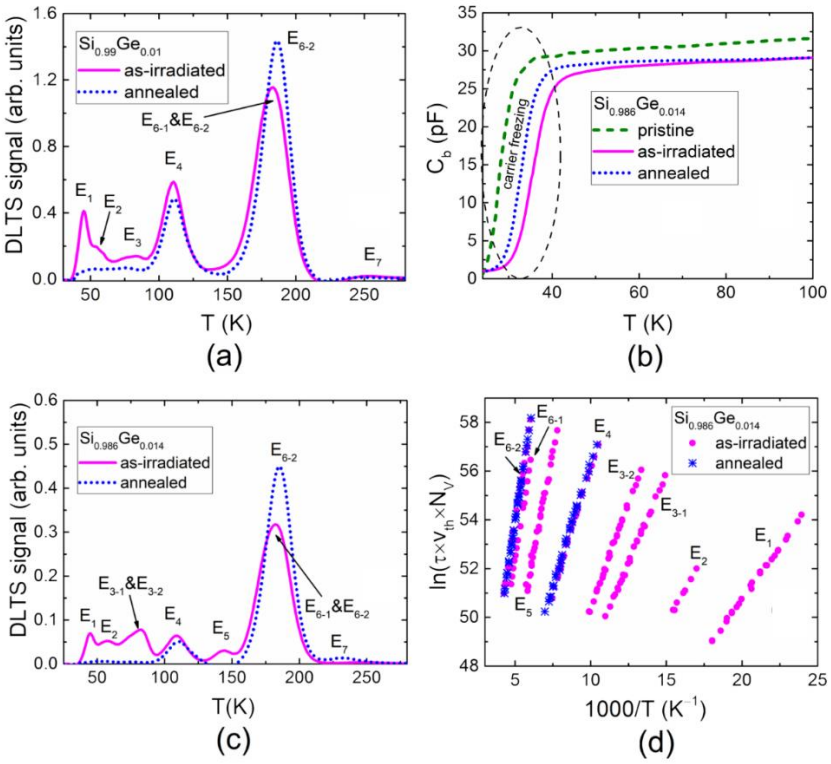

Figure 3.2. (**a**) DLT spectra recorded on the as-irradiated and annealed $Si_{0.99}Ge_{0.01}$ diode samples. (**b**) The barrier capacitance dependence on temperature (C_b–T) obtained for the pristine, 5.5 MeV electron irradiated and subsequently annealed $Si_{0.986}Ge_{0.014}$ samples. (**c**) DLT spectra recorded on the as-irradiated and annealed $Si_{0.986}Ge_{0.014}$ diode samples. (**d**) Arrhenius plots composed for different traps.

Another slight addition of Ge to obtain the $Si_{0.986}Ge_{0.014}$ alloy should further modify the spectrum of Si radiation defects. Figure 3.2b shows the barrier capacitance changes with temperature (C_b–T) in the 5.5 MeV electron-irradiated and subsequently annealed $Si_{0.986}Ge_{0.014}$ samples. However, together with the onset within the C_b–T curves, observed in Figure 3.1a, variations of the slope of the C_b–T curves can be noticed for the pristine, as-irradiated and subsequently annealed $Si_{0.986}Ge_{0.014}$ samples. These changes in the C_b–T curve onsets and slopes can be ascribed to irradiation and annealing-induced transformations and various trap species density variations that cause freezing of carriers within the temperature range under consideration [57, 117]. Indeed, the structure of the DLT spectrum (Figure 3.2c) and its changes after annealing of the electron irradiated $Si_{0.986}Ge_{0.014}$ diode resembles that obtained in Figure 3.1b. Moreover, it was observed that the E_3 peak was composed of

two peaks E_{3-1} and E_{3-2}, as obtained after irradiation of the $Si_{0.986}Ge_{0.014}$ alloy diode. The latter (E_{3-1} and E_{3-2}) peaks were ascribed to traps with slightly different activation energies, which had values that were determined by using Arrhenius plots (Figure 3.2d). The E_{3-1} and E_{3-2} peaks disappeared after annealing, thereby indicating the transformation of vacancy related defects.

Table 3.2. Summary of traps revealed for the as-irradiated and subsequently annealed SiGe samples with different Ge content.

Sample	As-Irradiated			Subsequently Annealed		
DLTS Peak	Activation Energy (eV)	Capture Cross-Section (cm^2)	Density of Traps (cm^{-3})	Activation Energy (eV)	Capture Cross-Section (cm^2)	Density of Traps (cm^{-3})
			$Si_{0.99}Ge_{0.01}$			
E_1	0.078	5.83×10^{-15}	3.00×10^{13}			
E_2	0.095	8.70×10^{-15}	1.07×10^{13}			
E_3	0.149	2.86×10^{-15}	1.08×10^{13}			
E_4	0.180	3.21×10^{-16}	4.79×10^{13}	0.180	3.07×10^{-16}	3.80×10^{13}
E_{6-1}	0.335	2.68×10^{-15}	3.51×10^{13}			
E_{6-2}	0.352	2.09×10^{-15}	6.13×10^{13}	0.351	2.24×10^{-15}	1.11×10^{14}
E_7	0.542	2.68×10^{-14}	1.40×10^{12}	0.523	2.49×10^{-14}	7.16×10^{11}
			$Si_{0.986}Ge_{0.014}$			
E_1	0.075	3.84×10^{-15}	1.18×10^{12}			
E_2	0.088	1.05×10^{-15}	8.05×10^{11}			
E_{31}	0.126	1.98×10^{-15}	4.65×10^{11}			
E_{32}	0.143	2.14×10^{-15}	6.02×10^{11}			
E_4	0.175	2.78×10^{-16}	1.09×10^{12}	0.175	2.03×10^{-16}	8.87×10^{11}
E_5	0.266	2.99×10^{-15}	5.03×10^{11}			
E_{6-1}	0.336	4.94×10^{-15}	2.60×10^{12}			
E_{6-2}	0.344	1.81×10^{-15}	4.25×10^{12}	0.346	5.56×10^{-15}	7.09×10^{12}
E_7				0.585	6.12×10^{-13}	1.10×10^{11}
			$Si_{0.949}Ge_{0.051}$			
E_{31}	0.117	5.42×10^{-15}	1.27×10^{13}			
E_{32}	0.127	5.09×10^{-15}	1.05×10^{13}			
E_4	0.170	2.00×10^{-16}	2.50×10^{12}	0.166	3.03×10^{-16}	2.37×10^{12}
E_5	0.233	3.38×10^{-15}	1.52×10^{12}			
E_{6-1}	0.297	1.94×10^{-15}	7.57×10^{12}			
E_{6-2}	0.312	1.12×10^{-15}	1.13×10^{13}	0.312	1.32×10^{-15}	2.13×10^{13}
E_7	0.585	6.12×10^{-13}	1.10×10^{11}			

The L-DLTS technique was additionally employed to separate the E_{6-1} and E_{6-2} traps more precisely. The trap activation energy values were evaluated using Arrhenius plots (Figure 3.2d). Parameters for all the unveiled traps are presented in Table 3.2. However, values of the activation energy ascribed to the E_1–E_7 traps, illustrated in Figure 3.2c and listed in Table 3.2, were close to those extracted from the $Si_{0.99}Ge_{0.01}$ spectra (Figure 3.2a). However, these activation energy values were slightly different from those

obtained for the Si diodes. The activation energy values extracted for $Si_{0.986}Ge_{0.014}$ diodes were again shifted to the low-energy range relative to those obtained for Si of the same conductivity type.

The rather different DLTS characteristics (relative to those of pure Si as well as of 1% and 1.4% Ge-containing SiGe alloy) were obtained for the 5.5 MeV electron-irradiated and subsequently annealed $Si_{0.949}Ge_{0.051}$ material diodes. Figure 3.3a illustrates the barrier capacitance changes with temperature (C_b–T) in the pristine, in the 5.5 MeV electron-irradiated and the subsequently annealed $Si_{0.949}Ge_{0.051}$ samples. The change in the slope of the C_b–T curves was inherent for all the pristine, the as-irradiated and the subsequently annealed samples. Again, the onsets within the C_b–T curves and slightly different slopes seem to appear due to the irradiation- and annealing-induced transformations and various traps species density variations [57, 117].

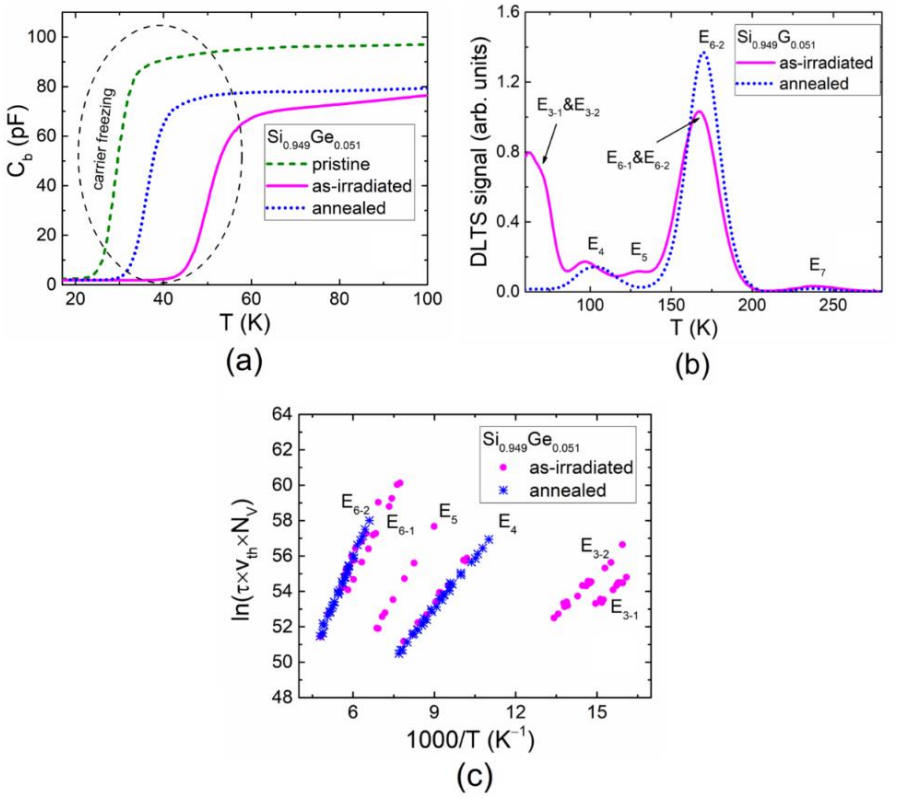

Figure 3.3. (**a**) The barrier capacitance dependence on temperature (C_b–T) obtained for pristine, 5.5 MeV electron irradiated and the subsequently annealed $Si_{0.949}Ge_{0.051}$ samples. (**b**) DLT spectra recorded on the as-irradiated and annealed $Si_{0.949}Ge_{0.051}$ samples. (**c**) Arrhenius plots made for different traps.

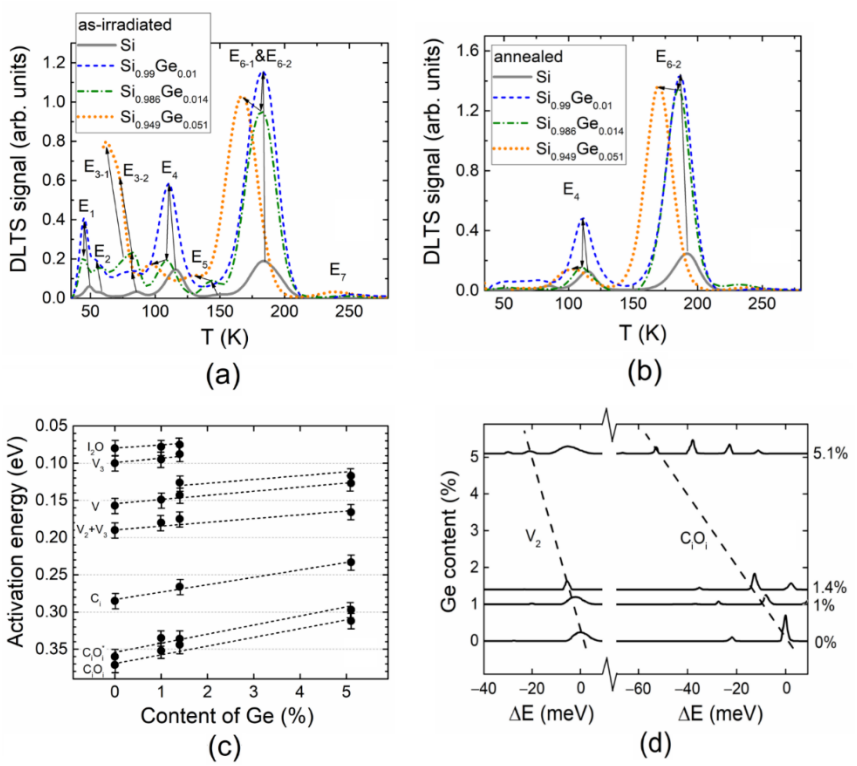

Figure 3.4. Comparison of the DLT spectra obtained in the as-irradiated (**a**) and annealed (**b**) Si and SiGe alloy samples. (**c**) The tendency of changes in the activation energy values of the radiation-induced traps in $Si_{1-x}Ge_x$ alloy as a function of Ge content. (**d**) Ge content dependent variations in the Laplace DLT spectra obtained for V_2 and C_iO_i radiation-induced defects.

The L-DLTS method was chosen to separate the traps inherent for low-temperature range (40–80 K) owing to the L-DLTS elevated resolution (up to 2 MeV). The DLT spectra recorded on the as-irradiated and annealed $Si_{0.949}Ge_{0.051}$ samples are illustrated in Figure 3.3b. However, the DLT spectra covered the temperature range >50 K. The barrier capacitance of the $Si_{0.949}Ge_{0.051}$ diodes vanished in the low temperature range (Figure 3.3a), and the application of the capacitance DLTS was then impossible [57]. The activation energies of the traps were evaluated using Arrhenius plots (Figure 3.3c). The spectra with two prevailing peaks, namely, E_4 and E_{6-2}, were again recorded after annealing at 125 °C for 15 min, similar to the regularity observed for the $Si_{0.986}Ge_{0.014}$ sample. The DLTS signatures for all the traps observed in $Si_{0.949}Ge_{0.051}$ samples are listed in Table 3.2. It was obtained that the activation energy values in the $Si_{0.949}Ge_{0.051}$ alloy were shifted even more

to the low-energy range relative to those obtained for the Si, $Si_{0.99}Ge_{0.01}$ and $Si_{0.986}Ge_{0.014}$ samples.

The comparison of the DLT spectra obtained in the as-irradiated (Fig. 3.4a) and annealed (Fig. 3.4b) Si and SiGe alloy samples is generalized in Figure 3.4 to clarify the activation energy shifts.

The tendency of changes in the activation energy values of traps in $Si_{1-x}Ge_x$ alloy as a function of Ge content is sketched in Figure 3.4c, based on DLT spectroscopy data obtained in this work. Additionally, the Laplace DLT spectra were re-plotted according to the re-calculation procedure described in Reference [118]. These L-DLT spectra are illustrated in Figure 3.4d to highlight the shifts in energy levels ascribed to V_2 and C_iO_i defects in the as-irradiated diodes. It can be inferred from Figure 3.4a,b, that the activation energy values decreased significantly with enhancement of the Ge content in the SiGe alloy, irrespective of the irradiation and annealing procedures. This activation energy variation was also independent of the DLTS peak amplitude changes. These results can be understood as an indication that the levels moved closer to the valance band [55, 119]. The peak shifts to the higher energy range with an increase in the Ge content was obtained for n-type SiGe alloys [120–122] conversely to those investigated in this work—*p*-type SiGe alloys. This effect can be explained either through an occupation of the radiation defect core by Ge atoms in the SiGe alloy due to the lattice parameter change or via lattice bond length variations which affect the conduction and valence band parameters of the SiGe alloy [55]. The opposite tendency within the observed DLTS peak shifts for the *p*-type and *n*-type SiGe alloys might be alternatively explained through the shifts of the Fermi level and the consequent filling of the radiation defect states.

Thereby, it was deduced from C-DLTS and L-DLTS spectra that the carbon/oxygen associated complexes prevailed in the pristine $Si_{0.949}Ge_{0.051}$ alloys. Irradiation with 5.5 MeV electrons led to considerable change in the DLT spectrum containing up to seven spectral peaks due to the introduction of the radiation defects. These defects have been identified using activation energy values reported in the literature. The double interstitial and oxygen (I_2O) complexes and the vacancy, di-vacancy and tri-vacancy ascribed traps were revealed in the irradiated samples. The interstitial carbon and the metastable as well as stable forms of the carbon–oxygen (C_iO_i * and C_iO_i) complexes were also identified for the irradiated SiGe alloys. It was found that the carbon–oxygen metastable complexes (C_iO_i *) were transformed into stable-state complexes (C_iO_i) under 125 °C annealing for 15 min of the irradiated samples. It was determined that the activation energy shifts of

radiation-induced deep traps to low values were defined by an increase in the Ge content of the SiGe alloy.

3.2. Electron irradiation induced transforms of minority carrier traps in p-type Si and Si1-xGex alloys

The Si and $Si_{1-x}Ge_x$ materials under consideration were grown using a Czochralski (CZ) pulling technique. The content of Ge was discretely varied in the range of $x = 0–0.05$. The alloys of $Si_{0.99}Ge_{0.01}$ and $Si_{0.95}Ge_{0.05}$ were then researched together with pure *p*-type boron-doped Si. The n^+p structure diodes were fabricated at Scientific-Practical Materials Research Centre (SP-MRC) of Belarus National Academy of Science (NAS). All the diodes were irradiated at Laboratory of Radiation Effects in SP-MRC of Belarus NAS using a linear electron accelerator (where 283 K temperature and flux of 2×10^{12} $cm^{-2}s^{-1}$ were kept). The 5.5 MeV electrons were chosen according to accessible characteristics of the linear accelerator, in order to have a prevalence of point radiation defects. Different fluences (Φ) in the range from 5×10^{13} cm^{-2} to 5×10^{14} cm^{-2}, were accumulated. Details on the irradiation regime can be found in [123].

Routine modes of the minority carrier deep-level transient spectroscopy by using electrical (MC-DLT) [124] and optical (MCT) [55, 57, 58] excess carrier injection were applied to highlight the minority carrier traps. A HERA-DLTS 1030 instrument (PhysTech GmbH) was employed to record the MC-DLT and MCT spectra using different correlation functions. The MCT regime was implemented using the continuous-wave IR light laser excitation (λ = 1064 nm) to homogeneously generate excess carriers within the depth of the sample. The IR light excitation was performed using illumination of the edge side of the diodes. The shortly illuminated samples were later kept in dark for 16 h to trace the stability of the B_iO_i complexes. The DLTS spectra were recorded for the temperature range of 65–280 K. The maximum densities (N_T) of radiation defects were significantly less ($N_T << N_S$) than those of dopants (N_S) to have the appropriate DLTS recording regimes. The densities of the electrically active dopants were evaluated to be less than 2×10^{15} cm^{-3}, Table 3.3. Thereby, a simple interaction of close defects can be assumed. The prevailing traps were identified by using the literature data defect activation energies denoted in Table 3.4 together with references.

Table 3.3. The boron dopant concentration in diodes composed of Si and SiGe alloy evaluated using C-V characteristics.

Sample	N_S (cm^{-3})
Si	1.8×10^{15}
$Si_{0.99}Ge_{0.01}$	1.4×10^{15}
$Si_{0.95}Ge_{0.05}$	1.9×10^{14}

A barrier evaluation technique using the linearly increasing voltage (BELIV) pulses, described in Chapter 2 [97], was additionally applied to clarify the role of the majority and minority carrier traps that appeared as the overlapping opposite polarity peaks within DLT spectra. There, the temperature- and illumination-dependent BELIV characteristics were examined. The barrier capacitance charging, the diffusion and thermal emission current components can be revealed and analyzed by recording the BELIV current transients. A closed-cycle He cryogenic system of the HERA-DLTS 1030 instrument together with diode mounting arrangement was employed to implement the BELIV measurement instrument. The same as in the DLTS experiments, continuous-wave IR light laser was employed for additional illumination of the sample.

Table 3.4. The electron traps revealed in the 5.5 MeV electron-irradiated Si, $Si_{0.99}Ge_{0.01}$ and $Si_{0.95}Ge_{0.05}$ diodes using MC-DLT and MCT spectra.

MC-DLT				MCT		
p-Si						
trap	E_T (eV)	N_T (cm^{-3})	DO	trap	E_T (eV)	DO
				E1	0.150 ± 0.005	VO [5]
E2	0.240 ± 0.005	6.93×10^{13}	B_iO_i	E2	0.240 ± 0.005	B_iO_i [2,5,18]
				E3	0.420 ± 0.005	V_{cl} [5]
$p\text{-}Si_{0.99}Ge_{0.01}$						
trap	E_T (eV)	N_T (cm^{-3})	DO	trap	E_T (eV)	DO
				E1	0.160 ± 0.005	VO
E2	0.240 ± 0.005	1.06×10^{14}	B_iO_i	E2	0.240 ± 0.005	B_iO_i
				E3	0.420 ± 0.005	V_{cl}
$p\text{-}Si_{0.95}Ge_{0.05}$						
				trap	E_T (eV)	DO
				E1	0.240 ± 0.005	VO
				E2	0.280 ± 0.005	B_iO_i
				E3	0.440 ± 0.005	V_{cl}

To control the boron dopant concentration (N_S) within the base region, the diodes composed of Si and SiGe alloy of varied Ge content were examined by measuring conventional capacitance–voltage characteristics. The reverse bias U_R was increased up to 5 V. The capacitance C was measured using a 1 MHz frequency test signal. The dopant concentration was extracted by analysing a slope of the C^{-2}-U_R curve. The extracted values of the dopant concentration N_S in diodes composed of different Ge content material are listed in Table 3.3.

The close values ($1.8 > N_S > 1.4$) × 10^{15} cm^{-3} of boron dopant concentration in diodes composed of Si and SiGe alloy with rather small Ge (≤1%) content were obtained. However, an enhancement of the Ge content within SiGe alloy to 5% leads to a clear reduction (nearly about one order of magnitude, i.e., to 1.9×10^{14} cm^{-3}) in electrically active B impurities.

The DLT spectra measured in electron-irradiated Si diodes under electrical (MC-DLT) and optical (MCT) carrier injection are illustrated in Figure 3.5a and Figure 3.5b, respectively. The competition of the majority (H1 and H2) and minority (E1–E3) carrier traps can be deduced from the MC-DLT and MCT spectra, especially, in the range of H1 and E2 spectral peaks (within MC-DLT spectrum, Figure 3.5a) and H2 and E3 spectral peaks (within MCT spectrum, Figure 3.5b), respectively. The positive polarity spectral peaks are then assigned to the hole traps, while the negative peaks are related to the electron traps. A simulation of the overlapping spectral peaks is inevitable to highlight the defects and to extract the spectral parameters of the appropriate carrier traps. It can be deduced from Figures 3.5 a, b that spectral positions of the H1 and E2 peaks, as well as those of the H2 and E3 traps, are corrected under simulation of counter-polarity spectral peaks. Moreover, it was clarified the overlapping spectral peaks H2-1 and H2-2 associated with majority carrier traps (Figure 3.5b). The peaks related to stable and metastable states of E2 trap were distinguished by short IR-illumination of the diode edge and prolonged (16 h) retention at 293 K temperature in dark of the illuminated sample. The measurements of the MCT spectra were performed, varying retention time to trace stability of traps after illumination–retention procedures. The MCT spectra were compared for the longest retention time, sufficient to stabilize the trap filling. The specified trap activation energy values were extracted using Arrhenius plots for different peaks obtained in MC-DLT and MCT spectra, as illustrated in Figure 3.5c.

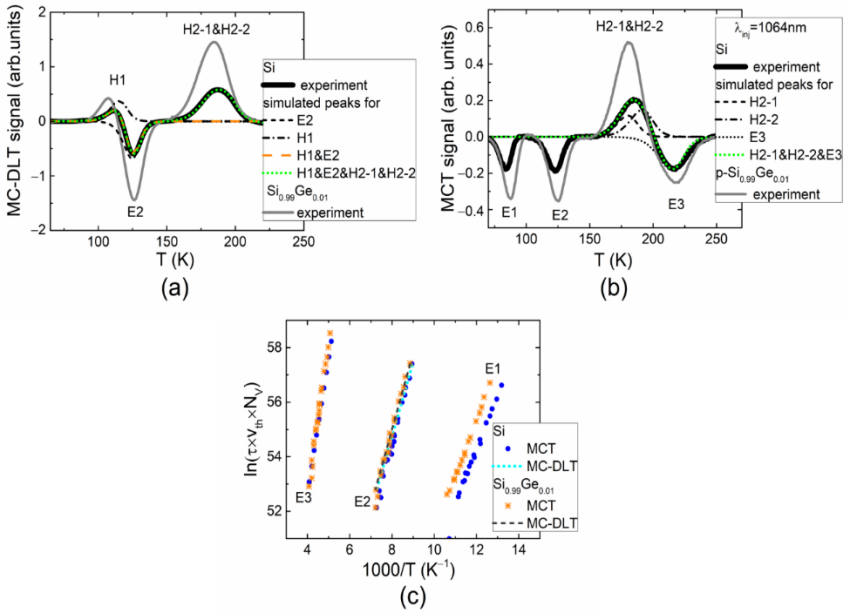

Figure 3.5. (**a**) The MC-DLTS spectra (solid curves) recorded under electrical carrier injection in 5.5 MeV electron-irradiated and boron-doped Si and $Si_{0.99}Ge_{0.01}$ diodes (the dot curve represents the simulated spectrum, including all the traps inherent for the IR illuminated diode after prolonged (16 h) retention in dark (at 293 K temperature); (**b**) The MCT spectra (solid curves) of the same Si and $Si_{0.99}Ge_{0.01}$ diodes recorded under optical injection implemented by short IR illumination of the diode edge and prolonged (16 h) retention in dark of the illuminated sample at 293 K temperature. Here, black curves represent spectra obtained for Si, while grey curves show these spectra recorded for $Si_{0.99}Ge_{0.01}$ diodes, and the dotted curves illustrate the simulated spectral peaks. (**c**) Arrhenius graphs plotted for different peaks in MC-DLT and MCT spectra. Here, τ denotes carrier lifetime relative to emission; υ_{th} is the carrier thermal velocity; N_V is the effective density of free carrier states.

The tentative identification of traps revealed in DLT spectra of boron-doped and electron-irradiated p-Si was performed by comparing values of activation energy extracted from Arrhenius plots and those reported in the literature, as indicated in Table 3.4. The hole trap H1 is assigned to the multi-vacancy ($V_2 + V_3$), while H2 trap with components H2-1 and H2-2 is related to the carbon–oxygen complex, with H2-1 being the metastable state (C_iO_i*) and H2-2 the stable state of this interstitial complex, respectively [124]. The minority carrier trap E1 with activation energy of 0.150 ± 0.005 eV can be associated with a vacancy–oxygen complex (VO) [48]. The electron trap E2 characterized by activation energy of 0.240 ± 0.005 eV can be ascribed to the

interstitial boron–interstitial oxygen complex (B_iO_i) [48, 56, 125]. The MCT spectra recorded after IR illumination and followed retention in dark for 16 h showed that the B_iO_i complex is in a stable state $B_iO_i^A$ of maximum concentration. This defect plays a major role in the "acceptor removal" processes. Overlapping of the counter-polarity peaks, as well as optical carrier injection of carriers implemented by illumination of the diode edge, leads to difficulties in estimation of concentration of minority carrier traps. Eventually, the spectral peak E3 with activation energy of 0.420 ± 0.005 eV can be associated with a vacancy cluster (V_{cl}) [48]. The parameters, such as the density (N_T) of traps, their activation energy E_T and defect origin (DO), are summarized in Table 3.4.

Nearly the same structure of spectra (relatively to those measured in p-Si) was obtained in $Si_{0.99}Ge_{0.01}$ diodes using MC-DLT and MCT modes of the DLTS recording (Figures 3.5a,b, grey curves). A slight shift of spectral peaks toward the higher temperature can be resolved for $Si_{0.99}Ge_{0.01}$ material diodes relatively to those recorded in p-Si. Additionally, the increased amplitudes of the spectral peaks (~N_T) were obtained in $Si_{0.99}Ge_{0.01}$ diodes within both MC-DLT and MCT spectra. This result may appear due to different concentrations of electrically active boron (N_S~1/N_T) in Si and $Si_{0.99}Ge_{0.01}$, as indicated for N_S values in Table 3.3. The activation energy values were extracted using Arrhenius plots, which almost coincide for *p*-type Si (Figure 3.5c) and $Si_{0.99}Ge_{0.01}$ diodes. It was inferred that the same radiation-induced minority carrier traps prevail within *p*-type Si and $Si_{0.99}Ge_{0.01}$ materials, as listed in Table 3.4.

However, modifications of the MC-DLT and MCT spectra of minority carrier traps clearly depend on the fluence of electron irradiation and on content of Ge in $Si_{1-x}Ge_x$ diodes. A comparison of the MC-DLT spectra in 1% and 5% Ge containing $Si_{1-x}Ge_x$ diodes and irradiated with nearly the same electron fluence of 2×10^{14} e/cm^2 is illustrated in Figure 3.6a. Here, no expressed minority carrier traps were obtained in $Si_{1-x}Ge_x$ diodes with 5% Ge, while a clear E1 peak associated with electron traps can be observed in MC-DLT spectrum recorded for $Si_{1-x}Ge_x$ diode with 1% Ge. Moreover, an increase in the majority carrier trap density with electron irradiation fluence can be easily deduced from Figure 3.6b, where the MC-DLT spectra recorded for $Si_{0.95}Ge_{0.05}$ diodes irradiated with fluences of 2×10^{14} cm^{-2} and 5×10^{14} cm^{-2} are compared. This observation can be understood assuming too small a density of electrically injected minority carriers and prevalence of the majority carrier traps of relatively large concentration. The appearance of the minority carrier traps within MCT spectra (Figure 3.6c) obtained using optical injection of excess carrier pairs in electron-irradiated 5% Ge containing $Si_{1-x}Ge_x$ diodes

supports this hypothesis. There, both the minority and majority carrier trap associated DLT spectral peaks can be clearly resolved. Nevertheless, the DLTS peak position shifts with content of Ge, and irradiation fluence of $Si_{1-x}Ge_x$ diodes can be clearly noticed in Figures 3.6a,c. However, the overlapping of these peaks aggravates separation of the activation energy of the prevailing radiation defects. Spectral peak positions were partially corrected by simulating competition of traps (illustrated in Figure 3.6c) in the formation of the DLT signals. The Arrhenius plots of minority carrier peaks within MCT spectra of the $Si_{0.95}Ge_{0.05}$ diodes irradiated with fluences of 2×10^{14} cm^{-2} and 5×10^{14} cm^{-2} of the 5.5 MeV electrons are illustrated in Figure 3.6d.

Three minority-carrier-trap-related MCT spectral peaks (E1-E3, Figure 3.6c) were resolved for $Si_{0.95}Ge_{0.05}$ material diodes. These radiation defects can be identified using activation energy values extracted from Arrhenius plots illustrated in Figure 3.2d. The E1 peak with $E_{T,1} \cong 0.24$ eV seems to be assigned to the vacancy–oxygen complex (VO) [48]. However, this E1 peak was not resolved within MC-DLT spectrum (Figure 3.6b). The E2 peak in the MCT spectrum of $Si_{0.95}Ge_{0.05}$ diode with $E_{T,2} \cong 0.28$ eV seems to indicate a competition between the minority carrier traps assigned to the interstitial boron–interstitial oxygen complex (B_iO_i) and to either a double-charged di-vacancy ($V_2^{0/=}$) or vacancy clusters (V_{cl}). The density of VO traps (E1) clearly increases with fluence for Ge-rich $Si_{0.95}Ge_{0.05}$ samples, as can be inferred from Figure 3.6c. In this case, boron (B) hardly participates in transformation of the E2 centers associated with B_iO_i complex due to a reduced concentration of the electrically active boron dopants (Table 3.3). The E3 peak with activation energy $E_{T,3} \cong 0.44$ eV, resolved within MCT spectrum of the $Si_{0.95}Ge_{0.05}$ material diode, corresponds to the vacancy clusters (V_{cl}). This result was implied from consideration of the amplitudes of the minority (E3) and majority (H2) carrier trap spectral peaks and their density changes with irradiation fluence. The shifts of the minority carrier activation energy with irradiation fluence are more pronounced in $Si_{1-x}Ge_x$ material diodes (Figure 3.6c) in comparison with those values obtained for diodes composed of Si (Figure 3.5b).

Variations of the BELIV transient dependent on temperature and injection were examined to resolve the competition of the minority and majority carriers, as well as to clarify the role of the barrier capacitance in the formation of the DLT spectra. The recorded transients, the measured barrier capacitance temperature dependences in SiGe alloy containing different concentrations of radiation-induced traps, as well as the transients simulated

through varying the parameters of carrier traps and measurement regimes (temperature, illumination), are illustrated in Figures 3.7 and 3.8.

A comparison of the temperature-dependent BELIV transients, recorded in *p*-type Si (Figure 3.7a) and SiGe (Figure 3.7c) alloy diodes in dark, shows a modification of the initial stage of the BELIV transients. The delay in the peak formation within BELIV transients increases with a reduction in temperature. The appearance of the lowest initial step of the BELIV current at temperatures < 150K correlates well with temperature-dependent barrier capacitance characteristics (Figure 3.8a) measured using a HERA-DLTS 1030 instrument. This step is formed due to the fast capture and release of the minority carriers, which modifies the resistance of depletion and transient layers.

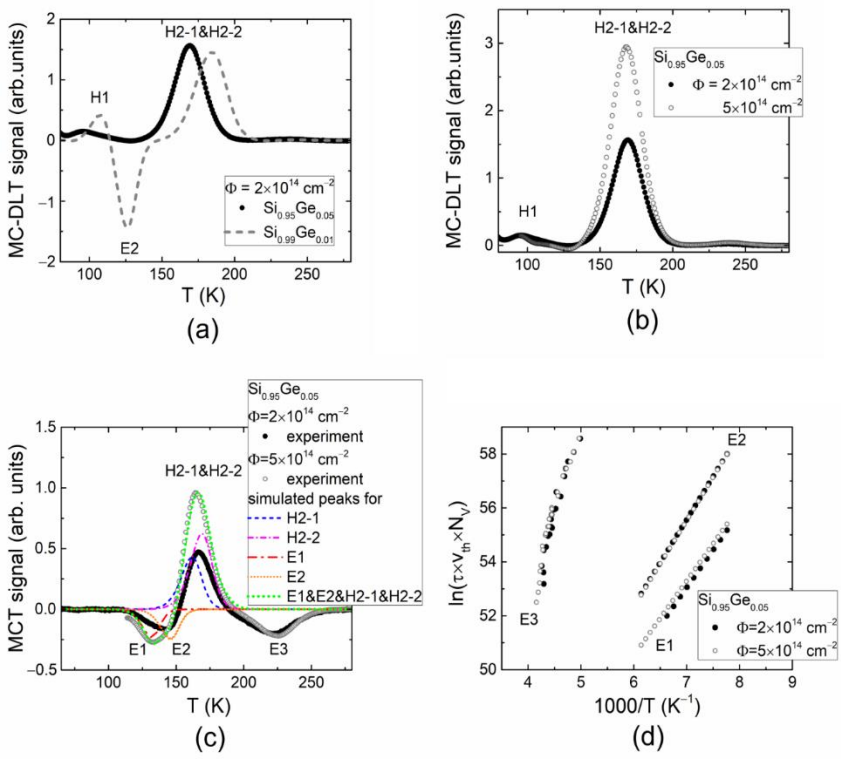

Figure 3.6. (**a**) Comparison of the MC-DLT spectra recorded by electrical injection of the excess carriers in the 2×10^{14} cm^{-2} fluence electron-irradiated $Si_{0.99}Ge_{0.01}$ and $Si_{0.95}Ge_{0.05}$ diodes; (**b**) Comparison of MC-DLT spectra recorded in $Si_{0.95}Ge_{0.05}$ diodes irradiated with 2×10^{14} cm^{-2} and 5×10^{14} cm^{-2} fluence where only majority carrier trap associated peaks are observed; (**c**)

Comparison of the MCT spectra recorded in $Si_{0.95}Ge_{0.05}$ diodes irradiated with 2×10^{14} cm^{-2} and 5×10^{14} cm^{-2} 5.5 MeV electron fluence using optical injection of the excess carrier pairs. Here, the dotted curves illustrate the simulated spectral peaks ascribed to different traps. (**d**) Arrhenius graphs plotted for different peaks in MC-DLT and MCT spectra.

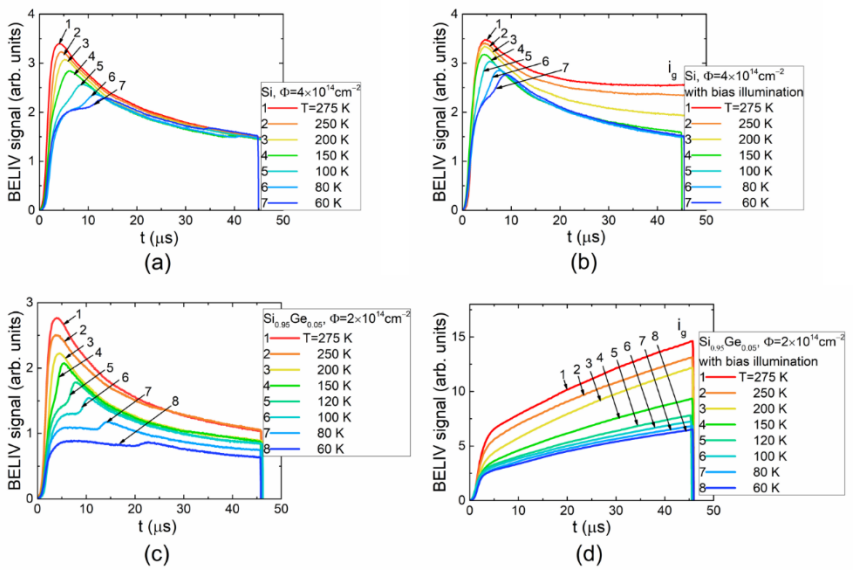

Figure 3.7. (**a**–**d**) Temperature-dependent BELIV transients in Si and $Si_{1-x}Ge_x$ diodes measured in dark (**a**,**c**) and under (**b**,**d**) laser illumination.

This also determines the time- and temperature-dependent $RC_{b0}(t,T)$ of the diode. The rather short capture/emission of minority carriers leads to an increase in the product (RC_{b0}) of the diode resistance R with time and a fixed value $C_{b0} \cong C_{geom}$ (Figure 3.8b) of barrier capacitance close to the geometrical (C_{geom}) one. The duration of this initial step of the BELIV current increases with a reduction in temperature, where current amplitude is nearly invariable. The carrier generation current, as well as the thermal emission lifetime, ascribed to either majority or minority carriers, can be evaluated using current value at the end of a BELIV pulse. The recorded transient usually contains the displacement and conductivity current components. The conductivity component arises within the transitional layer at the depletion boundary when the trapped carriers (n_T) with steady-state concentration n_{T0} are exponentially released $n_T(t) = n_{T0}\exp(-t/\tau_g)$. The thermal emission lifetime [54]

$$\tau_g = \frac{\exp(E_T / kT)}{\sigma v_T N_C}. \quad (3.3)$$

is a function of several parameters: the emission cross-section σ, the thermal velocity v_T, the density of states N_C in the free carrier band and of activation (E_T), as well as of thermal (kT) energy. The generation currents [55] from both the shallow and deep traps act simultaneously, leading to the leakage current, which is expressed as $i_g(t) = en_iW(t)S/\langle\tau_g\rangle$ through the averaged lifetime $\langle\tau_g\rangle$, where the impact of shallow centres manifests within initial stages of generation current transients. The carrier emission time decreases and density of the empty capture emission centres increases with enhancement of temperature due to the change of thermal emission factor, while steady-state bias illumination saturates a filling of the carrier capture centres. The changes of material resistance R are dependent on the content of alloy components; irradiation parameters can also significantly modify the BELIV transients. The BELIV transient appears as a square-wave pulse in high resistivity or insulating material when barrier capacitance approaches a geometrical capacitance value.

Then, the carrier release lifetime can be related to minority carrier thermal emission lifetime, according to Equations (2.19 and 3.3). Variation of the depleted diode resistance (R) increases in time $R \sim 1/n = \exp(t/\tau_{g,min})/n_{T0}$. The barrier capacitance restores to its value inherent for a diode, governed by the majority carrier concentration, after minority carriers are completely extracted. This instant depends on minority carrier lifetime (which increases nearly reciprocally relative to temperature) and majority carrier concentration (which decreases with temperature and depends on trap filling, modified by the external illumination), as described in [54]. Such modifications of the BELIV transient shape can be simulated by varying time- and temperature-dependent parameters of diode barrier capacitance and resistance, as illustrated in Figure 3.8a. Indeed, the carrier emission lifetime depends on trap parameters, activation energy and capture cross-section. The minority carrier lifetime as a function of temperature extracted for p-type Si and $Si_{0.95}Ge_{0.05}$ is illustrated in Figure 3.8c.

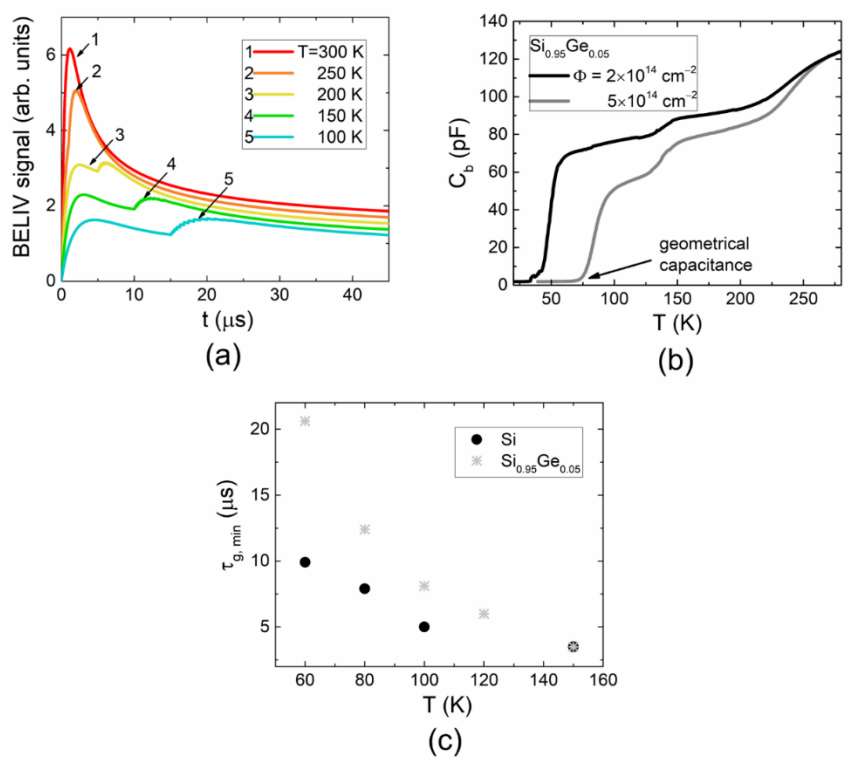

Figure 3.8. (**a**) Simulated variations (using Equations (1) and (3)) of the BELIV transients assuming changes of material resistivity, concentration of injected carriers, as well as minority and majority carrier traps of different generation lifetime. (**b**) Temperature-dependent barrier capacitance (C_b) variations in diodes containing different concentration of radiation-induced traps, where C_b approaches a geometrical value due to full extraction of thermally emitted carriers. (**c**) Minority carrier thermal generation lifetime as a function of temperature measured by BELIV technique in *p*-type Si and SiGe alloy.

It can be deduced from the results of simulations illustrated in Figure 3.8 that minority carrier emission lifetime in SiGe alloy is significantly longer than that in Si. This result hints at the deeper trap level associated with the same species defect in SiGe alloy relative to Si. The overall reduction in BELIV current with temperature (in Figures 3.7a,c) simply indicates a decrease in free carrier concentration in both materials. An enhancement of the excess carrier density through the external illumination (Figures 3.7b,d) is followed by the BELIV current increase, which is mainly caused by the generation current term (Equations 2.19 and 3.3). The BELIV current values (at the ultimate instant of the transients) approach (Figure 3.7b) or even exceed

(Figure 3.7d) the BELIV peak current. The density of the minority carrier emission traps in SiGe alloys seems to be significantly larger than that of Si, as the initial step of the BELIV current is hidden (Figure 3.7d) by generation current term. The BELIV current values at the ultimate instant t_p can be employed for comparison of the generation currents in i_g-T plots. A clear prevalence of the generation current in SiGe alloys (Figure 3.7d) also hints that the radiation-induced minority carrier trap density is enhanced in *p*-type SiGe alloy diodes relative to that in p-Si diodes.

Electron irradiations mostly determine an introduction of point radiation defects (Table 3.4). It had been shown [126] that gamma irradiations of 10 kGy dose did not change significantly the conductivity of the SiGe material, while neutron irradiations sharply decreased material conductivity to 0.14% of non-irradiated material. As shown in [55], the same type of radiation defects in Si and SiGe alloys are introduced by hadron irradiations in the range of moderate energy and fluence. Nevertheless, the type inversion of n-Si had been observed [127] under Co^{60} gamma irradiations in the range (>250 Mrad) of extremely large doses. However, the appearance of the acceptor removal phenomenon and type inversion in *p*-type Si significantly depends on oxygen impurity content within pristine Si material. Therefore, the resolved VO centers within DLTS can be an indication of B acceptor removal probability in *p*-type Si and SiGe. Variations of the density of B_iO_i centers and of electrically active B obtained in our research are in line with those [128] observed in p-Si irradiated with nuclear reactor neutrons over a wide range of fluences. The activation energy shifts of carrier traps, dependent on Ge content in SiGe alloys, obtained in this research, correlate rather well with such characteristics obtained in SiGe materials irradiated with electrons, protons, alpha particles and heavy ions [129,130]. However, it had been shown [33] that the production of extended defects can be suppressed in SiGe thin layers by hadron irradiations.

Variations of the activation energy values of radiation-induced traps extracted from MC-DLT (Figure 3.5a) and MCT (Figure 3.5b) spectra recorded in Si, $Si_{0.99}Ge_{0.01}$ and $Si_{0.95}Ge_{0.05}$ diodes are illustrated in Figure 3.6. Shifts of the DLTS peaks ascribed to majority and minority carrier trap can be inferred from these (Figure 3.6a,b) with the change of Ge content in SiGe alloys. The majority carrier trap ascribed peaks shift to the low-temperature wing of the DLT spectra with enhancement of Ge content within the SiGe alloy. The opposite tendency in variation of the activation energy of minority carrier traps with Ge content was revealed (Figure 3.6c). It was found that activation energy increases with Ge percentage. This result is supported by the BELIV characteristics, where a deeper trap level associated with the same

species defect in SiGe alloy relative to that in p-Si can be inferred from Figure 3.6c. This shows the contrary result relative to n-type silicon–germanium alloys [33,50] where the enhancement of the majority carrier activation energy with Ge content is inherent. In *p*-type SiGe (Figure 3.6a), the activation energy of majority carrier traps shifts to the lower energy values with an increase in Ge content [50,119].

In MC-DLT spectra (Figure 3.9a), the peak amplitude (E2) of minority carrier traps ascribed to the interstitial boron–interstitial oxygen complex (B_iO_i) is rather weak for the silicon–germanium alloy with a Ge content of 5%. It has been shown [131, 132] that Ge content modifies the density of the interstitial boron (B_i). The boron activation energy also varies depending on local strain induced by difference in radius of the surrounding atoms. An enhancement of Ge content within SiGe compensates the local strain [131] and thereby leads to a reduction in B_i density. Consequently, this serves to explain a decrease in B_iO_i centers and E2 peak intensity within MC-DLT spectrum (Figure 3.9a). On the other hand, this leads to a decrease in the electrically active dopants [132], i.e., of N_S. This result proves the obtained relations among N_S values in Table 3.3 dependent on Ge content and emulates variations of B solubility dependent on local strain. However, simultaneous action of different states [131] formed from B surrounded by Si (B-Si) atoms, and B surrounded by Si together with Ge (Si-B-Ge) atoms, stabilizes the density of the electrically active dopants (B_S). The changes in Ge content perturb the ratio of the B-Si and Si-B-Ge states within crystal bulk and thereby local strain and density of N_S. This might be a reason for the metastability of B_iO_i complexes, which appeared in two configurations of [$B_iO_i^A$] and [$B_iO_i^B$] [133-135]. Additionally, it had been concluded that most of the strain in SiGe is accommodated by variations of both the bond angle and bond length. The latter parameter also determines the changes in the formation energy of defects [136].

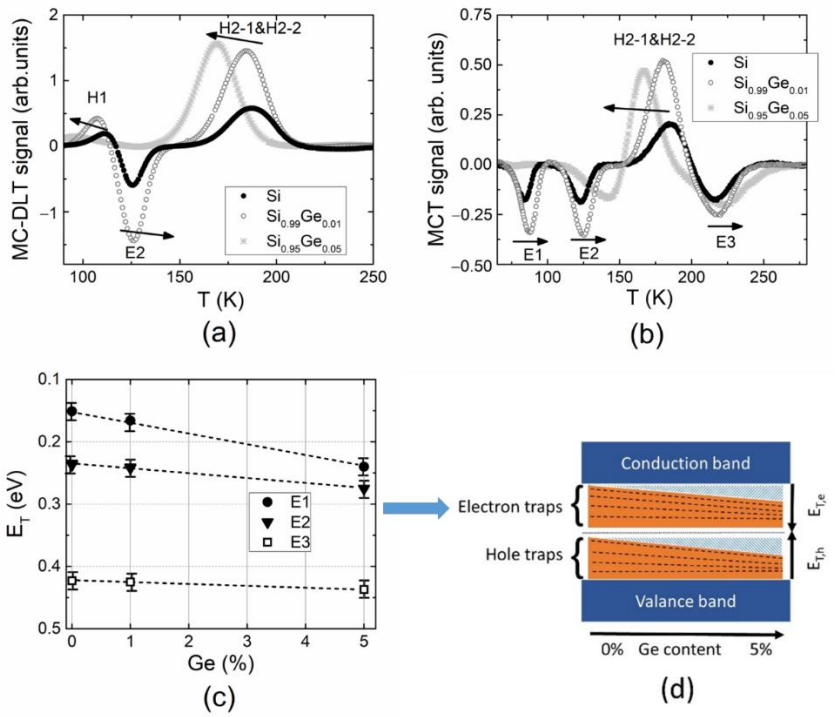

Figure 3.9. Comparison of MC-DLT (**a**) and MCT (**b**) spectra obtained in the 5.5 MeV electron-irradiated Si, $Si_{0.99}Ge_{0.01}$ and $Si_{0.95}Ge_{0.05}$ diodes; (**c**) The activation energy values (E_T) of the radiation-induced traps (E1–E3) of minority carriers as a function of Ge content; (**d**) A tentative scheme of the band gap variation in *p*-type $Si_{1-x}Ge_x$ material and related activation energy changes in the minority carrier traps depending on the Ge content.

The indirect band gap in SiGe alloys appears between Γ- Δ valleys as it does in Si crystals, and its value as a function of Ge content is described by expression [137, 138]

$$E_{gx}^{\Delta}(x) = 1.155 - 0.43x + 0.206x^2. \quad (3.4)$$

In this case, the bandgap of $Si_{0.95}Ge_{0.05}$ alloy differs from that value of Si by ~0.021 eV. Diamond structure of $Si_{1-x}Ge_x$ still exists, as long as the Ge content is either less than 10% or more than 85%. Otherwise, SiGe will probably become a random alloy [48]. The enhancement of Ge content in SiGe alloy could also lead to the formation of an impurity band [139, 140]. A tentative sketch of the bandgap in *p*-type $Si_{1-x}Ge_X$ alloys and arrangement of the radiation defect levels as a function of Ge content are presented in Figure 3.9d. Here, it is assumed that the alloy lattice still has a diamond structure. Even a small amount of substitutional Ge atoms modifies the value of energy level due to an increase in compress strain in the silicon–germanium alloy.

The shifts of the activation energy of minority and majority carrier traps exhibit the opposite character, i.e., the activation energy (E_{Te}) of the minority carrier traps increases, while the activation energy (E_{Th}) of the majority carriers decreases due to an increase in Ge content in the SiGe alloy. This trend will probably continue until it turns into a random alloy (a polycrystalline material).

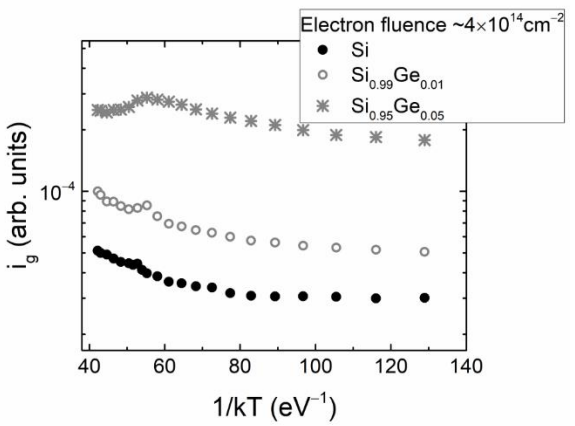

Figure 3.10. Generation current variations as a function of the inverse thermal excitation energy measured in samples under IR laser illumination.

The generation current dependence on the reciprocal thermal energy ($1/kT$) (Figure 3.10) extracted using BELIV current values at the ultimate instant t_p (Figure 3.7) shows a two-componential characteristic. This implies competition between the minority and majority carrier traps within a definite range of temperatures. The elevated temperature wing ($1/kT$ = 40–58) of this characteristic seems to be related to the majority carrier traps (H2), according to the temperature-dependent modifications of the BELIV transients (Figures 3.7a,c). The slopes of the $i_{g\ vs.}\ (kT)^{-1}$ characteristics obtained for p-type Si and SiGe alloys nearly coincide for the $(kT)^{-1} > 60$ (low temperature) range. This indicates that the same minority carrier trap (probably E2) prevails there.

The prevailing defects and transformations of the minority carrier traps in 5.5 MeV electron-irradiated *p*-type $Si_{1-x}Ge_x$ alloys, with *x* varied in the range of 0–0.05, were examined in the temperature range of 65–280 K by the deep-level transient spectroscopy (DLTS) using electrical (MC-DLT) and optical (MCT) excess carrier injection modes. The bi-stable boron–oxygen (B_iO_i) complex was revealed to be the prevailing minority carrier trap in *p*-type $Si_{1-x}Ge_x$ alloy diodes. The relatively small density of electrically active boron–oxygen complexes in SiGe alloy with 5% of Ge content was inferred

from both the MC-DLT and MCT spectra, recorded in $Si_{0.95}Ge_{0.05}$ alloy, as well as from C-V characteristics. This finding can be explained either by the fact that boron-doped $Si_{0.95}Ge_{0.05}$ diodes are more resistive to the appearance of the "acceptor removing" effect in comparison with boron-doped Si and $Si_{0.99}Ge_{0.01}$ diodes or due to Ge content modified density of the interstitial boron (B_i). The role of the boron–oxygen (B_iO_i) complex is significantly reduced in $Si_{0.95}Ge_{0.05}$ alloy due to local strain. This B_iO_i defect is responsible for the *B* acceptor removal and the degrading of radiation hardness. Therefore, transformations of the radiation-induced B_iO_i defect in $Si_{0.95}Ge_{0.05}$ diodes can pave an advanced technology in enhancement of the detector radiation hardness based on SiGe alloys with elevated Ge content. It was also shown that the values of activation energy of radiation-induced traps of minority carriers shift to the higher values with the increase in Ge content in *p*-type SiGe alloys. The generation currents in SiGe alloys, extracted from BELIV transients, indicate that radiation-induced minority carrier trap density is enhanced in p-type SiGe alloy diodes relative to that in p-Si diodes.

3.3. Comparison of electrical and optical characteristics in electron and proton irradiated SiGe materials

The radiation detectors under tests were fabricated at Scientific-Practical Materials Research Centre of NAS of Belarus in a configuration of n^+p diodes using SiGe substrates grown by Czochralski technique. The diodes contained the 2×3 mm^2 surface area and 500 μm thickness. Several $Si_{1-x}Ge_x$ single-crystal alloys with bandgap E_G varied according to x as [128] $E_G = 1.12 - 0.41x + 0.008x^2$ (eV) for $x < 0.85$ (at 300 K) were fabricated by incorporating either 1 or 5% of Ge. The diode basis was formed of p-type $Si_{1-x}Ge_x$ material which conductivity was controlled by concentration of boron dopants. The p-Si based diodes with the same doping were examined for comparison. Irradiations with 5.5 MeV electrons at room temperature were implemented by using a linear electron accelerator at Scientific-Practical Materials Research Centre of NAS of Belarus. Different exposures at fixed electron flux of 2×10^{12} cm^{-2}s^{-1} were applied to vary electron irradiation fluence. Irradiations with 1.6 MeV proton beam were performed by a Tandetron 4110A accelerator at Center for Physical Sciences and Technology, Lithuania, gradually increasing fluence. Proton beam current was varied in the range of 20–40 nA, and the largest fluence up to 10^{15} p/cm^2 was collected under the longest exposure. The pristine (A_p, B_p and C_p), electron (A_e, B_e and C_e) and proton (A_{P1}, B_{P1} and C_{P1}) irradiated Si and SiGe diodes

The diodes contained the 2 × 3 mm^2 surface area and 500 μm thickness. Several $Si_{1-x}Ge_x$ single-crystal alloys with bandgap E_G varied according to x as [128] $E_G = 1.12 - 0.41x + 0.008x^2$ (eV) for $x < 0.85$ (at 300 K) were fabricated by incorporating either 1 or 5% of Ge. The diode basis was formed of p-type $Si_{1-x}Ge_x$ material which conductivity was controlled by concentration of boron dopants. The p-Si based diodes with the same doping were examined for comparison. Irradiations with 5.5 MeV electrons at room temperature were implemented by using a linear electron accelerator at Scientific-Practical Materials Research Centre of NAS of Belarus. Different exposures at fixed electron flux of 2×10^{12} $cm^{-2}s^{-1}$ were applied to vary electron irradiation fluence. Irradiations with 1.6 MeV proton beam were performed by a Tandetron 4110A accelerator at Center for Physical Sciences and Technology, Lithuania, gradually increasing fluence. Proton beam current was varied in the range of 20–40 nA, and the largest fluence up to 10^{15} p/cm^2 was collected under the longest exposure. The pristine (A_p, B_p and C_p), electron (A_e, B_e and C_e) and proton (A_{P1}, B_{P1} and C_{P1}) irradiated Si and SiGe diodes, respectively listed in Table 3.5, were examined.

Table 3.5. The diodes under test, made on p-type Si and SiGe material substrates of the same doping.

Diode Base Material	Si		$Si_{0.99}Ge_{0.01}$		$Si_{0.95}Ge_{0.05}$	
Diode Batch	A		B		C	
Pristine Material	(A_P) Pristine		(B_P) Pristine		(C_P) Pristine	
5.5 MeV Electron Irradiation Fluences	(A_{e1}) 2×10^{14} e/cm^2	(A_{e2}) 4×10^{14} e/cm^2	(B_{e1}) 5×10^{13} e/cm^2	(B_{e2}) 2×10^{15} e/cm^2	(C_{e1}) 2×10^{14} e/cm^2	(C_{e2}) 5×10^{14} e/cm^2
1.6 MeV Proton Irradiation Fluences	(A_{P1}) 0–10^{15} p/cm^2		(B_{P1}) 0–10^{15} p/cm^2		(C_{P1}) 0–10^{15} p/cm^2	

The routine capacitance-voltage (C-V) characteristics were examined to control dopant concentration. These characteristics were measured at dc bias voltage (≤5 V) using a 1 MHz frequency harmonic test signal, before and after irradiation with definite fluence. The pulsed capacitance technique has been applied for junction barrier evaluation by linearly increasing voltage (BELIV) [97], and for estimation of carrier emission lifetime in the pristine and irradiated diodes.

The dopant concentrations (N_S) in the diode base region were evaluated using the measured C–V characteristics. These parameters in the pristine and irradiated samples are listed in Table 3.6. The experimental errors in

evaluation of dopant concentration N_S do not exceed 2% of the extracted values. It can be deduced from Table 3.6 that the effective dopant concentration in Si and $Si_{0.99}Ge_{0.01}$ material diodes decreases with enhancement of irradiation fluence. This can be explained by introduction of donor type radiation defects which compensate boron dopants.

However, the opposite tendency of doping level variation with irradiation fluence was revealed for the $Si_{0.95}Ge_{0.05}$ material diodes. This might be explained either through prevailing of the acceptor-like radiation defects in p-type $Si_{0.95}Ge_{0.05}$ material or via lattice bond length variations which affect the conduction and valence band parameters of the SiGe alloy [55] and the consequent shifts of Fermi level. The thermal activation energy shifts of radiation induced deep traps to low values with increase of Ge content in the SiGe alloy were inferred using DLTS characteristics obtained on the same diodes and published elsewhere. This result supports an assumption of lattice bond length variations with Ge content [119].

Table 3.6. The doping concentrations evaluated using C-V characteristics.

Sample			
Diode Base Material	**Fluence Φ (e/cm²)**	**N_S (cm⁻³)**	**N_S (cm⁻³) in Proton Irradiation Experiments**
Si	Pristine ($\Phi = 0$)	1.93×10^{14}	
	2×10^{14}	1.76×10^{14}	
	4×10^{14}	1.69×10^{14}	
$Si_{0.99}Ge_{0.01}$	pristine	1.82×10^{15}	6.61×10^{13}
	5×10^{13}	n/a	
	2×10^{15}	1.45×10^{15}	
$Si_{0.95}Ge_{0.05}$	pristine	1.81×10^{14}	2×10^{14}
	2×10^{14}	1.86×10^{14}	
	5×10^{14}	1.89×10^{14}	

The transients of the barrier capacitance pulsed charging (BELIV) might be useful in estimation of the thermal emission centers introduced by doping and irradiation procedures. The BELIV transients recorded on Si as well as $Si_{0.95}Ge_{0.05}$ diodes irradiated with 5.5 MeV electrons and rather moderate fluences are illustrated in Figure 4.11a. These transients are peak-current normalized to exclude an impact of diode area and absolute value of barrier height. The rather short LIV pulses (of $\tau_{PL} = 48$ μs) are there employed to have considerably large charging currents (due to elevated ramp $A = U_P/\tau_{PL}$ of LIV pulses of the invariable $U_P = 12$ V amplitude). The shape of transients in Figure 3.11a manifests only the impact of barrier capacitance charging where

an initial step AC_{b0} represents the displacement current ($i_C(t)$), delayed due to measurement circuit R_LC_{b0}, and a descending component governed by the subsequent charge extraction current. Therefore, the $i_C(t)$ can be estimated by using a convolution integral (Eq. 2.18). The impact of the thermal emission centers can be highlighted by additional illumination (Figure 3.11b) implemented using IR (1064 nm) laser. This additional illumination changes filling of the thermal emission centers. The laser generated excess carriers of density n_{ex} may change the effective density of band states as $N_{C,eff} \cong N_C - n_{ex}$, and, thereby, thermal emission time $\tau_g = \exp(E_{tr}/kT)/\nu_{th}\sigma N_{C,eff}$ (in Equation (3.3)). Here, E_{tr} is an activation energy of trap, kT is the thermal energy at temperature T, ν_{th} is thermal velocity of trapped carriers, σ is the carrier capture/emission cross-section. Thus, reduction of $N_{C,eff}$ leads to an increase of τ_g, which approaches to τ_{PL} and highlights the trapping/thermal emission centers. Additionally, the deeper an emission center (relative to the activation energy E_{tr}) the longer τ_g is.

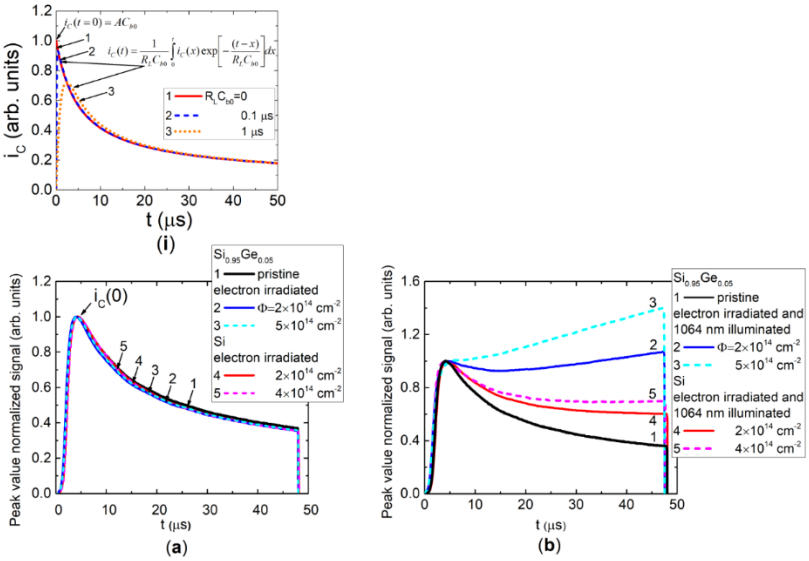

Figure 3.11. Evolution of BELIV transients in Si as well as $Si_{0.95}Ge_{0.05}$ diodes irradiated with 5.5 MeV electrons using various fluences and recorded in dark (**a**) as well as under 1064 nm wavelength laser illumination. (**b**) Here, LIV pulses of U_P = 12 V and τ_{PL} = 48 μs were employed. In the inset (**i**), the BELIV pulse components are denoted.

Figure 3.11b illustrates how the irradiation and additional illumination changes the BELIV transients of Si and $Si_{0.95}Ge_{0.05}$ diodes. The radiation

introduced emission centers increase the generation lifetime $\tau_g \sim 1/N_{C,eff}$, due to reduction of the $N_{C,eff}$ by the released carriers, as $N_{C,eff} \cong N_C - n_{ex}$. Also, the generation current increases, as the enhanced density m_{tr} of emission centers elevates the $i_g^* \sim e m_{tr} S w/\tau_{PL}$, when the i_g^* value exceeds that of i_C (see Equation (2.19)). Thereby, the enhancement of the electron irradiation fluence determines the increase of the thermal emission current in both Si and $Si_{0.95}Ge_{0.05}$ diodes (Figure 3.11b). However, density m_{tr} of the radiation induced emission centers seems to be dependent on the single crystal matrix. The proportionality of the i_g^* to m_{tr} is masked by the competition of i_g^* and i_C components within i_R (Equation (2.19)), and the observed values of i_g significantly depend of the range of τ_{PL}. Thereby, the qualitative estimation of thermal emission centers can reliably be elucidated using BELIV transients. Nevertheless, assuming $\tau_g \rightarrow \tau_{PL}$ for transients shown in Figure 3.11b, the m_{tr} introduced by electron beam into $Si_{0.95}Ge_{0.05}$ diodes is 1.8 times larger relative to that of Si material diode, at the same collected fluence of 2×10^{14} e/cm^2. On the other hand, it can testify that the prevailing thermal emission centers in $Si_{0.95}Ge_{0.05}$ diodes are shallower by 15 meV than those, radiation induced into Si diodes. The latter result is in line with DLTS results (obtained for the same Si and $Si_{0.95}Ge_{0.05}$ diodes) due to thermal activation energy shifts of radiation induced deep traps to low values with enhancement of Ge content within SiGe alloy.

The changes of carrier thermal generation lifetime can be directly observed in heavily irradiated diodes with significantly increased m_{tr} values when $\tau_g \rightarrow \tau_{PL}$ through elongated τ_{PL} and $i_g^* \rightarrow i_C$ due to reduction of the ramp A of long LIV pulses. Such a situation had been materialized in $Si_{0.99}Ge_{0.01}$ diodes irradiated with 2×10^{15} e/cm^2 5.5 MeV electrons, as illustrated in Figure 3.12. There, the BELIV transients in the pristine and irradiated diodes are compared. It can be clearly noticed, that the initial peak value in the BELIV transient is reduced for the irradiated diode due to the excess carrier capture. There, the decrease of ramp A for long LIV pulses should be coordinated with the τ_{PL} range to get $i_g \geq i_C$ and to directly highlight the i_g component. Direct separation of the i_g component enables estimation of the τ_g and E_{tr} values. Assuming the inherent values of $v_{th} = 10^7$ cm/s, $\sigma = 10^{-14}$ cm^2, and $N_C = 10^{19}$ cm^{-3} in Si and SiGe at room temperature, the $E_{tr} = 0.47$ eV was extracted using the transients of Figure 3.12. This would imply the traps with deep levels in the mid-bandgap.

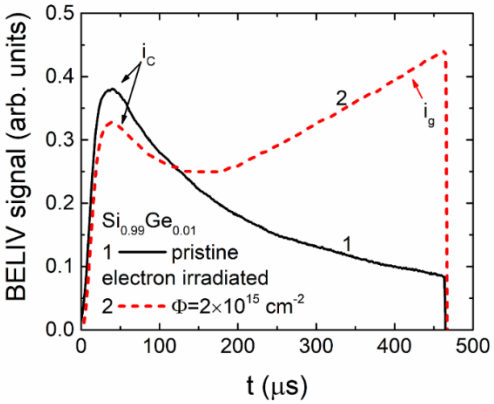

Figure 3.12. The BELIV transients recorded in pristine and electron irradiated $Si_{0.99}Ge_{0.01}$ diodes using LIV pulses of U_P = 12 V and τ_{PL} = 470 μs.

The recorded SS-PI spectra (Figure 3.13) really represent the step-like structure containing a single step, where spectral variation electron-photon interaction cross-section is well approximated by the Kopylov-Pikhtin model, represented by Equation (2.30). The spectral step peaked in the range of 1.1–1.3 eV, being above bandgap of E_G = 1.1 eV for the SiGe alloys, might appear due to the bandgap absorption modified by surface recombination. This assumption is supported by the changes of SS-PIS signal reduction in the range of >1.2 eV for both SiGe alloys. This SS-PIS signal decrease develops noticeably with Ge content (Figure 3.13). The simulated spectral steps, made using this Equation (2.30) and assuming values of the broadening factor in the range of Γ = 0.119–0.120, and shown in Figure 3.13 by dashed-curves. Superposition of the measured and simulated spectral steps implies that a single deep photo-active center with activation energy of E_{dl} = 0.97 eV prevails in all the electron irradiated samples irrespective of Ge content. Nevertheless, values of the photo-current (height of spectral steps) appear to be slightly dependent on irradiation fluence and Ge content within SiGe alloy. This effect can be explained by fluence dependent excess carrier concentration, generated by electron-photon interaction within SS-PIS process. The SS-PIS photo-current should be proportional to this carrier concentration (according to Equation (2.31)), which seems to be modulated by carrier capture and recombination processes. Thereby, a SS-PIS step obtained in SiGe diodes irradiated with 2×10^{14} e/cm^2 fluence appears to be the higher one relative to that irradiated with 2×10^{15} e/cm^2 fluence (Figure 3.13). Differences of relative heights of the SS-PIS steps obtained in the electron irradiated Si and SiGe alloys can be explained by activation energy shifts of radiation induced deep traps with enhancement of Ge content within

SiGe alloy. Assuming a simplified approach, where these single-type deep centers are involved in both carrier photo-activation (SS-PIS, Figure 3.13) and thermal emission (within BELIV transients, Figures 3.11b and 3.12), a configuration diagram might be sketched (see the inset *i* for Figure 3.13).

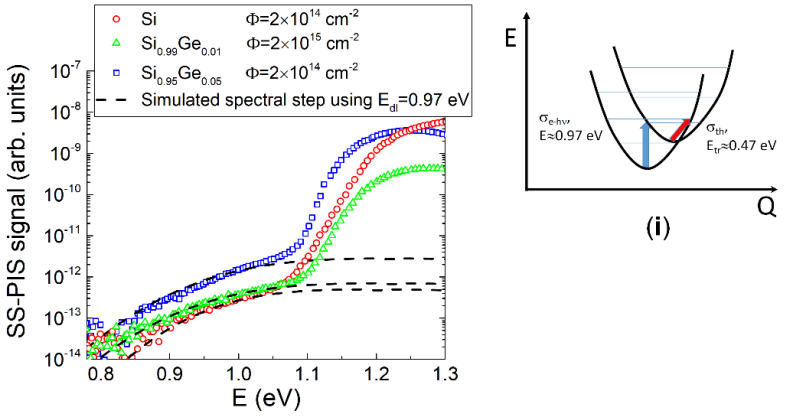

Figure 3.13. SS-PIS spectra recorded in the electron irradiated Si and SiGe diodes. In the inset (**i**), the configuration diagram sketched using SS-PI spectra and BELIV estimations, made using Figures 3.11 and 3.12.

Modulation of the concentration of the photo-excited excess carriers by carrier capture and recombination processes was examined using analysis of the photo-conductivity transients. Carrier lifetime in pristine and electron irradiated samples was extracted after irradiations using microwave-probed photoconductivity (MW-PC) transients (Figure 3.14a). The deep traps act as the recombination defects. However, the shallow levels act as the trapping (generation current) centers [20], which temporary capture the excess carriers followed by further thermal trapped carrier release into free states. The carrier recombination lifetime (τ_R) was measured within the initial MW-PC decay stage at e^{-1} level relative to a peak value of the transient (Figure 3.14a). Some transients (in samples irradiated with large fluence) contained the second (asymptotic decay) component, which is related to the trapping lifetime (τ_{tr}), Equation (2.23). Values of both carrier lifetimes (τ_R and τ_{tr}) as a function of electron irradiation fluence are represented in Figure 3.14b.

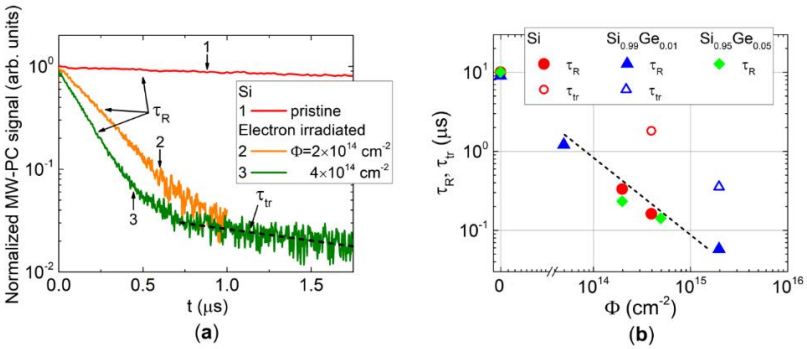

Figure 3.14. (**a**) Carrier decay transients recorded by MW-PC technique in Si diodes irradiated with 5.5 MeV electrons collecting different fluence. (**b**) Carrier lifetimes ascribed to their decay through recombination and trapping centers as a function of electron irradiation fluence in pristine and irradiated Si and SiGe samples (A, B and C, Table 3.5).

It can be noticed in Figure 3.14b that trapping lifetimes (τ_{tr}) are nearly an order of magnitude longer than the recombination lifetimes. Also, the trapping effect can be resolved reliably only in heavily irradiated diodes when radiation defect concentrations are sufficiently large. Both carrier recombination and trapping lifetimes decrease near-reciprocally relative to density of the radiation defects acting as carrier capture and thermal emission centers. Variation of values of the carrier recombination lifetimes in the electron irradiated Si and SiGe diodes obeys the same line (eye-guided by dot curve in Figure 3.14b) in a double-log $\tau_R - \Phi$ scale. This hints on nearly the same mechanisms of radiation damage of the examined Si and SiGe materials.

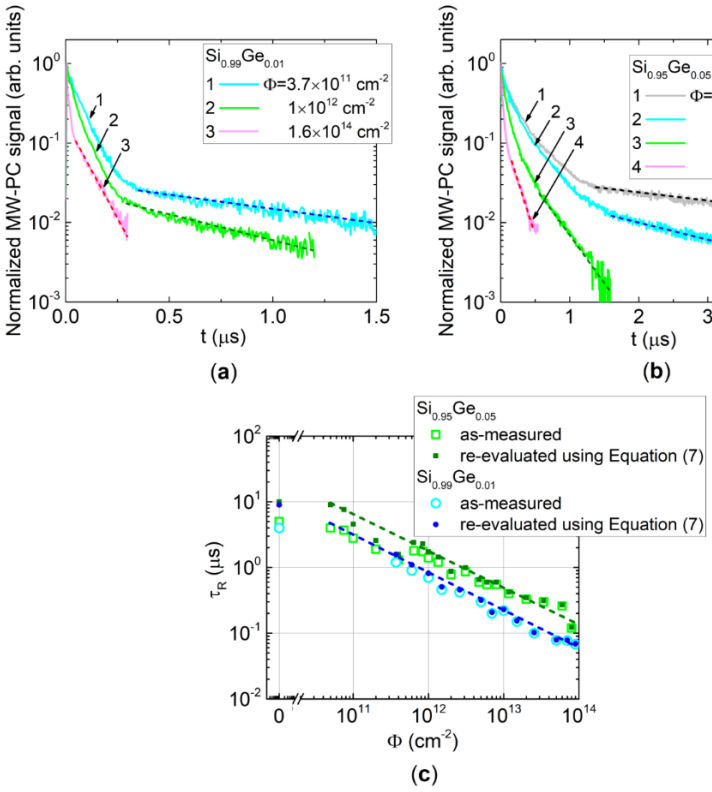

Figure 3.15. The MW-PC relaxation transients recorded on $Si_{0.99}Ge_{0.01}$ (**a**) and $Si_{0.95}Ge_{0.05}$ (**b**) diodes irradiated with 1.6 MeV protons of varied fluence. (**c**) Carrier recombination lifetime as a function of 1.6 MeV proton fluence in $Si_{0.99}Ge_{0.01}$ and $Si_{0.95}Ge_{0.05}$ samples. Here, the MW-PC transients (shown in Figures 3.15a,b) were in situ scanned during proton irradiation within stopping range of 1.6 MeV protons.

The more complicated situation (relatively to that of penetrative electrons, illustrated in Figure 3.14) appears in recording and analysis of the MW-PC transients after and during irradiation with stopped particles, namely 1.6 MeV protons. There, the sample depth dependent carrier decay lifetime is inherent. As mentioned, the near-surface excitation regime has been applied, and carrier decay transients recorded within stopping range of 1.6 MeV protons were examined *in-situ* during proton irradiations, to overcome profiling of carrier lifetime. The recorded transients appear also (like in the case of carrier trapping) to be similar to the two-componential decay (Figures 3.15a,b). However, the initial decay fragment of the transient should be ascribed to the transitional processes of surface recombination [21], due to inhomogeneous excitation by strongly absorbed light. The asymptotic decay

is then governed by the surface (τ_s) and bulk recombination (τ_R) lifetimes. The latter parameter is really modified by radiation defects, and transients (illustrated in Figures 3.15a,b) significantly vary depending on the collected proton irradiation fluence. The surface (τ_s) recombination lifetime has been additionally estimated by dedicated investigations using a technique of several excitation wavelengths [21]. Then, values of the carrier bulk recombination lifetime (Figure 3.15c), attributed to proton introduced radiation defects, were corrected using these τ_s and the as–measured $\tau_R - \Phi$ characteristics, by applying Equation (2.21). It can be inferred from Figure 3.15c that corrections of the τ_R values are important only in the range of small fluences where τ_s is close to those of τ_R values. The corrected $\tau_R - \Phi$ characteristics, obtained for diodes made of SiGe alloy with different Ge content, appear to be the near-reciprocally dependent on density of the radiation defects, assumed being proportional to the proton irradiation fluence Φ. As can be deduced from Figure 3.15c, the carrier recombination lifetime, governed by radiation defects, is obtained to be longer for the SiGe alloy with the larger Ge content (of 5%) than that of 1% Ge. This result implies that the SiGe alloys (with enhanced Ge content) can be prospective materials in fabrication of radiation tolerant particle (especially hadron) detectors. However, a trade-off for Ge content enhancement within SiGe material and growth of the single-crystal SiGe alloys should be found.

In summary of this section, the radiation hardness of SiGe alloys relative to penetrative (5.5 MeV electrons) and strongly absorbed (1.6 MeV protons) high energy particles has been estimated by control of carrier emission and capture centers characterized by carrier recombination as well as thermal emission lifetime variations dependent on irradiation fluence. These characteristics have been recorded in diodes made of SiGe alloys with different Ge content and compared with those obtained for Si of the same p-type conductivity and doping level. It has been demonstrated that qualitative estimation of thermal emission centers can be implemented using BELIV transients related to barrier capacitance of the diodes. Nevertheless, the density of trapping centers introduced by electron beam into $Si_{0.95}Ge_{0.05}$ diodes might be 1.8 times larger relative to the Si material diode, at the same collected fluence. On the other hand, it can testify that the prevailing thermal emission centers in $Si_{0.95}Ge_{0.05}$ diodes are shallower by 15 meV than those, radiation induced into Si diodes. The latter result is in line with DLTS results obtained for the same Si and $Si_{0.95}Ge_{0.05}$ diodes due to thermal activation energy shifts of radiation induced deep traps to low values with enhancement of Ge content within SiGe alloy. It has been demonstrated that separation of the generation

current components within BELIV transients (when possible) enables estimation of the thermal emission lifetime and, consequently, thermal activation energy E_{tr}. The activation energy of E_{tr} = 0.47 eV was extracted from BELIV transients for the prevailing species of the radiation defects. The close values of activation energy in the range of 0.5–0.58 eV had been revealed by the dedicated investigations of DLTS spectra in the irradiated Si and SiGe diodes. The radiation defects with such the activation energy were assigned to the radiation induced complexes of interstitials with carbon or boron impurities. Thereby, the revealed prevailing emission centers in our work are in line with DLTS data published in literature. The prevailing photo-generation centers with photo-activation energy of 0.97 eV have been also revealed using the steady-state photo-ionization spectroscopy. Assuming a simplified approach, where the single-type deep centers are involved in both carrier photo-ionization and thermal emission, a configuration diagram for the carrier capture-release processes has been sketched. It has been revealed that both carrier recombination and trapping lifetimes decrease near-reciprocally relative to density of radiation defects acting as carrier capture and thermal emission centers. It has been found that variation of the recombination lifetimes in the irradiated Si and SiGe diodes obeys the same type curve in the double-log $\tau_R - \Phi$ scale. This hints on nearly the same mechanisms of radiation damage of the examined Si and SiGe materials. A technique of measurements, implemented by locating the fiber and needle-tip MW probes within 1.6 MeV proton stopping range, has been applied to examine fluence dependent lifetime characteristics under irradiations by strongly absorbed particles. It has been revealed that the carrier recombination lifetime, governed by radiation defects introduced using the strongly absorbed proton irradiation, is longer for the SiGe alloy containing the larger Ge content (of 5%). This might be explained through prevailing of the acceptor-like radiation defects in p-type SiGe alloy material containing the enhanced content of Ge. Also, it has been shown the predominance of point radiation defects. Activity of point defects can be modified by anneal procedures and, thereby, recovery of irradiated sensors can be performed. The SiGe alloys might also be promising in engineering of the strong field layer of the advanced low gain avalanche detectors [1].

3.4. Irradiated ammonothermal GaN materials

Study of the radiation damage in GaN-based materials becomes an important aspect for possible application of the GaN detectors in the harsh radiation environment at the Large Hadron Collider, at medical particle accelerators and

other medical instruments Intentionally doped and semi-insulating bulk ammonothermal GaN materials, suitable for fabrication of bulk sensors, were studied to reveal the dominant defects introduced by reactor neutron irradiations. Variations of the response of the capacitor-type sensors with neutron irradiation fluence have been correlated with the carrier lifetime changes. The measurements of the photoconductivity and photoluminescence transients have been used to study the variation of the parameters of radiative and non-radiative recombination, important in production of fast scintillators acting as beacons to indicate the nuclide arrival into brachytherapy zone. The examined characteristics showed that AT GaN is a sensitive particle detection material being radiation hard up to high hadron fluences $\geq 10^{16}$ cm^{-2}.

These intrinsic point and extended defects determine a rich spectrum of deep levels by modifying electrical conductivity. To suppress the enhanced un-intentional doping, fast recombination centres are commonly introduced by using the transitional metal impurities (such as Fe), to have a semi-insulating GaN material. This additionally leads to the considerably short carrier lifetime and fast sensor response. The increasing of the detector thickness, for instance, by applying CVD or HVPE grown GaN, however, becomes an improper mean for enhancing of an interaction path in particle detectors with extremely short carrier lifetime. Introduction of the radiation defects during operation of particle sensors in harsh areas of particle accelerators considerably depends on pristine material, exploited for detector fabrication [141-144]. Integral sensor damage by irradiations varies with thickness of sensors depending on particle type and energy, due to different interaction cross-sections, and on penetration paths for incident radiations. To reduce radiation damage of detectors, thin sensor structures with internal amplification [90] can be promising for particle tracking. Thus, the high quality MOCVD GaN might be suitable for fabrication of such type sensors. In order to produce rather thick sensors for recording of the penetrative particles with small interaction cross-section, the ammonothermally grown GaN with significantly reduced ($<10^4$ cm^{-2}) dislocation densities is the most promising material. Therefore, knowledge of the intrinsic and irradiation fluence dependent variations of the optical and electrical characteristics is important.

The ammonothermal (AT) GaN is the most promising material for particle detector fabrication due to significantly reduced densities of the intrinsic defects (e.g. dislocation densities) relative to other technology GaN (HVPE, MOCVD) materials (cf. $<10^4$ cm^{-2} in AT GaN, $\geq 10^6$ cm^{-2} HVPE GaN and $\geq 10^9$ cm^{-2} in MOCVD GaN). Moreover, rather thick and homogeneous AT GaN single-crystals can be grown and applied in production of sensors for

detection of penetrative, high-energy particles. The AT GaN materials doped with different impurities (Mn, Mg) were studied in order to estimate possibilities in fabrication of either fast or extremely sensitive particle detectors. The Mn impurities in GaN (GaN:Mn) may act as fast carrier traps and compensating centres for unintentionally introduced donor-type defects, inherent for GaN materials. Such a GaN:Mn is suitable for formation of the semi-insulating (SI) material. The SI GaN:Mn can thereby be appropriate for production of fast and rather sensitive detectors, - as short carrier lifetime determines fast recovery of the sensor, while the depletion layer in SI GaN:Mn junction structure will be thick and easily governed by small concentrations of radiation generated secondary pairs of the excess carriers. The Mg impurities serve as the main dopants in formation of the p-type conductivity GaN. Thus, AT GaN:Mg material, especially with long carrier lifetimes, is the most suitable for production of thick junction-structure (for instance, pin diode) particle detectors. Thick sensors are inevitable in detection of high energy particles, where interaction cross-section is rather small, and long particle path within sensor is necessary for generation of secondary carrier pairs of recordable amount. The parameter of the carrier pair generation per detector length unit (~90 pairs/μm is inherent for GaN materials) determines the required detector thickness to reach the recordable collected charge. The registered high energy irradiation inevitably introduces radiation defects by particle energy loss due to ionizing processes and through the non-ionizing energy loss (NIEL). The parameter of defect introduction rate serves as another characteristic of the detector radiation hardness. Alternatively, a characteristic of carrier recombination/trapping lifetime as a function of irradiation fluence can be employed for estimation of material tolerance to heavy irradiations. In GaN materials, excess carrier annihilation appears due to radiative and non-radiative channels. Therefore, comprehensive characterization of the irradiated material should be applied to predict operational features of the designed particle sensors, especially for future, very high luminosity LHC experiments (e.g. CMS detectors, installed within harsh area of the CMS forward calorimeter, should sustain 10^{17} cm^{-2} fluences). The elevated doping densities of sensor materials can thereby be preferential to increase radiation tolerance of sensors by enhancing the ratio of dopant density relative to radiation defect concentration. The trade-off should often be found to harmonize the parameters of sensor thickness, speed, sensitivity, radiation hardness, etc. The irradiations of high energy particles (1 -10 MeV) lead to prevailing of NIEL processes in radiation damage of detectors [2, 9]. The NIEL material damage by different type particle (neutrons, protons, pions, electrons) becomes then similar. Therefore, the 1 MeV neutron

equivalent relative to NIEL damage is widely used [62] for estimation of the effective fluence within sensor characteristics such as charge collection efficiency, carrier trapping lifetime, defect introduction rate. Complementarily, reactor neutron irradiations are rather suitable for emulation of the evolution of the particle detector functionality during LHC experiments, as homogeneous damage can there be easily reached.

In this work, the results of the comprehensive study of electrical and optical characteristics, inherent for the pristine and radiation affected ammonothermal (AT) GaN, are reported. The carrier recombination features in the AT GaN materials were examined by combining measurements of fluence dependent variations of carrier lifetime, time integrated and time resolved photoluminescence spectroscopy. The characteristics of the non-radiative recombination and trapping of carriers were investigated by the microwave-probed photoconductivity (MW-PC). The time integrated and time resolved photoluminescence (PL) as well as steady-state photoluminescence measurements were employed to study the dynamics of different density carriers involved within radiative recombination processes before and after irradiations of GaN samples. The charge collection efficiency (CCE) characteristics were examined by inspection of current transients recorded on sensor structures. The CCE has been estimated from the reduction of the collected charge in sensors irradiated with different fluences. Clear correlation among MW-PC, PL and CCE characteristics dependent on neutron irradiation fluence has been obtained. It has been proved that AT GaN material is the most suitable for fabrication of rather thick particle detectors.

The high crystalline quality bulk ammonothermal GaN (AT GaN) samples were fabricated at *AMMONO* company (Poland) [91]. These samples were made as 400-450 μm thick wafers of the GaN doped with Mg and Mn. Ammonothermal GaN crystals grown on HVPE-GaN seeds contain dislocation density of about 7×10^4 cm^{-2} [92] or less than ~10^3 cm^{-2} by using the small-size seeds ("point seed"). The ammonothermal GaN samples were irradiated by nuclear reactor neutrons using wide range of fluences (10^{12}-5×10^{16} cm^{-2}) at Jožef Stefan Insitute (Ljubljana) TRIGA reactor. The TRIGA reactor emits neutrons of a continuum spectrum where fast neutrons (> 100 keV) with energy peaked at 1 MeV are generated with flux of 7.5×10^{12} n/(cm^2 s). A fluence is evaluated by using the equivalent of the 1 MeV neutron irradiation NIEL damage.

Examination of material and detector structures were examined by techniques briefly described in Chapter 2. Measurements of the parameters of carrier radiative and non-radiative recombination at different excess carrier densities were performed by steady state (SS), time integrated (TI) and time

resolved (TR) photoluminescence (PL) and microwave-probed photoconductivity transients (MW-PC) [21], respectively. Complementarily, carrier capture and transport parameters have been examined by transient current technique (TCT) [90]. This TC technique was implemented using the capacitor-like (metal-semiconductor-metal structure) sensors made of GaN materials under research. There, carrier drift transients are recorded by measuring variations in time of sensor current under optical injection of the excess carriers into the inter-electrode gap of a sensor by a laser beam. The device under test (DUT) is connected in series with a voltage source and a charging current limiting resistor. The transient signal of TCT is transferred to the oscilloscope input through a capacitor and load resistor loop. The current transients are recorded by a digital 1 GHz oscilloscope of Tektronix TDS-5104. A DUT was mounted on a strip-line printed-circuit-board (PCB) to have proper time resolution. The same TCT injection conditions, like in MW-PC experiments, were kept using 400 ps laser pulses at 354 nm wavelength.

Carrier decay transients in pristine AT GaN:Mg samples, registered by MW-PC technique, are illustrated in Fig. 3.16a. These transients are clearly two-componential, with a short initial decay constituent followed by the considerably longer component, which is close to exponential one. The relative amplitude of the latter asymptotic component depends on excitation intensity, and it increases with excess carrier concentration, being proportional to an excitation density. The observed variations of MW-PC transients in the pristine AT GaN:Mn samples are similar to those obtained for AT GaN:Mg non-irradiated material. While the time scale (up to ten of μs) for transients registered in AT GaN:Mg is significantly longer than those (up to tens of ns) for AT GaN:Mn. The same two-componential character of carrier decays implies the simultaneous action of several mechanisms in carrier extinction. A fixed time-scale for the excess carrier density decrease to a background level hints on the small impact of the disorder effects. These effects are manifested as the extended-exponent shape relaxation in GaN materials, containing high dislocation densities. This assumption is in agreement with rather low dislocations densities $\leq 10^4$ cm^{-2} in the AT GaN materials investigated. The increase of the amplitude of an asymptotic decay component with excitation intensity excludes manifestation of a simple carrier trapping effect [21], where the role of trapping should appear at reduced excess carrier concentrations. Dependence of decay components on fixed wavelength (354 nm, under –prevailing band-to-band processes) excitation intensity also excludes the impact of surface recombination (with nearly the same

asymptotic decay time), even at assumption of the intensity dependent surface recombination velocity. Thus, an assumption of the non-linear decay process with simultaneous action of the radiative (as UV photoluminescence) and non-radiative recombination through deep levels becomes the most realistic. Such a process of the excess carrier variation in time ($n_{ex}(t)$) is described by Eq. (2.22).

The MW-PC signal is then proportional to the concentration of free carriers. Thereby, the parameter $n_{ex,0}$ is directly estimated using a transient taken from experiment at a fixed excitation density. The excitation density is evaluated using the laser beam parameters and material absorption coefficient at fixed wavelength. The tentative value of carrier lifetime (τ_R) ascribed to each transient can also be estimated from the slope of the asymptotic (close to an exponential: $n_{ex,0}\exp(-t/\tau_R)/[1+B\tau_R n_{ex,0}]$) component within a recorded transient. Thus, value of either B or a pair (B, τ_R) is the only adjustable parameter involved into simulation of the experimental transients. It is worth mentioning that even the simple two-exponential relaxation approach includes more than three adjustable parameters to reach fitting of the recorded transients by the simulated ones. The as–recorded and simulated transients for different excitation intensities are compared in Fig. 3.16a. The most important parameter in these correlations is τ_R which is a measure for estimation of the non-radiative recombination defects. The B coefficient of an estimated value of $(1 - 3)\times10^{-8}$ cm^3/s should be attributed to the UV (band-to-band) recombination process. Thus, further analysis of the impact of the neutron irradiations has been performed using the approach (Eq. 2.22) for the parameter evaluations using the best fit between the experimental and simulated MW-PC transients.

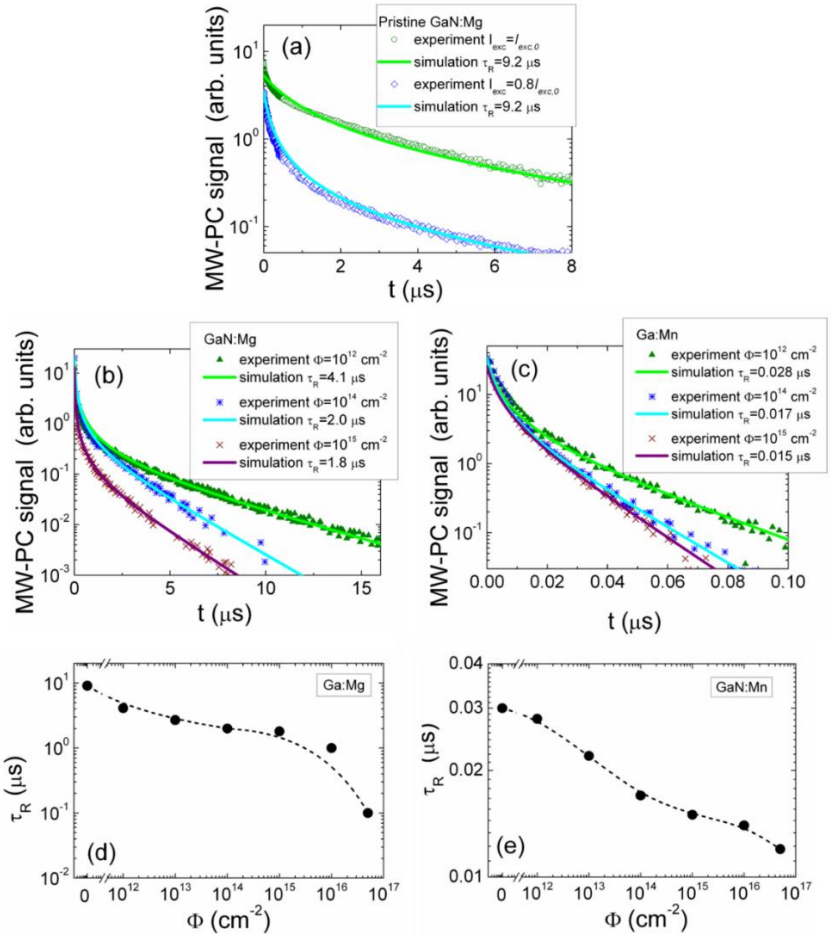

Fig. 3.16. a- The as-measured MW-PC transients (symbols) and simulated (solid curves) carrier decay transients using (Eq. 1) approach for the pristine AT GaN:Mg material varying excitation intensity. Neutron fluence dependent MW-PC transients (symbols) for the AT GaN:Mg (b) and GaN:Mn (c) samples fitted by simulated ones (solid curves). Variation of values of the non-radiative recombination lifetimes extracted form fits in Figs. (b, c) as a function of neutron fluence, obtained for GaN:Mg (d) and GaN:Mn (e) samples.

Variations of the as-recorded and simulated MW-PC transients with neutron irradiation fluence are illustrated in Figs. 3.16b and 3.16c for GaN:Mg and GaN:Mn materials, respectively. It can be clearly deduced, that variations of these MW-PC transients are caused by τ_R reduction with enhancement of

neutron irradiation fluence Φ. The extracted values of τ_R for GaN:Mg and GaN:Mn materials as a function of Φ are depicted in Figs.3.16d and 3.16e, respectively.

For the high quality ammonothermal GaN material, the rather long carrier lifetime values have been obtained, relative to other MOCVD and HVPE GaN samples, supplied by different vendors [91,92]. The considerably longer lifetimes obtained for pristine GaN:Mg, relative to those in GaN:Mn, indicate that Mn impurities act as fast recombination centres. Values ($\tau_R \leq 30$ ns) of carrier recombination lifetime in AT Mn-doped GaN are close to those (2-20 ns)\ measured in semi-insulating HVPE grown and iron doped material (GaN:Fe). Mn and Fe impurities are implied to be the compensating impurities for the un-intentionally introduced technological defects in GaN materials. Mg impurities seem to be the dopants responsible for conductivity type formation and can act as the free carrier supply (generation) centres.

The high quality ammonothermal GaN is rather tolerant to neutron irradiations, relative to other MOCVD and HVPE GaN samples, supplied by different vendors, irradiated by hadrons and examined by MW-PC technique [21]. Carrier recombination lifetime decreases by factor of 100 in GaN:Mg under neutron irradiation with the largest fluences 5×10^{16} n/cm^2 applied (Fig. 3.16d). While in GaN:Mn material, reduction of carrier recombination lifetime was obtained by factor of 3 over wide range (10^{12} –5×10^{16} n/cm^2) of neutron fluences (Fig. 3.16e). This indicates that radiation defects are the most efficient in GaN:Mg material, where relatively long carrier lifetime is inherent. Carrier lifetime is one of the most important parameter of particle sensors, which determines the efficiency of charge collection (CCE) and a possibility to detect electrical signals on the background of electrical noises.

The charge collection efficiency has been evaluated by measuring pulsed current responses of the capacitor-like sensor structures made of irradiated AT GaN samples, at applied voltage of 280 V. There, excitation density was fixed to the lowest values, acceptable for the transient current (TCT) registering in sensors made of the most irradiated material. The CCE has been evaluated by current integration in time over a TCT pulse. To calibrate the CCE variations dependent on irradiation fluence, the time integrated TCT signals for the irradiated material sensors were normalized to that of the pristine material, separately for GaN:Mg and GaN:Mn.

Values of the normalized CCE as a function of neutron fluence are depicted in Figs. 3.17. At low fluences ($\Phi \leq 10^{14}$ n/cm^2), this CCE is almost constant and equal to the CCE of a sensor made of the non-irradiated material. For moderate fluences ($\Phi \geq 10^{15}$ n/cm^2), the radiation defects, induced by

neutrons, lead to the decrease of CCE. At the highest irradiation fluences (Φ=5×10^{16} n/cm^2), the CCE decreases to ~2.1 % and to ~7.5 % in Mn doped samples. In Mg doped and Φ=5×10^{16} n/cm^2 irradiated AT GaN samples, CCE decreases to ~1.8 %. The decrease of CCE is related to the density of recombination/trapping active defects. To estimate fluence dependent variations of CCE due to changes of carrier transport parameters, the fluence dependent characteristic CCE/τ_R was therefore analysed. A reduction of this CCE/τ_R parameter appeared to be faster in Mg doped AT GaN material relative to that in Mn doped samples. In agreement with this $CCE/\tau_R - \Phi$ characteristic for GaN:Mg, the PL intensity decreases with enhancement of irradiation fluence faster than that in Mn irradiated AT GaN samples, indicating the elevated introduction rate of the non-radiative defects in Mg doped GaN. These observations imply that density of the electrically active centres, induced by neutron irradiation, also depends on the type and concentration of dopants. The rather small variation of values of the CCE/τ_R parameter for a wide (Φ=10^{12} - 10^{15} n/cm^2) range of fluences hints on the relatively high radiation hardness of AT GaN material.

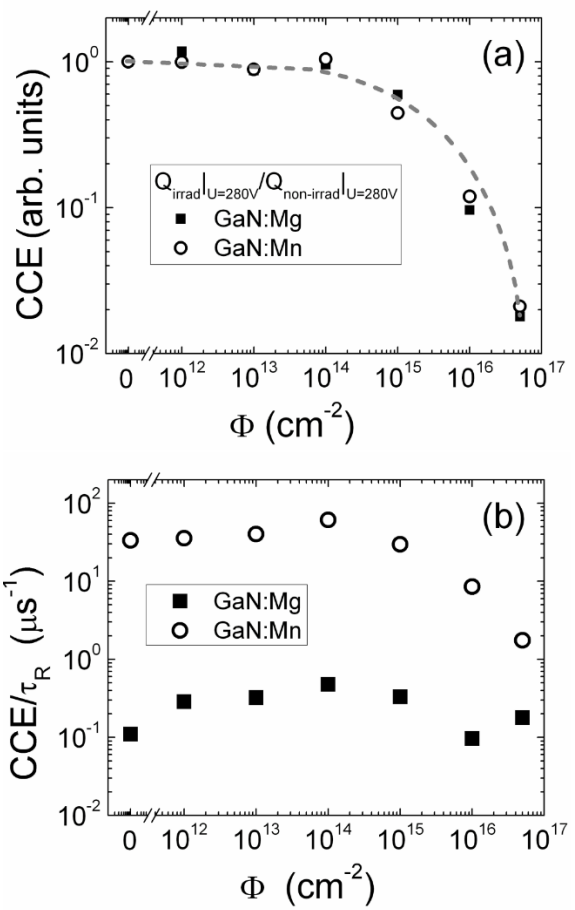

Fig. 3.17. The CCE normalized to a CCE value obtained for the non-irradiated sample (a) and the ratio of CCE and recombination lifetime (CCE/ τ_R) (b) as a function of neutrons irradiation fluence for Mg (squares) and Mn (open dots) doped AT GaN samples.

The fluence dependent reduction of the excess carrier lifetime has been obtained for both AT GaN:Mg and GaN:Mn materials. This characteristic is in good agreement with neutron fluence determined changes of the PL intensity, Fig. 3.18.

The decrease of the carrier lifetime is the main reason for charge collection efficiency degradation in heavily irradiated particle sensors made of AT GaN. As it has been demonstrated, the TCT signals can be registered by AT GaN sensors irradiated with the largest neutron fluences of 5×10^{16} n/cm^2, at least, by pulsed laser carrier injection. Nevertheless, the PL signals remain at the detectable intensity level. Thereby, AT GaN material is suitable for fabrication of the double-response particle sensors with properly low

leakage currents. The exceptionally long carrier lifetimes (up to several μs) in AT GaN:Mg make this material applicable in formation of thick detectors.

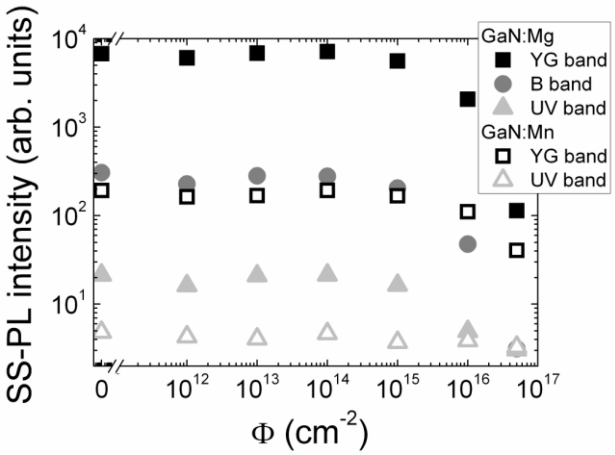

Fig. 3.18. Fluence dependent variations of the peak intensity for the YG-PL, B-PL, UV-PL bands in GaN:Mg and GaN:Mn samples as a function of neutron irradiation fluence.

The steady-state photoluminescence (SS-PL) spectroscopy represents the radiative recombination processes for stabilized filling of radiative and non-radiative recombination centres. The dynamics of the excess carrier redistribution among PL channels might be different for the high and low excitation levels. Variations of the SS-PL spectra recorded on GaN:Mg (a) and GaN:Mn (b) materials, irradiated with different neutron fluences, are illustrated in Fig. 3.18. It can be deduced from comparison of spectra for GaN:Mg (a) and GaN:Mn (b) in Fig. 3.18 that UV-PL intensity considerably decreases with enhancement of neutron fluence (Φ) for GaN:Mg, while this UV-PL intensity is nearly independent of Φ for GaN:Mn. In both GaN:Mg and GaN:Mn samples, the YG-PL is the dominant peak within SS-PL spectra. The broad YG-PL band is commonly attributed to deep level defects with strong electron-phonon coupling [12]. The red luminescence (R-PL) peaked at 1.9 eV appears as a shoulder to the YG-PL band. The R-PL is usually related to the $Mn^{3+/2+}$ dopants, those act as the acceptor centres forming a level located at 1.8 eV above the valence band. Recent studies, performed on the un-intentionally doped ammonothermal GaN materials with a n-conductivity type, also showed the Mn concentration dependent degradation of the luminescence. For B-PL, YG-PL and R-PL bands (Fig. 3.18), the PL intensity

decreases with enhancement of irradiation fluence in GaN:Mg samples faster than in GaN:Mn, indicating the higher introduction rate of radiation defects (for the GaN:Mg), acting as the non-radiative recombination centres. Fluence dependent variations of the peak intensity of YG-PL, B-PL and UV-PL bands for GaN:Mg and GaN:Mn as a function of neutron fluence are depicted in Fig .12c. There PL peak intensities are almost independent of moderate irradiation fluence, of $\Phi \leq 10^{15}$ n/cm^2 values, demonstrating the rather high radiation hardness of AT GaN materials in their applications for particle sensors with optical response.

3.5. Comparison of the simulated and recorded characteristics of LGAD detectors made of Si and SiGe alloys

Silicon–germanium ($Si_{1-x}Ge_x$) material-based devices with enhanced radiation tolerance are capable to operate for applications in future Large Hadron Collider (LHC) [1]. The radiation induced deep carrier traps affect the characteristics of the semiconductor particle detector.

Comparison of the electrical characteristics for simulated Low Gain Avalanche Detectors (LGAD) has been performed of both p-type Si and $Si_{1-x}Ge_x$ with different Ge content (with x in the range of 1% to 5.1%) materials. The diode structures (Fig. 3.19) were designed identically the same by dimensions, dopant concentrations and origin of traps (the parameters of traps in Si and $Si_{1-x}Ge_x$ were borrowed from literature data) to compare the characteristics of SiGe and Si LGADs.

The simulations (Figure 3.20) of I-V characteristics revealed the lower values of dark current in $Si_{1-x}Ge_x$ LGAD structure containing 10% Ge compared with pure Si LGAD structure. However, the higher concentrations of Ge in the SiGe LGAD structures caused the higher dark current values compared with the pure silicon LGAD. LGAD structures containing traps exhibit the higher dark current values in I-V characteristics for both Si and SiGe trap-less structures. This could be caused by carrier trapping effect due to deep emission centres.

The experimentally recorded I-V and C-V characteristics in various LGAD devices are illustrated in Figure 3.21. The obtained I-V and C-V characteristics qualitatively fit rather well the simulated ones.

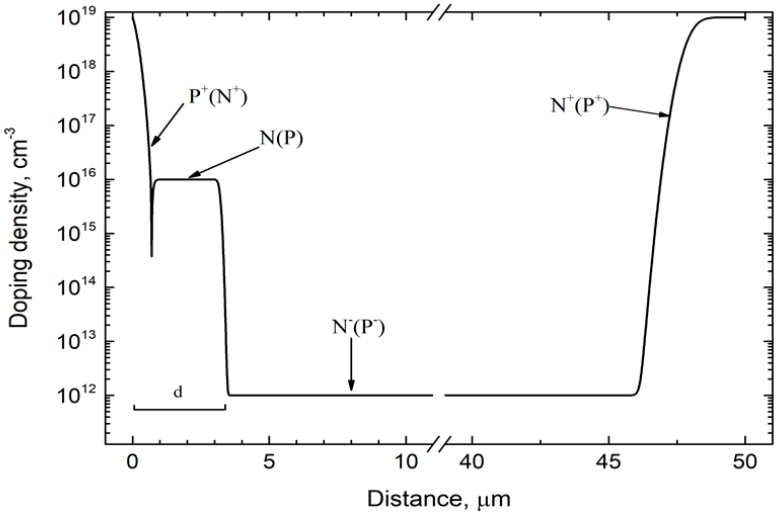

Fig. 3.19. The TCAD accepted doping profile for the LGAD structure with a phosphorus doped n-well epitaxial layer.

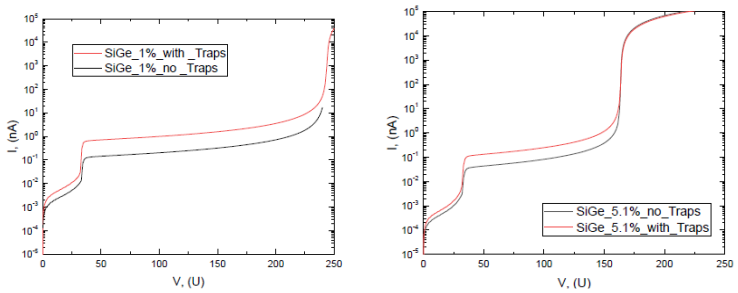

Fig. 3.20. Comparison of the simulated I-V characteristics for LGADs made of p-type $Si_{1-x}Ge_x$ with different Ge content (with x=0.01(a) and x=0.05(b)) in trap free and trap containing materials.

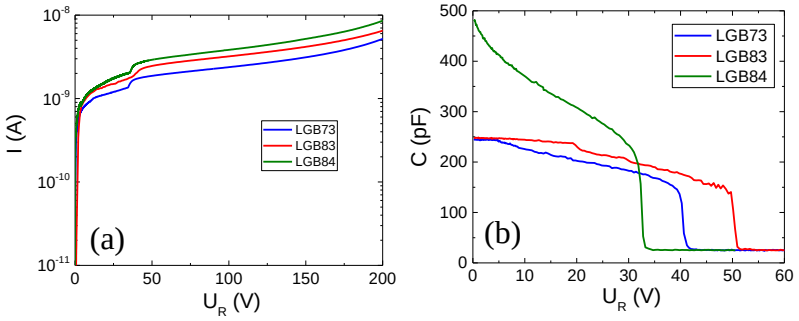

Fig. 3.21. The I-V (a) and C-V (b) characteristics measured on three different runs in fabrication of the LGAD sensors using the same technology.

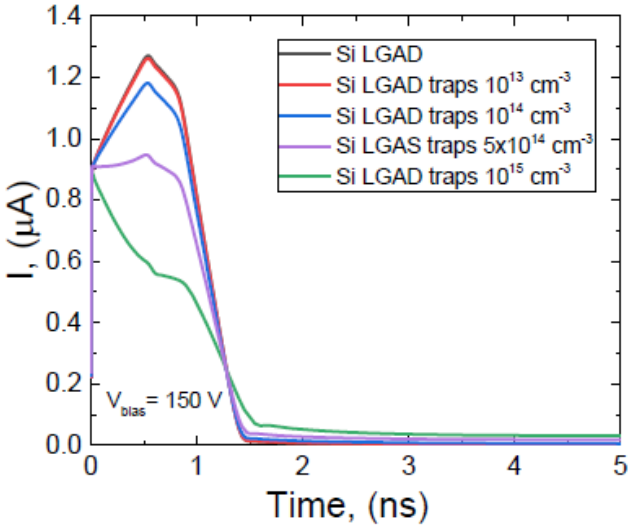

Fig. 3.22. Simulated TCT current pulses of Si LGAD's dependent on concentration of traps.

The simulations (Figure 3.22) revealed the lower values of dark current in $Si_{1-x}Ge_x$ LGAD structure containing 1% Ge content compared to that of pure Si LGAD structure. The TCT current transients of Si LGAD's showed the elongation of the carrier extraction pulses (Figure 3.22) with enhancement of the trap concentration. This could be explained by the carrier trapping effect due to deep emission centres.

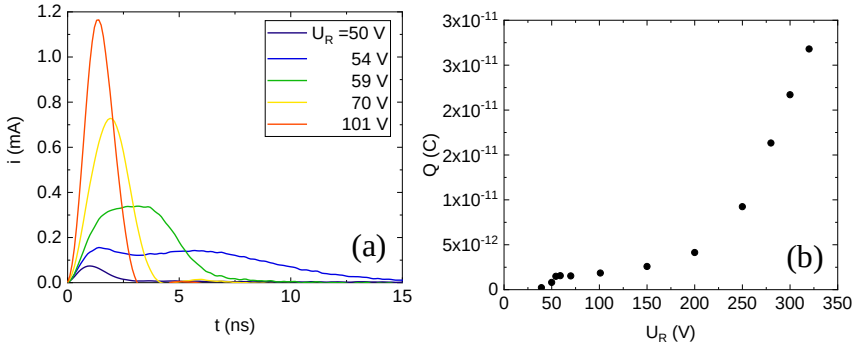

Fig. 3.23. The experimentally determined evolution of the TCT transients generated by the LGAD sensors obtained varying applied reverse voltage (a)

and (b) the collected charge dependence on applied external voltage when the charge is injected by λ=532 nm laser pulses.

The TCT current shows the inherent increase with enhancement of applied voltage (Figure 3.23 a), while drift time of the injected excess carrier domain shortens with this voltage evolution. The collected charge is an integral of current over time (Figure 3.23 b). Due to small injected charge, the changes of the transient shape (Figure 3.23a) become observable only for elevated (> 50 V) values of applied voltage. The sharp step in values of the collected charge (Figure 3.23b) appears for applied voltages above 200 V. This is in line with initiation of avalanche process for the tested LGAD structures. It has been evaluated (by comparing the collected charge values for 150 V and 330 V of external reverse voltage) the gain coefficient to be about 30 owing to an avalanche process. This can be ascribed to the low gain region of the sensors with the internal enhanced field layer.

For comparison, the evolution of the TCT transients have been experimentally measured (Figure 3.24) for pin sensors, also varying applied reverse voltage (a), and the collected charge dependence on applied external voltage (b) was examined when the charge is injected by λ=532 nm laser pulses.

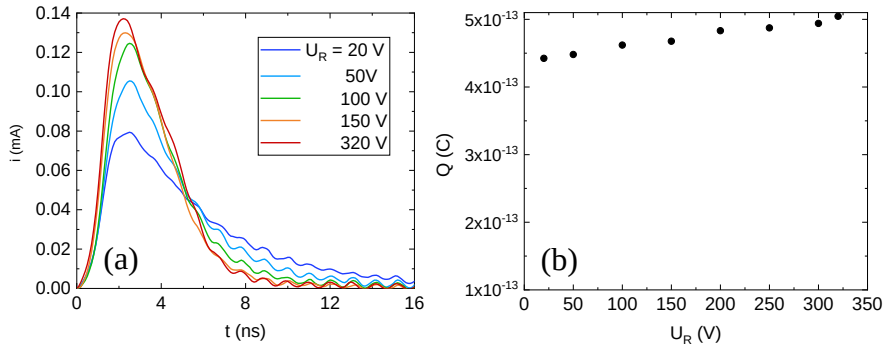

Fig. 3.24. Evolution of the TCT transients measured on pin sensors varying applied reverse voltage (a), and (b) the collected charge dependence on applied external voltage when the charge is injected by λ=532 nm laser pulses.

The transients obtained for pin diodes (Figure 3.24 a) are two-componential. These transients represent the evolution of excess carrier drift regime from the bipolar process (where electron and hole domains move in opposite directions) to the monopolar one, when the slower carriers determine

the displacement current component at the end of the drift process. The carriers have been injected within edge of the diode structure in the latter experiments. The injection of carriers is implemented here nearby the junction location. The collected charge (Figure 3.24b) increases close to linearly with enhancement of applied voltage. Therefore, no amplification effect appears using pin diodes.

4. DEVELOPED TECHNOLOGY OF THE BRACHYTHERAPY PLANNING

The brachytherapy planning [EPO-1] and treatment procedures comprise inevitable and specific component of the identification and reconstruction of the radiation emitters within catheters and applicators used in dynamic treatment [145], when actual position of radiation source should be firstly reconstructed in the phantom and then in patient's body. Brachytherapy planning can be implemented using 2D representations and documentations for simplified applications or using 3D imaging techniques such as computer tomography (CT), magnetic resonance (MR) and ultra-sound scanning (US).

4.1. Problems of radiation dosimetry in brachytherapy planning

Reconstruction of the radiation emitters within catheters needs the time-resolved control of the radioactive source position [146]. The time-resolved dosimetry is more sensitive in administration of treatment deviations [147]. Moreover, the instantaneous dose rate measurements and accumulated dose maps are necessary for planning and implementation of brachytherapy procedures. The precise localization of emitters and dosimeters in high-dose-gradient fields is crucial for adequate evaluations of measurement uncertainty. As usually, the different apparatuses are employed for identification and control of the mutual positions of a patient and radiation emitters. Qualitatively, the methods for control and imaging of the continuous localization of medical probes and patient anatomy can be classified as 1) optical tracking, based on video-cameras and visual markers [147], 2) the electromagnetic (EM) tracking, based on detection of magnetic fields due to the induced currents in solenoids or fluxgate sensors [148, 149], 3) the X-ray based flat-panel imagers or computer tomography (CT) based 3D imaging systems, 4) the combined positioning systems composed of dosimeter sensors acting as position and dose detectors [147, 150].

The optical tracking is mainly employed in surgery procedures when visual scenes can be labelled and directly controlled. However, special techniques, such as Brachy-View [147], based on pinhole γ-camera, where a linear array of pinholes in collimator is combined with an array of pixelated Si detectors, can be implemented for real time tracking of radiation emitters by analysing multiple images projected onto the detector array. The emitter location is there evaluated by finding the space point with minimum perpendicular distance to all the back-projected lines through the

corresponding pinholes. However, modelling of the pinhole geometry and Monte-Carlo simulations should be performed to reach the adequate sensitivity and spatial resolution without radiation overexposing healthy organs. The catheters and needle-type probes are tracked inside the human body, and the electromagnetic (EM) tracking means have emerged as the method for localization of small EM sensors in a given EM field [149]. The EM tracking phenomenon arises from the fact that electromagnets are responsible for producing changing (ac) or quasi-static (dc) magnetic fields, which induce currents in solenoid sensors embedded in the detectors. The phenomenon responsible for the operation of these tracking systems relies solely on magnetic induction. EM tracking accuracy can be compromised by magnetic field distortion due to nearby medical diagnostic devices or ferromagnetic objects. Furthermore, additional hardware components of the tracking system, such as the EM field generator, which must be placed close to the patient and imaging devices equipped with fragile EM sensor. The X-ray imaging systems are appropriate for when large volumes of the patient's body are tracked as in external radiation treatment using electron or γ-ray beams. However, usage of X-ray for patient's positioning can be detrimental, especially in brachytherapy when rather small ranges should be imaged and controlled, while rather intensive irradiations are delivered to patient for the auxiliary positioning purposes. The more intricate emitter tracking systems, based on the so-called Magic Phantom [147], can be designed where it is possible to measure the delivered irradiation dose with simultaneous source position and timing accuracy by using the high timing resolution of the analogue front-end electronics.

Examples of positioning and dosimetry methods and instruments for control of the brachytherapy emitters in brachytherapy planning and treatment procedures are described in research papers [145-150].

From patents and patent applications, the documents closest to the present invention are:

1) A method and apparatus based on "A phantom for verification of accuracy of HDR brachytherapy planning and Phantom device having the phantom", described in Korean Patent Reg. No. KR 100613244 discloses a high-dose-rate brachytherapy phantom for quality control of a treatment planning computer that establishes a treatment plan for brachytherapy, the phantom for brachytherapy of the registered patent is composed of an acrylic assembly composed of a rectangular parallelepiped holder, to which an applicator is fixed, and an upper, lower block, and side block to which the holder is inserted and fixed, and various dose measurements and distribution measurements are possible by simulating the human body. However, the high-

dose-rate brachytherapy phantom of the above registered patent has a complex structure and can only be applied to a specific type of dose measuring device as suggested in the registered patent, and the existing dose measuring devices are not applicable.

2) Another method and apparatus based on 'Phantom device for measuring proximity radiation dose (Phantom apparatus for measuring dose of brachytherapy radiation)', described in Korean patent Reg. No. KR 101752972 discloses a phantom device for measuring proximity radiation dose capable of improving treatment precision through accurate prediction of radiation dose irradiated to a patient during treatment. A phantom device for measuring proximity radiation dose (to achieve the above object) includes a base plate provided with 1) a plurality of installation grooves in which 2) a plurality of dosimeters are installed, and 3) a cover for covering the base plate with a plurality of cover grooves covering the plurality of dosimeters and a 4) photosensitive plate stacked on the base plate with the cover plate interposed there between and in which 5) a radiation photoreceptor is embedded. The dosimeter includes at least one of a glass dosimeter, a MOSFET (Metal Oxide Field Effect Transistor) dosimeter, an OSLD (Optically Stimulated Luminescence Dosimeter) dosimeter, and a Thermo-Luminescence Dosimeter (TLD) dosimeter. The base plate, the cover plate and the photosensitive plate are formed of a synthetic resin material including acrylic. The photosensitive plate is provided with grid-shaped coordinates for measuring radiation dose distribution. A fluorescent material is provided in a plurality of positions on at least one of the base plate, the cover plate, and the photosensitive plate. The base plate, the cover plate, and the photosensitive plate are fixed to each other by a plurality of fixing clips that are coupled in a stacked state.

3) The closest prototype patent would be AU 2008100728 A4 which discloses 'A real time treatment dose verification system for afterloader brachytherapy systems'. The patented system will measure the brachytherapy treatment radiation dose and the geometrical distribution of the radiation dose during the treatment delivery by a brachytherapy afterloading system. The system can measure the position of radiation isotope source as it moves through each catheter, in real time over the duration of the entire treatment. It can compare the amount of radiation dose being delivered as well as the geometric distribution of the dose against the planned treatment dose and distribution. The system consists of a two-dimensional flat panel imaging device that is positioned against the patient during the treatment. The flat panel imager is then linked to a control computer system that reads the data from the imager and compares the radiation measured to the planed patient treatment. The flat panel imager records the patient exit radiation dose at a known

geometrical plane from the brachytherapy implant, as a digital image. The flat panel imager is responsive to the radiation X-ray energies of the radioactive isotope. (For example, a common radiation isotope source is Iridium-192, which has a mean X-ray energy of 390 kV. The imager will also be responsive at x-ray energies of 120 to 140 kV). The geometrical location of the flat panel imager in relation to the patient is determined using an external kilovoltage X-ray system. The flat panel imager is positioned for treatment, then a kilovoltage image is taken through the patient, to record the flat panel imager and patient relationship. This image is fed to the process computer before brachytherapy treatment commences and the geometrical position is calculated. As the treatment delivery proceeds, with the after loader stepping the radioactive isotope source trough each catheter, the image recorded by the flat panel imager is transferred to the control computer system where the measured image is subtracted from a planned image. All measured and planed image comparisons will be made progressively as treatment is delivered at some predetermined time interval. An error threshold will be set, producing an error flag when the delivered dose differs by more than a critical amount from the planned dose. This error flag will notify the brachytherapy treatment operator to stop the treatment. The data collected over the duration of the treatment will also provide a total delivered radiation dose record. The dose recorded by the flat panel imager is patient exit dose. The process computer, as well as comparing planned and delivered exit dose, will also back project the exit dose through the patient, to the implant site, and provide measured radiation dose at any plane within the cancer site. The back projection method therefore provides a two dimension in-vivo dose verification system without any invasive procedure. This process can be applied to any part of the human body.

The main drawback of the above reviewed methods and apparatuses is that they need additional instrumentation for positioning of the emitters with additional X-ray sources, those can be detrimental for patient, they need several base and florescent plates with a lot of dosimetry grooves where a solution of the optimization task is very complicated and needs long exposures, to simultaneously estimate position and accumulated dose.

4.2. Structure of the tentative instrumentation for radionuclide positioning

The present apparatus and self-consistent method for brachytherapy planning is based on triangulation of needle type probes fixed within a base plate (10, 24) containing a mesh-work (25) linked to a plurality of phantom installation

grooves in which three needle-type catheters comprise a 3D synchronous scanner made of a system of internal scintillator sensors (3) operating as beacons installed within, at least, three needle-type scaling catheters (6) those are positioned within either therapeutic patient‘s organ (1), which contour is simultaneously imaged by either routine CT or US means (14), or phantom for brachytherapy procedure planning; the coordinates of the 3D scanner (3-9) are tightly linked to a base plate (10, 24) containing a mesh-work (25) linked to a plurality of phantom installation grooves in which three needle-type catheters (6) containing optical beacons are initially installed, and the base plate has a grid-shaped coordinate scale indicator (10, 24) linked to a plurality of cover grooves and a label on the patient‘s body (10, 24); operation of the 3D scanner (3-9) implemented using scintillating sensors (3) is based on scintillator signals, induced by the same brachytherapy emitter, those are transferred by fiberscopes (7) to optical/electrical signal digital converters (8) and further transmission (9) to the control computer inputs; the scintillator signals can also be used for additional positioning of the CT (14) X-ray source and binding of these CT X-ray source coordinates to the base plate (24) position and scale (26), to link the 3D scanner coordinates to the cancer site and its contour; the 3D scanner is combined with dosimeters (17), made of semiconductor radiation sensors, installed within the scaling needle-type catheters (6) together with scintillating beacons; triangulation (28)) of the signals of radiation sensors is combined with scaling performed using 3D scintillation scanner (3-9) to reach the enhanced precision in radiation source positioning in time-space resolved coordinates.

The present apparatus and self-consistent method for brachytherapy is devoted for time resolved positioning of radiation emitters and dosimetry in planning and in vivo brachytherapy based on triangulation of needle type probes fixed within time-space resolved coordinates comprising a 3D scanner.

A brachytherapy synchronous positioning and dosimetry apparatus (2, Fig. 4.1) and a self-consistent method for brachytherapy planning and treatment procedures on patient’s (0, Fig.4.1) cancer site (1, Fig. 4.1), consists of 3D synchronous scanner made of a system of internal scintillator sensors (3) operating as beacons installed within, at least, three needle-type scaling catheters (6, Fig. 4.1) those are positioned within either therapeutic patient‘s organ (1), which contour is simultaneously imaged by either routine CT or US means (14, Fig. 4.1), or phantom for brachytherapy procedure planning; the coordinates of the 3D scanner (3-9, Fig. 4.1) are tightly linked to a base plate (10, Fig. 4.1) containing a mesh-work linked to a plurality of phantom installation grooves in which three needle-type catheters (6) containing optical beacons are initially installed, and the base plate has a grid-shaped coordinate

scale indicator linked to a plurality of cover grooves and a label on the patient‘s body (10, 24); operation of the 3D scanner (3-9) implemented using scintillating sensors (3) is based on scintillator signal transfer by fiberscopes (7) to optical/electrical signal digital converters (8) and further transmission (9) lines.

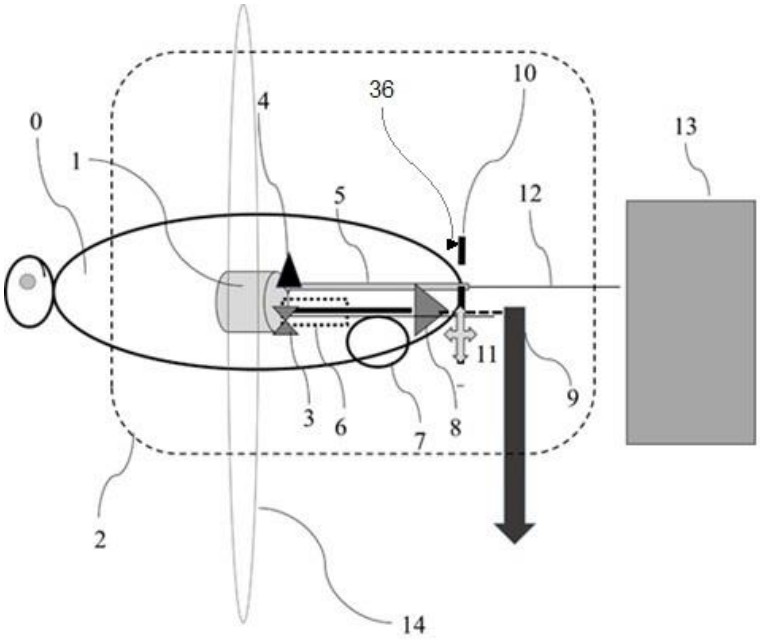

Fig. 4.1. A brachytherapy synchronous positioning and dosimetry apparatus (2) for implementation of the brachytherapy planning and treatment procedures on patient’s (0) cancer site (1), consists of 3D synchronous scanner made of a system of internal scintillator sensors (3) operating as beacons installed within, at least, three needle-type scaling catheters (6) those are positioned within either therapeutic patient‘s organ (1), which contour is simultaneously imaged by either routine CT or US means (14), or phantom for brachytherapy procedure planning; the coordinates of the 3D scanner (3-9) are tightly linked to a base plate (10, 24) containing a mesh-work (25) linked to a plurality of phantom installation grooves in which three needle-type catheters (6) containing optical beacons are initially installed, and the base plate has a grid-shaped coordinate scale indicator (10, 24) linked to a plurality of cover grooves and a label on the patient‘s body (10, 24); operation of the 3D-scanner (3-9) implemented using scintillating sensors (3) is based on scintillator signal transfer by fiberscopes (7) to optical/electrical signal digital converters (8) and further transmission (9) to the control computer inputs; the scintillator signals are also used for additional positioning of the

CT (14) X-ray source and binding of these CT X-ray source coordinates to the base plate position and scale to link the 3D-scanner coordinates to the cancer site and its contour; the 3D- scanner is combined with dosimeters, made of semiconductor radiation sensors, installed within the scaling needle-type catheters (6) together with scintillating beacons; triangulation of the signals of radiation sensors is combined with scaling performed using 3D-scintillation scanner (3-9) to reach the enhanced precision in radiation source positioning in time-space resolved coordinates.

The signals from the transmission lines are addressed to the control computer inputs; the scintillator signals are also used for additional positioning of the CT (14) X-ray source and binding of these CT X-ray source coordinates to the base plate (24, Fig. 4.4) position and scale (26 Fig. 4.4), to link the 3D scanner coordinates to the cancer site and its contour; the 3D scanner is combined with dosimeters (17 Fig. 4.2), made of semiconductor radiation sensors, installed within the scaling needle-type catheters (6) together with scintillating beacons; triangulation (28 Fig. 4.5)) of the signals of radiation sensors is combined with scaling performed using 3D scintillation scanner (3-9, Fig. 4.1) to reach the enhanced precision in radiation source positioning in time-space resolved coordinates.

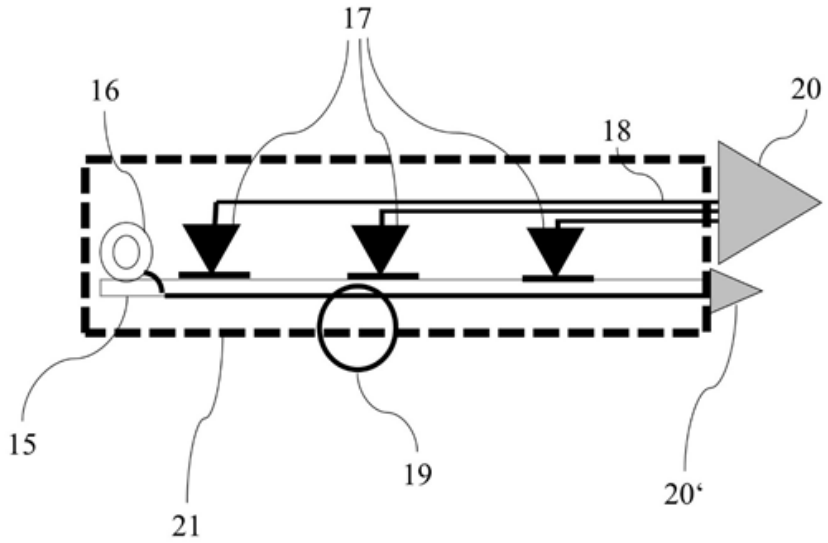

Fig. 4.2. Single probe (21) of the 3D scanner made of insulating ribbon substrate (15), installed within the needle-type catheter (6), and on which the scintillating positioner (16) together with several dosimeter sensors (17) are

mounted, and to which the electrical wires for (18) and optical fibers (19) for transfer of the sensor signals to the digital transducers (20, 20') are attached.

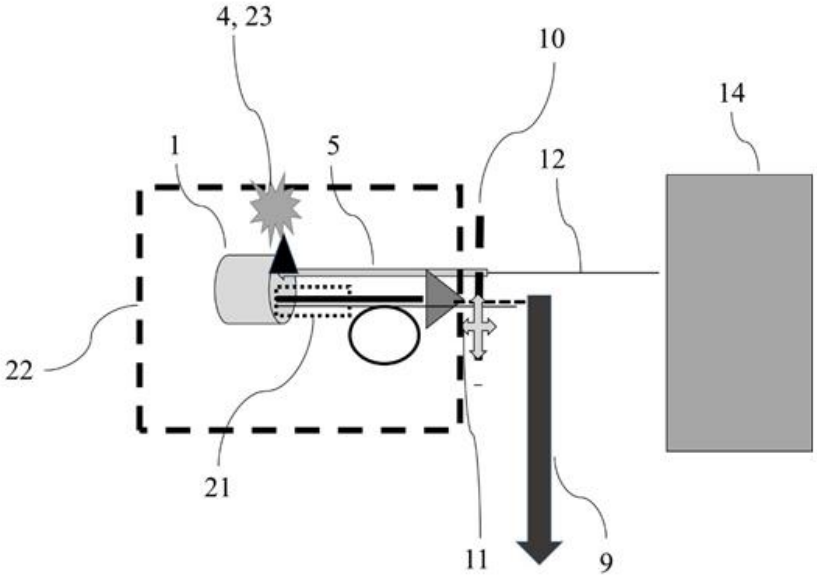

Fig. 4.3. The brachytherapy synchronous positioning and dosimetry apparatus, based on 3D scanner (21) and composed for implementation of the brachytherapy planning using a phantom (22) where scintillator signal, for position labelling, is excited by either radioisotope emitter from brachytherapy afterloader (14) or CT X-rays (23).

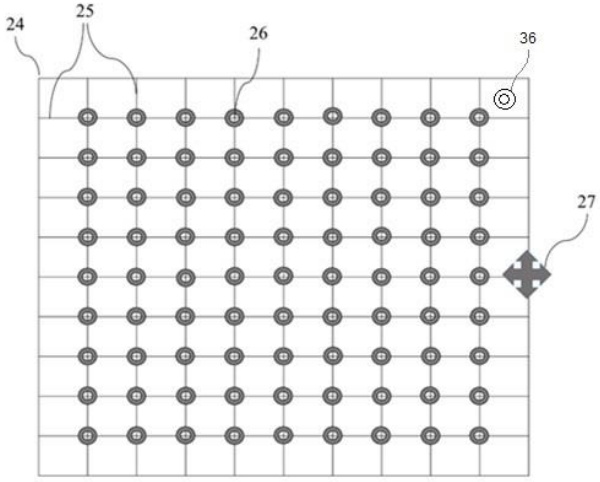

Fig. 4.4. The brachytherapy phantom for the brachytherapy planning includes a base plate (24) provided with a plurality of installation holes (26) and

containing a mesh-work with (X-Y) 2D coordinate labels (25) which is linked to a plurality of phantom installation grooves as the needle-type inserts for radioisotope and 3D scanner. The base plate also contains labels for identification of the base plate with patient‘s body, phantom cube and probes of the 3D scanner.

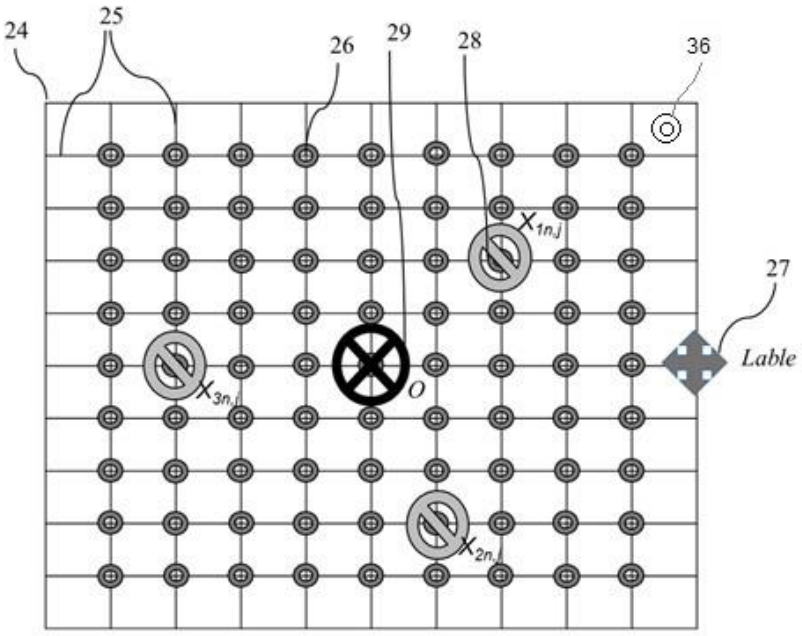

Fig. 4.5. Initial positioning of the 3D-scanner (28) relative to the catheter *C* (29), containing a radionuclide emitter, using a coordinate system, bound to the base plate (24), which is performed either during installation of the brachytherapy phantom (within brachytherapy planning procedures or starting of the brachytherapy treatment. The coordinate scale of the base plate is precisely bound to the patient’s body using a remote position verification devices (RPVD), such as LiDAR (laser imaging, detection, and ranging), ultrasound or laser distance meters, installed within base plate (as illustrated by the 36 element in Picture 5), which can be additionally bound to a label (27) on patient’s body. Such an arrangement of RPVD and base plate bind is employed for independent control of the base plate position (and consequently of the 3D scanner position) relative to irradiation target (tumour contour) within patient’s body. The coordinate binding and control procedures additionally ensure the instantaneous measurements of a distance from the

patient's body under test in order to precisely determine the appeared position deviations inevitable for the advanced dose calculations.

The present brachytherapy positioning and dosimetry apparatus has such preferences relatively to "A real time treatment dose verification system for afterloader brachytherapy systems":

- the present apparatus contains scintillator sensors operating as temporal and position beacons installed within needle-type scaling and dosimetry catheters instead of complicated external positioning systems, described in scientific literature and mentioned patents, based on either additional electromagnetic tracking based on detection of magnetic fields or the X-ray based flat-panel imagers or computer tomography (CT) based 3D imaging systems, or the combined positioning and dosimetry extended matrix systems;
- 3D synchronous position–dosimetry scanner employed in the present apparatus, made of a rigid system of three internal scintillator and dosimeter sensor catheters, provides a fast and optimal triangulation system for the tight binding of the scanner to the scaling-calibration base plate with a grid-shaped coordinate scale indicator and patient's body label;
- for the brachytherapy planning and verification the 3D phantom is bound to the scaling-calibration base plate with a grid-shaped coordinate scale indicator and patient's body label containing a plurality of 3D phantom installation grooves, in which a triangle of needle-type catheters making a 3D position-dosimetry scanner, are initially installed for the initial calibration of the positioning system where an initial calibration procedure is performed using the central catheter filled with the same radioactive-isotope emitter, as employed for treatment procedures and provided from the afterloader by the special applicator;
- the brachytherapy verification procedures can be performed without of either ultrasound or CT imaging instrumentation when using a calibrated and bound to patient's label 3D phantom with the separately obtained cancer site contour, related to the irradiation planning phantom;
- the scintillation beacon or scintillator within double-response sensor can be employed for control of radiation damage of the dosimeters inside dosimetry scanner.

The present brachytherapy positioning and dosimetry method has such preferences relatively to "A real time treatment dose verification system for after loader brachytherapy systems":

- the positioning method is self-consistent with instrumentation for the treatment irradiation procedures and avoids additional X-ray source, which may be detrimental for a patient;
- the method is based on superposition of the patient's body label with the scaling-calibration base plate, containing a grid-shaped coordinate scale indicator and the 3D phantom coordinates, and coincidence procedure is initially performed by using the central catheter filled with the radioactive-isotope emitter;
- the simultaneous positioning and dosimetry method is based triangulation procedure using a rigid triangle of the initially calibrated 3D synchronous scanner and solving the optimization task using the stripe of 3 dosimeters for rapid calculations in optimization solutions, instead of triangulation by optimization procedures made among multiple dosimeters within prototype patent, where clear optimization is hardly achieved;
- the time-resolved, dynamic positioning procedures can be implemented by measuring transients of the analogue signals generated by the fast double-response scintillation-photoconductivity detectors, where position/distance equivalent delays are controlled.

4.3. Principles of the positioning of the radioactive emitters and dosimetry mapping

Principles of the positioning of the radioactive emitters and dosimetry mapping in verification of the brachytherapy planning and treatment procedures.

The 3D synchronous position–dosimetry scanner is assembled to make a rigid triangulation system of three internal scintillator and dosimeter sensor catheters, bound to a scaling-calibration base plate with a grid-shaped coordinate scale indicator, positioned on the 3-D phantom. The position on strip array of each scintillator sensor in every dosimetry catheter of the position-dose scanner, acting as a temporal and position beacon, is determined and bound to the coordinate scale of the base plate. The coordinate scale of the base plate is precisely bound to the patient's body using a remote position verification devices (RPVD), such as LiDAR (laser imaging, detection, and ranging), ultrasound or laser distance meters, installed within base plate (as illustrated by the 36 element in Figure 5), which can be additionally bound to a label on patient's body. Such an arrangement of RPVD and base plate bind is employed for independent control of the base plate position (and consequently of the 3D scanner position) relative to irradiation target (tumor)

within patient's body. This also ensures the tight correlation between coordinate scale of the base plate and dosimeters. The 3D synchronous position–dosimetry scanner is composed, installed and related to the base plate coordinate system. The central irradiation catheter is installed, the radioactive emitter is shortly inserted into this catheter from the after loader through fixed applicator, the signals of scintillation and dosimetry sensors are registered by making the initial map (matrix) of temporal orientation-position-dose rate data. On the base plate, either patient or phantom labels are superimposed. The data of cancer site contour bound with phantom cube coordinates are loaded to memory of the central computer when separate cancer site imaging is performed by using ultrasound or X-ray CT instruments. The signals of scintillating beacons and dosimeters of the 3D scanner are additionally registered and superimposed with base plate and phantom coordinates, using X-ray excitation sources within CT instrument when cancer site contouring is synchronously performed (by CT) with initial calibration of the present brachytherapy positioning and dosimetry apparatus. The fixed set of data such as S_K (the Kerma factor evaluated in air), Λ (the dose rate constant), $G(r, \Theta)$ (the geometrical-factor function of the employed radionuclide), $g(r)$ (the radial dose function), and $F(r, \Theta)$ (the anisotropy correction factor related to the angular dependent characteristic of the specific emitter activity) is initially provided for evaluating of the dose rate $\partial D(r,\Theta)/\partial t$, emitted by the definite radionuclide,- according to supplier information. Also, the calibrated characteristics (such as illustrated in Figures 7-9) of the amplitudes of each sensor response as a function of the distance r^{**} between the radionuclide and the sensor (mounted within catheter cylinder) are measured and tabulated in advance.

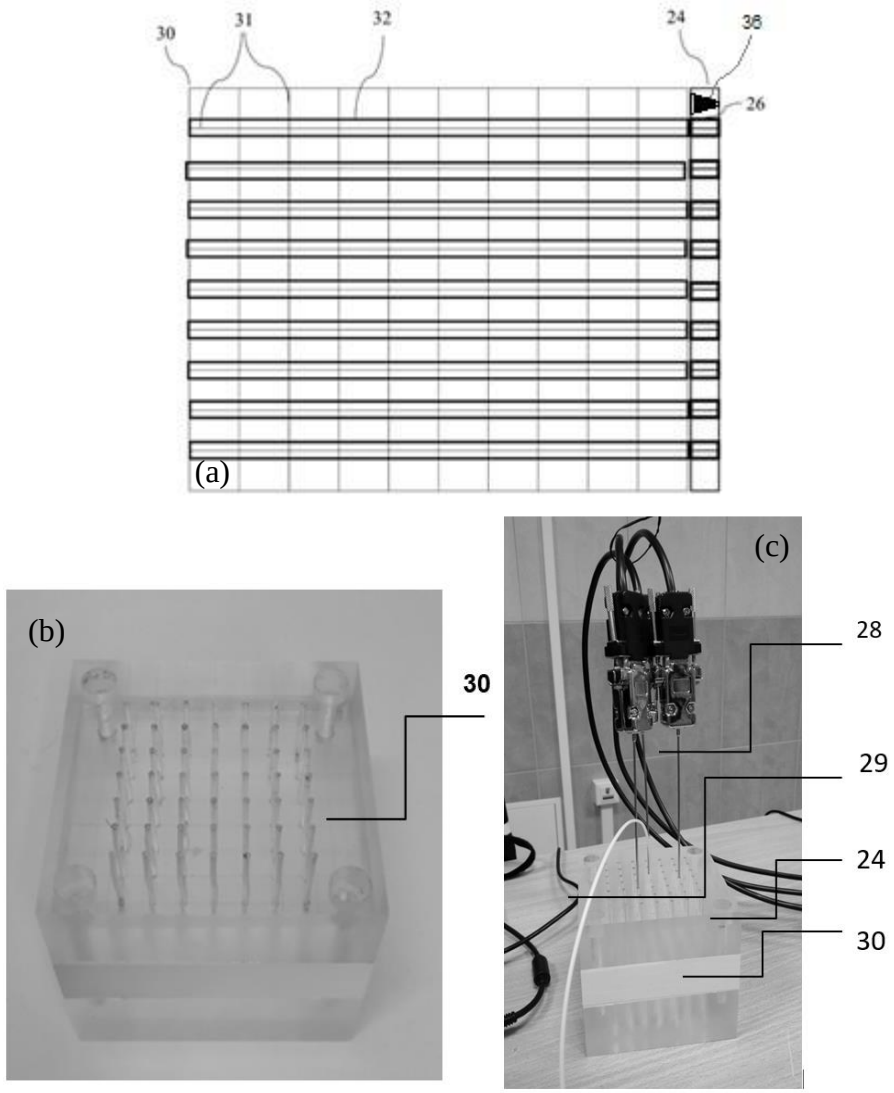

Fig. 4.6. A cube of the brachytherapy phantom (30) (for the brachytherapy planning) which contains a mesh-work of the X-Y-Z coordinate labels (31) and catheter installation groves (32) and which is attached to the synchronous positioning and dosimetry apparatus through a base plate (24, Fig. 4.4) provided with a plurality of installation holes (26).

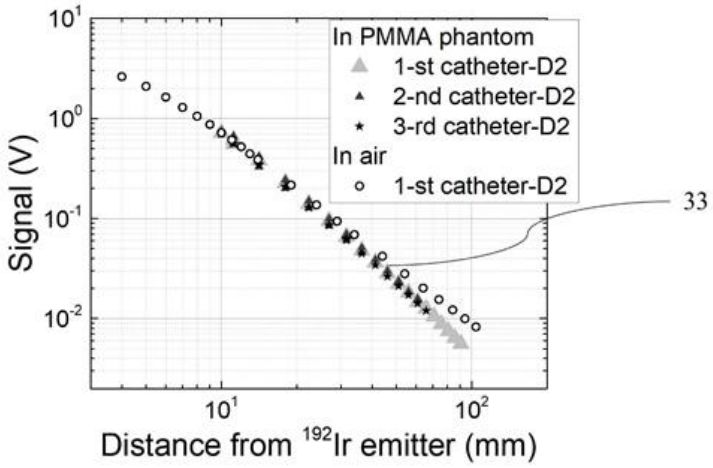

Fig. 4.7. The calibration characteristic (33) of dosimeter signal as a function of distance from the ^{192}Ir radionuclide emitter when using different type catheters (*C*) and phantom environments.

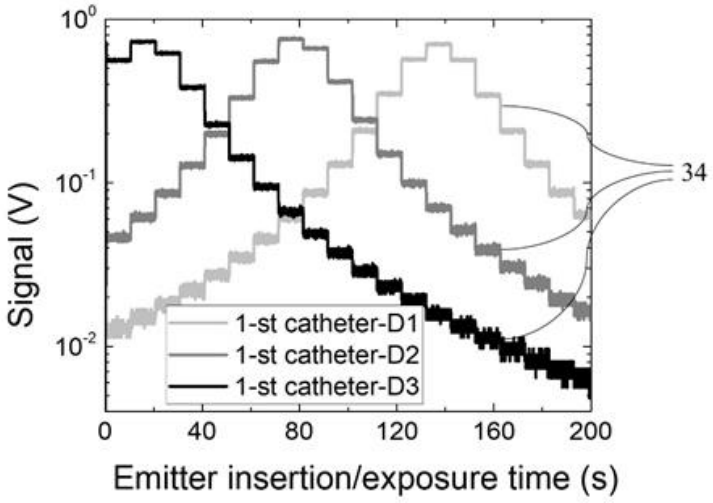

Fig. 4.8. The calibration histogram obtained varying position of the ^{192}Ir radioisotope emitter within single needle-type catheter for different dosimeters (34).

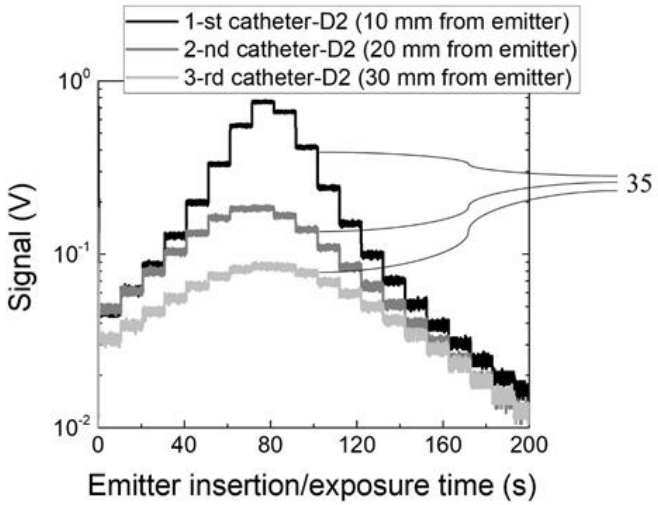

Fig. 4.9. The calibration histograms recorded varying the position of the ^{192}Ir radioisotope emitter in series within various needle-type catheters (35).

The radionuclide emitter is then inserted into the central radiation catheter (*O*), as illustrated in Figure 4.5, installed within patient's body or brachytherapy phantom, to compose the centred (at *O*) coordinate system, where shortly inserted radionuclide serves as a beacon for calibration of the initial positions of the probes containing sensors (n=1, 2, 3) located at the distances $X_{i1,j}, X_{i2,j}, X_{i3,j}$ from a trial radionuclide. Here, $i=1, 2, 3$ is the index of the probes. The spatial coordinates (those coincide with distances $X_{i1,j}, X_{i2,j}, X_{i3,j}$ for the system of catheter displacement centred at *O*) are determined using these distances from radionuclide to the definite sensor ($X_{i1,j}, X_{i2,j}, X_{i3,j}$) within the specific probe (*i)* and displaced along the active probe of length (*L*), as illustrated in Figure 4.5. Values of distances $X_{i1,j}, X_{i2,j}, X_{i3,j}$ are extracted using the sensor response amplitudes dependent on distance r^{**}, registered under shortly excited sensors by shortly inserted radionuclide, and obtained by calibration measurements.

The parameters are extracted using optimization procedures for all the detectors involved within position–dosimetry scanner. The dose (D) is evaluated using the measured dose rate ($\partial D(r)/\partial t$) signals as [145]:

$$\dot{D}(r,\theta) = S_k \cdot \Lambda \cdot \frac{G(r,\theta)}{G(r_0,\theta_0)} \cdot g(r) \cdot F(r,\theta), \qquad (4.1)$$

where, $G(r_0, \Theta_0)$ is the initial geometrical-factor function for a single sensor. The dose values $D(r_t, t_e)$ within dosimetry map are obtained from the dose rate data using a dwelling time (t_E) of irradiation as [145, 151]:

$$D(r_t, t_e) = [\partial D(r)/\partial t] \times t_E. \qquad (4.2)$$

The distance-position-dose values are obtained from the calibrated characteristics of the product $D(r,t_e)\times r^{**}$ being a linear function of a distance between the nuclide and the sensor r^{**}. The shortest distance is evaluated replacing the generalized factor r^{**} by actual R_i *one* ascribed to each (i) probe. The position S_i of the scintillator within the strip array of sensors is also related to the strip length ΔL=0 (Figure 4.10) measured relative to a bottom of the phantom and catheter.

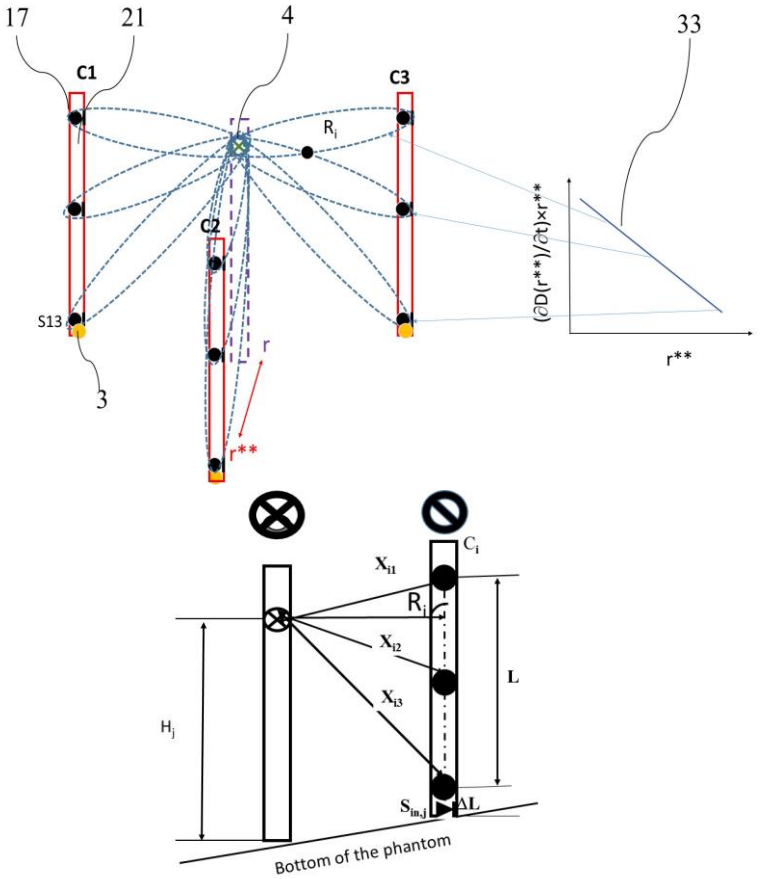

Fig. 4.10. A sketch of synchronous positioning and dosimetry algorithm using 3D synchronous scanner made of a system of internal scintillator sensors operating as beacons installed within, at least, three needle-type scaling catheters (C_1, C_2, C_3) those are positioned within phantom for brachytherapy procedure planning. On the right hand figure, the procedure of evaluation of the distance R_i from the radiation source (within a calibration catheter) to the specific probe (i) is implemented using three sensors (n= 1, 2, 3) located at locations X_{i1}, X_{i2}, X_{i3} from radionuclide (where i= *1, 2, 3* is the number of the

probes) and of the height coordinate H_j (within the horizontal (slice) section plane *j*) measured from the bottom of a phantom across its vertical position.

4.4. Algorithms and software for the in situ measurements of local accumulated dose

The algorithm used to identify the localization of the radiation source (for instance, $X_{i1,j}$) within a phantom is based on determination of sensor response, dependent on irradiation flux/dose rate, which decreases with enhancement of a distance R_i (from the radiation source) as the reciprocal function of R_i^2 (i.e. being the $1/R_i^2$, type function) when single directional variations are considered. The coordinates of the radiation source in a phantom are determined as follows:

- The altitude of a triangle R_i from the radiation source to the specific (*i*) probe (Figure 4.10), containing sensors (n=1, 2, 3) located at $X_{i1,j}, X_{i2,j}, X_{i3,j}$ from radionuclide (where *i=1, 2, 3* is the number of the probes), is related to the spatial coordinates (distances from radionuclide to the definite sensors ($X_{i1,j}, X_{i2,j}, X_{i3,j}$) within the specific probe displaced along active probe length (L) and can be evaluated by analyzing triangle (sketched on Figure 12) with sides of length L, $X_{i1,j}, X_{i3,j}$, and the semi-perimeter $s= (L + X_{i1,j} + X_{i3,j})/2$. The length of the altitude can then be expressed using Heron's formulae [152]

$$R_i = 2\,\frac{\sqrt{s(s-L)(s-X_{i1,j})(s-X_{i3,j})}}{L}. \qquad (4.3)$$

The latter relation is derived by equating the triangle area expressions ascribed to the same triangle composed of (1/2)×base(L)×altitude(R_i) and that described by the Heron's formula $\sqrt{s(s-l)(s-X_{i1,j})(s-X_{i3,j})}$ [152] in terms of the lengths. The altitude length R_i can also be evaluated by using equivalent form of the equation 4.3:

$$R_i = \frac{\sqrt{(X_{i1,j}+X_{i3,j}+L)(-X_{i1,j}+X_{i3,j}+L)(X_{i1,j}-X_{i3,j}+L)(X_{i1,j}+X_{i3,j}-L)}}{2L}. \qquad (4.4)$$

- The height coordinate H_j related to each sensor n within horizontal (slices) section planes *j*, measured from the bottom of a phantom and ascribed to the vertical position of the radiation source within 3-D phantom, is evaluated (according to the illustration shown in Figure 4.12) using equation (5), as:

$$H_j = \sqrt{X_{i3,j}^2 - R_i^2} + \Delta L \qquad (4.5)$$

- The instantaneous 3-D coordinates of the radiation source within the horizontal section planes *j* (Figure 4.13), can be evaluated by determining the

intersection points *O* of all the (*i*) probes located (within definite horizontal plane) at different distances R_{1j}, R_{2j} and R_{3j} *(i=1,2,3)* relative to an instantaneous source position (similar to illustration in Figure 4.13). It should be obtained a solution of a set (for instance, by considering the set of sensors *n*=1) of equations:

$$\begin{cases} (X - X_1)^2 + (Y - Y_1)^2 = R_1^2 \\ (X - X_2)^2 + (Y - Y_2)^2 = R_2^2 \\ (X - X_3)^2 + (Y - Y_{31})^2 = R_3^2 \end{cases} \quad (4.6)$$

- Further, the 3D coordinate system including each horizontal plane *j* is constructed by making the meshes of the coaxial circles surrounding each (*i*) cylindrical probe and solving a set of equations:

$$\{(X - X_{in,j})^2 + (Y - Y_{in,j})^2 + (Z - Z_{in,j})^2 = R_i^2 \quad (4.7)$$

- There, the first circle is centred at the axis of every cylindrical probe and is chosen to be such to include the nearest nodes of the phantom mesh within any set of planar coordinates (to cover the scaling-calibration base plate with a grid-shaped coordinate scale indicator and 3-D phantom). The radius of the successive circles is subsequently increased by a definite step within the evaluation mesh according to the desirable precision (to construct the initial coordinate mesh of the discrete pitches). Thereby, the principle coordinates of the mesh are set by calibrating the distances among the probes (catheters C_i equipped with sensors *n*).

- The algorithm of dose calculation is based on the two-dimensional formalism (equation (1)) described in 2D AAPM TG-43 [151]. The phantom horizontal plane cross section *j* is usually divided into squares (for instance, of 8×8 extent) and each square is divided into segments (dose points) P_{kj} (where *k*= 1, 2, 3, ..., 6399, 6400 is the number of the segment, for instance of 10×10 extent) similar as in a fragment of the phantom in a Figure 4.14. Each dose point is calculated independently using TG-43 formalism [151] based on the functions of the radial distance r^{**}_{kj} from the radiation source and a polar angle coordinate θ_{kj}, in the cylindrical coordinate system, meanwhile β_{kj} is the angle subtended by the tips of radionuclide with respect to the point under test P_{kj}. This algorithm allows to consider dose distribution within the cross-sectional planes *j* (slices).

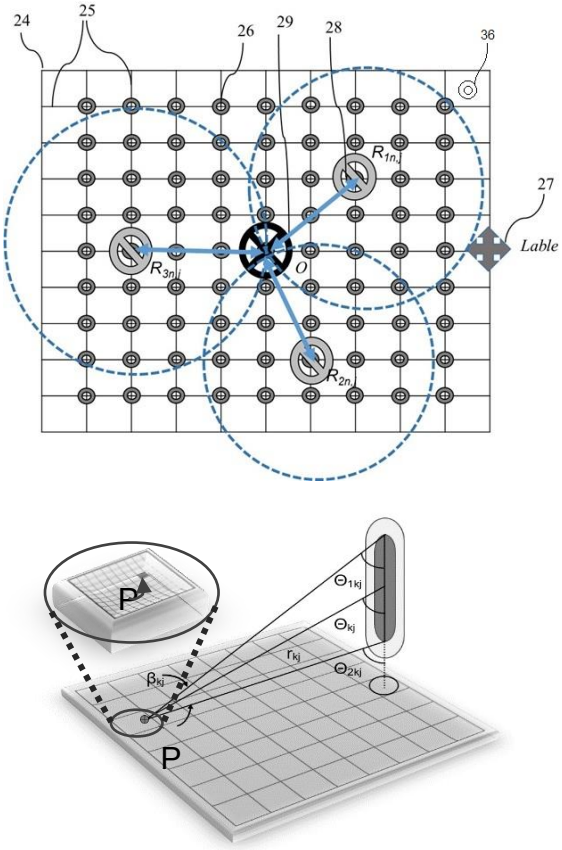

Fig. 4.11. A sketch of the evaluation algorithm to determine an instant coordinate (x_0, $y_{0,}$ z_0) of the radionuclide relative to the definite slice *j* using an intersection point *O* of circles centred at definite probes (*i*) and sensors (*n*) located at distances $R_{in,j}$ measured relative a position of the radiation source. Each horizontal section plane *j* is constructed by the meshes of the coaxial circles which is surrounding each of the cylindrical probe (*i*). $R_{i,n,j}$ from the definite probe axis to a point under examination.

C are expressed as $\Delta X = c \times \Delta t$ with *c* being the speed of light. On the other hand, additional correction should also be made concerning the actual strip height and its position ΔL relative to a bottom of the phantom.

Deviations from the planned doses and positions can be estimated by comparing the maps obtained using the phantom and those registered in patient‘s body.

The tentative brachytherapy planning instrumentation have been produced after trying of several type commercial pin sensors, made of Si and

GaN materials discussed in the material research (1-3) Chapters of this dissertation.

5. SUMMARY OF DISSERTATION RESULTS AND CONCLUSIONS

1. In this work, the analysis of the electrical characteristics in pristine, electron as well as proton irradiated and subsequently annealed $Si_{1-x}Ge_x$ samples with different Ge contents was performed. The routine capacitance deep-level transient spectroscopy (C-DLTS) and Laplace DLTS (L-DLTS) techniques [19,20] were combined to clarify the deep trap spectrum. The traps were identified by analysing the activation energy values reported in the literature. It was revealed that the carbon–oxygen metastable complexes (C_iO_i *) were transformed into the stable-state complexes (C_iO_i) under 125 °C annealing for 15 min of the irradiated samples.

2. It was deduced from C-DLTS and L-DLTS spectra that the carbon/oxygen associated complexes prevailed in the pristine $Si_{0.949}Ge_{0.051}$ alloys, irradiated with 5.5 MeV electrons.

3. The double interstitial and oxygen (I_2O) complexes and the vacancy, di-vacancy and tri-vacancy ascribed traps were revealed in the irradiated samples.

4. The vacancy–oxygen (VO) and the boron-oxygen (B_iO_i) complexes, as well as vacancy clusters, were revealed to be the dominant electron traps. It was proven that boron–oxygen complexes (B_iO_i) of stable form [$B_iO_i^A$] prevail in the temperature range of 65–280 K. It was shown that shifts of activation energy of the minority carrier traps appear due to an increase in Ge content in SiGe alloys.

5. The microwave probed photoconductivity, pulsed barrier capacitance transients and spectra of steady-state photo-ionization in pristine, 5.5 MeV electron and 1.6 MeV proton irradiated Si and SiGe diodes with n^+p structure were examined. It has been revealed that both carrier recombination and trapping lifetimes decrease near-reciprocally as a function of density of radiation defects acting as carrier capture and thermal emission centres, with predominance of point radiation defects. It has been hypothesized that the single-type deep centres are involved in both carrier photo-generation and thermal emission processes.

6. It has been revealed that Ge can be used as an isovalent impurity, instead of carbon, within engineering of the strong field layers in advanced low gain avalanche detectors made of Si.

7. The bi-stable boron–oxygen (B_iO_i) complex was revealed to be the prevailing minority carrier trap in *p*-type $Si_{1-x}Ge_x$ alloy diodes.

8. The relatively small density of electrically active boron–oxygen complexes in SiGe alloy with 5% of Ge content can be explained either by the fact that boron-doped $Si_{0.95}Ge_{0.05}$ diodes are more resistive to the appearance of the "acceptor removing" effect in comparison with boron-doped Si and $Si_{0.99}Ge_{0.01}$ diodes or due to Ge content modified density of the interstitial boron (B_i). The role of the boron–oxygen (B_iO_i) complex is significantly reduced in $Si_{0.95}Ge_{0.05}$ alloy due to local strain.

9. The B_iO_i defect is responsible for the *B* acceptor removal inp-type Si and SiGe materials and the degrading of their radiation hardness. Therefore, transformations of the radiation-induced B_iO_i defect in $Si_{0.95}Ge_{0.05}$ diodes can pave an advanced technology in enhancement of the detector radiation hardness based on SiGe alloys with elevated Ge content.

10. It was also shown that the values of activation energy of radiation-induced traps of minority carriers shift near-linearly to the higher values with the increase in Ge content in the range of x=0.01-0.05 in *p*-type $Si_{1-x}Ge_x$ alloys.

11. Clear correlation among MW-PC, PL and CCE characteristics dependent on neutron irradiation fluence has been unveiled in sensors made of the ammono-thermal technology GaN materials and irradiated with reactor neutrons. It has been proved that AT GaN material doped with Mg is the most suitable for fabrication of rather thick particle detectors.

12. The brachytherapy planning technology using phantoms and a prototype instrumentation for remote control of the radionuclide location as well as for in situ dosimetry mapping has been created and installed at National Cancer Institute. The EPO patent application has been submitted [EPO-1].

ACKNOWLEDGEMENTS

First of all, I would like to thank my scientific supervisor prof. habil. Dr. Eugenijus Gaubas, for the support, understanding, boundless trust and non-exceeding patience. I appreciate the opportunity to work with prof. habil. dr. Eugenijus Gaubas and learn the methods.

I am also thankful to researchers of Photoelectric Phenomena research group doc. dr. T. Čeponis and dr. V. Rumbauskas for the collaboration during the improvement of instrumentation for brachytherapy applications, dr. J. Pavlov for the together implemented most of DLTS characterisation and PHD students D. Meškauskaitė and L. Deveikis for the several material characterisation experiments performed in collaboration.

I am thankful to reviewers of the dissertation doc. dr. T. Šalkus and dr. A. Šilėnas for valuable suggestions to improve the work.

I would like to express my gratitude to my father Tomas Pūkas who also inspired me to choose physics studies, mother Daiva Pūkienė, sisters Karolina and Klementina, brother Konstantinas as well as my friends for being supportive during my long-lasting years of studies at Vilnius University.

I am very thankful to my wife Simona and children Albertas and Agota, for being there for me all those years and inspiring to continue my research work.

REFERENCES

1. High luminosity LHC project. Available online: https://hilumilhc.web.cern.ch/(accessedon11November2020).

2. Moll M Radiation tolerant semiconductor sensors for tracking detectors *Nucl. Instrum. Methods A* 565 (2006) 202–11.

3. CERN Available online: https:// cern.ch

4. Adam, W.; Bergauer, T.; Brondolin, E.; Dragicevic, M.; Friedl, M.; Frühwirth, R.; Hoch, M.; Hrubec, J.; König, A.; Steininger, H.; et al. P-type silicon strip sensors for the new CMS tracker at HL-LHC. *J. Instrum.* **2017**, *12*, P06018. https://doi.org/10.1088/1748-0221/12/06/p06018.

5. Ullan, M.; Diez, S.; Lozano, M.; Pellegrini, G.; Knoll, D.; Heinemann, B. Combined effect of bias and annealing in gamma and neutron radiation assurance tests of SiGe bipolar transistors for HEP applications. *Solid State Electron.* **2011**, *56*, 179–184.

6. Makarenko, L.F.; Lastovskii, S.B.; Korshunov, F.P.; Moll, M.; Pintilie, I.; Abrosimov, N.V. Formation and annealing of boron-oxygen defects in irradiated silicon and silicon-germanium n^+-p structures. *AIP Conf. Proc.* **2014**, *1583*, 123–126.

7. Sugiura M, Kushimoto M, Mitsunari T, Yamashita K, Honda Y, Amano H, Inoue Y, Mimura H, Aoki T and Nakano T Study of radiation detection properties of GaN pn diode *Jpn. J. Appl. Phys.* **55 (**2016**)** 05FJ02.

8. Vaitkus J, Gaubas E, Kazukauskas V, Blue A, Cunningham W, Rahman M, Smith K and Sakai S A new radiation hard semiconductor - semi-insulating GaN: Photoelectric properties *AIP Conference Proceedings* **CP772** (2005) 207–8.

9. Sellin P J and Vaitkus J New materials for radiation hard semiconductor dectectors *Nucl. Instrum. Methods A* **557** (2006) 479–89.

10. Imanishi M, Todoroki Y, Murakami K, Matsuo D, Imabayashi H, Takazawa H, Maruyama M, Imade M, Yoshimura M and Mori Y Dramatic

reduction of dislocations on a GaN point seed crystal by coalescence of bunched steps during Na-flux growth *J. Cryst. Growth* **427** (2015) 87–93.

11. Bockowski M, Iwinska M, Amilusik M, Fijalkowski M, Lucznik B and Sochacki T Challenges and future perspectives in HVPE-GaN growth on ammonothermal GaN seeds *Semicond. Sci. Technol.* **31 (**2016**)** 93002.

12. AMMONO. Available online: www.ammono.com

13. Kucharski R, Zajac M, Puchalski A, Sochacki T, Bockowski M, Weyher J L, Iwinska M, Serafinczuk J, Kudrawiec R and Siemiątkowski Z Ammonothermal growth of GaN crystals on HVPE-GaN seeds prepared with the use of ammonothermal substrates *J. Cryst. Growth* **427** (2015) 1–6.

14. Graf T, Gjukic M, Hermann M, Brandt M S, Stutzmann M and Ambacher O 2003 Spin resonance investigations of Mn^{2+} in wurtzite GaN and AlN films *Phys. Rev. B* **67** (2003) 165215.

15. Zvanut M E, Uprety Y, Dashdorj J, Moseley M and Alan Doolittle W Passivation and activation of Mg acceptors in heavily doped GaN *J. Appl. Phys.* **110** (2011) 44508.

16. Besleaga, C.; Kuncser, A.; Nitescu, A.; Kramberger, G.; Moll, M.; Pintilie, I. Bistability of the BiOi complex and its implications on evaluating the "acceptor removal" process in p-type silicon. *Nucl. Instrum. Methods Phys. Res. Sect. A Accel. Spectrom. Detect. Assoc. Equip.* **1017** (2021) 165809.

17. Liao, C.; Fretwurst, E.; Garutti, E.; Schwandt, J.; Moll, M.; Himmerlich, A.; Gurimskaya, Y.; Pintilie, I.; Nitescu, A.; Li, Z.; et al. The boron-oxygen (BiOi) defect complex induced by irradiation with 23 GeV protons in p-type epitaxial silicon diodes. *IEEE Trans. Nucl. Sci.* (2021).

18. Moll, M. Acceptor removal—Displacement damage effects involving the shallow acceptor doping of p-type silicon devices. *PoS* ***Vertex2019*** (2020) 027.

19. Gurimskaya, Y.; de Almeida, P.D.; Garcia, M.F.; Suau, I.M.; Moll, M.; Fretwurst, E.; Makarenko, L.; Pintilie, I. Radiation damage in p-type EPI silicon pad diodes irradiated with protons and neutrons. *Nucl. Instruments*

Methods Phys. Res. Sect. A Accel. Spectrom. Detect. Assoc. Equip. ***958*** (2020)162221.

20. Mukashev, B.N.; Abdullin, Kh.A.; Gorelkinskii, Yu.V. Metastable and bistable defects in silicon. *PHYS-USP+* **43** (2000)139–150.

21. Gaubas E, Simoen E and Vanhellemont J Review—Carrier lifetime spectroscopy for defect characterization in semiconductor materials and devices *ECS J. Solid State Sci. Technol.* **5** (2016) P3108–37.

22. Gaubas E, Kaniava A and Vaitkus J Investigation of recombination parameters in silicon structures by infrared and microwave transient absorption techniques *Semicond. Sci. Technol.* **12** (1997) 1–10.

23. Gaubas E, Vaitkus J and Smith K M Monitoring of carrier lifetime in GaAs substrate–epi-layer structures by space-resolved transient microwave absorption *Nucl. Instrum. Methods A* **460** (2001) 35–40.

24. RD50—Radiation hard semiconductor Devices for Very High Luminosity Colliders. Available online: www.cern.ch/rd50 (accessed on 25 November 2020).

25. Besleaga, C.; Kuncser, A.; Nitescu, A.; Kramberger, G.; Moll, M.; Pintilie, I. Bistability of the BiOi complex and its implications on evaluating the "acceptor removal" process in p-type silicon. *Nucl. Instrum. Methods Phys. Res. Sect. A Accel. Spectrom. Detect. Assoc. Equip.* **2021**, *1017*, 165809.

26. Ullan, M.; Diez, S.; Lozano, M.; Pellegrini, G.; Knoll, D.; Heinemann, B. Combined effect of bias and annealing in gamma and neutron radiation assurance tests of SiGe bipolar transistors for HEP applications. *Solid State Electron.* **2011**, *56*, 179–184.

27. Haugerud, B.M.; Pratapgarhwala, M.M.; Comeau, J.P.; Sutton, A.K.; Prakash, A.P.G.; Cressler, J.D.; Marshall, P.W.; Marshall, C.J.; Ladbury, R.L.; El-Diwany, M.; et al. Proton and gamma radiation effects in a new first-generation SiGe HBT technology. *Solid State Electron.* **2006**, *50*, 181–190.

28. Grabchikov, S.S.; Lastovskii, S.B.; Solobai, A.A.; Trukhanov, A.V.; Chushkova, D.I. Sythesis features and radiation protection efficiency of

multilayer structures based on Ni-Fe electrodeposited films. *Proc. Natl. Acad. Sci. Belarus. Phys.-Tech. Ser.* **2017**, *2*, 23–29.

29. Makarenko, L.F.; Lastovskii, S.B.; Korshunov, F.P.; Moll, M.; Pintilie, I.; Abrosimov, N.V. Formation and annealing of boron-oxygen defects in irradiated silicon and silicon-germanium n^+-p structures. *AIP Conf. Proc.* **2014**, *1583*, 123–126.

30. Li, Y.; Li, J.; Du, J.; Han, J.; Xiang, Q.; Zhang, C. Influence of fast neutron and gamma irradiation on the thermoelectric properties of n-type and p-type SiGe alloy. *J. Nucl. Mater.* **2020**, *528*, 151856.

31. Nylandsted Larsen, A.; Bro Hansen, A.; Mesli, A. Irradiation induced defects in SiGe. *Mat. Sci.Eng. B* **2008**, *154–155*, 85–89.

32. Mamor, M.; Pipeleers, B.; Auret, F.D.; Vantomme, A. Defect production in strained p-type $Si_{1-x}Ge_x$ by Er implantation. *J. Appl. Phys.* **2011**, *109*, 013715.

33. Kwak, D.W.; Li, D.W.; Oh, J.S.; Li, Y.H.; Cho, H.Y. Extended deep level defects in Ge-condensed SiGe-on—Insulator structures fabricated using proton and helium implantations. *Thin Solid Films* **2012**, *520*, 5593–5596.

34. Markevich, V.P.; Peaker, A.R.; Murin, L.I.; Abrosimov, N.V. Oxygen-related radiation-induced defects in SiGe alloys. *J. Phys. Condens. Matter.* **2003**, *15*, S2835–S2842.

35. Pittet P, Guo N L, Jean M G, Jean M B, Anas I, Jean Y G and Balosso J 2009 PL characterization of GaN scintillator for radioluminescence-based dosimetry *Opt. Mater.* **31** 1421–4.

36. Pittet P, Lu G N, Galvan J M, Loisy J Y, Ismail A, Giraud J Y and Balosso J 2009 Implantable real-time dosimetric probe using GaN as scintillation material *Sensors Actuators A Phys.* **151** 29–34.

37. Wang R, Pittet P, Ribouton J, Lu G-N, Chaikh A and Ahnesjö A 2013 Implementation and validation of a fluence pencil kernels model for GaN-based dosimetry in photon beam radiotherapy *Phys. Med. Biol.* **58** 6701–12.

38. Reshchikov M A and Morkoç H 2005 Luminescence properties of defects in GaN *J. Appl. Phys.* **97** 61301.

39. Polyakov A, Usikov A, Theys B, Smirnov N, Govorkov A, Jomard F, Shmidt N and Lundin W 2000 Effects of proton implantation on electrical and recombination properties of n-GaN *Solid. State. Electron.* **44** 1971–83.

40. Gaubas E, Ceponis T, Kuokstis E, Meskauskaite D, Pavlov J and Reklaitis I 2016 Study of charge carrier transport in GaN sensors *Materials* **9** 293.

41. Son N T, Hemmingsson C G, Morishita N, Ohshima T, Paskova T, Evans K R, Usui A, Isoya J, Monemar B and Janzén E 2010 Radiation-induced defects in GaN *Phys. Scr.* **T141** 14015.

42. Zhang M I, Yang R X, Wang X L and Liu S F 2015 Neutron irradiation effect on GaN-based materials *ECS Trans.* **66** 33–52.

43. Rodrigues J, Peres M, Soares M J, Lorenz K, Marques J G, Neves A J and Monteiro T 2012 Influence of neutron irradiation and annealing on the optical properties of GaN *Phys. Status Solidi C* **9** 1016-20.

44. Perez-Taborda, J.A.; Caballero-Calero, O.; Martin-Gonzalez, M. Silicon-germanium (SiGe) nanostructures for thermoelectric devices: Recent advances and new approaches to high thermoelectric efficiency. In *New Research on Silicon—Structure, Properties, Technology*; Talanin, V.I., Ed.; Intech: Rijeka, Croatia, 2017; pp. 183–206.

45. Heinemann, B.; Rucker, H.; Barth, R.; Barwolf, F.; Drews, J.; Fischer, G.G.; Fox, A.; Fursenko, O.; Grabolla, T.; Herzel, F.; et al. SiGe HBT with fx/fmax of 505 GHz/720 GHz. In Proceedings of the 2016 IEEE International Electron Devices Meeting (IEDM); San Francisco, CA, USA, 3–7 December 2016.

46. Yang, Y.; Liu, S.; Bian, X.; Feng, J.; An, Y.; Yuan, C. Morphology- and porosity-tunable synthesis of 3D nanoporous SiGe alloy as a high-performance lithium-ion battery anode. *ACS Nano* **2018**, *12*, 2900–2908, doi:10.1021/acsnano.8b00426.

47. Yonenaga, I. Si_xGe_{1-x} bulk crystals. In *Reference Module in Materials Science and Materials Engineering*; Hashmi, S., Ed.; Elsevier: Amsterdam, Netherlands, 2016; pp. 8647–8651.

48. Kissinger, G.; Pizzini, S. *Silicon, Germanium, and their alloys: growth, defects, impurities, and nanocrystals*, 1st ed.; CRC Press: Boca Raton, FL, USA, 2015.

49. Usami, N. 4-Types of silicon–germanium (SiGe) bulk crystal growth methods and their applications. In *Silicon–Germanium (SiGe) Nanostructures: Production, Properties and Applications in Electronics*; Shiraki, Y., Usami, N., Eds.; Woodhead Publishing Limited: Sawston, UK, 2011; pp. 72–82.

50. Markevich, V.P.; Peaker, A.R.; Murin, L.; Coutinho, J.; Torres, V.J.B.; Jones, R.; Öberg, S.; Briddon, P.; Auret, F.; Abrosimov, N. Electronic properties of vacancy–oxygen complexes in SiGe alloys. *Phys. B: Condens. Matter* **2003**, *340–342*, 790–794, doi:10.1016/j.physb.2003.09.214.

51. Coutinho, J.; Balsas, Álvaro; Torres, V.J.B.; Briddom, P.; Barroso, M. Electronic levels of interstitial carbon and carbon–oxygen centers in SiGe alloys. *Mater. Sci. Eng. B* **2004**, *114*, 304–306, doi:10.1016/j.mseb.2004.07.048.

52. Hayama, S.; Davies, G.; Tan, J.; Markevich, V.P.; Peaker, A.R.; et al. Carbon-related centers in irradiated *SiGe alloys. Physica B* **2003**, *340–342*, 823–826.

53. Skardi, H.A.; Hansen, A.B.; Mesli, A.; Larsen, A.N. The di-vacancy in particle-irradiated, strain-relaxed SiGe. *Nucl. Instrum. Methods Phys. Res. Sect. B: Beam Interact. Mater. Atoms* **2002**, *186*, 195–200, doi:10.1016/s0168-583x(01)00893-x.

54. Gaubas, E.; Ceponis, T.; Uleckas, A.; Vaitkus, J.; Raisanen, J. Recombination characteristics in 2–3MeV protons irradiated FZ Si. *Nucl. Instruments Methods Phys. Res. Sect. A: Accel. Spectrometers Detect. Assoc. Equip.* **2010**, *612*, 559–562, doi:10.1016/j.nima.2009.08.013.

55. Markevich, V.P.; Peaker, A.R.; Çapan, I.; Lastovskii, S.; Dobaczewski, L.; Emtsev, V.; Abrosimov, N. Electrically active defects induced by irradiations with electrons, neutrons and ions in Ge-rich SiGe alloys. *Phys. B Condens. Matter* **2007**, *401–402*, 184–187, doi:10.1016/j.physb.2007.08.142.

56. Makarenko, L.F.; Lastovski, S.B.; Yakushevich, H.S.; Gaubas, E.; Pavlov, J.; Kozlovski, V.V.; Moll, M.; Pintilie, I.; Pavlov, J.; Kozlovski, V.V. Formation of a bistable interstitial complex in irradiated p-type silicon. *Phys. Status Solidi* **2019**, *216*, 1900354, doi:10.1002/pssa.201900354.

57. Blood, P.; Orton, J.W. *The Electrical Characterization of Semiconductors: Majority Carriers and Electron States*; Academic Press Inc.: San Diego, CA, USA, 1992.

58. Peaker, A.R.; Markevich, V.P.; Hawkins, I.; Hamilton, B.; Nielsen, K.B.; Gościński, K. Laplace deep level transient spectroscopy: Embodiment and evolution. *Phys. B Condens. Matter* **2012**, *407*, 3026–3030, doi:10.1016/j.physb.2011.08.107.

59. Gaubas, E.; Ceponis, T.; Deveikis, L.; Meskauskaite, D.; Pavlov, J.; Rumbauskas, V.; Vaitkus, J.; Moll, M.; Ravotti, F. Anneal induced transformations of defects in hadron irradiated Si wafers and Schottky diodes. *Mater. Sci. Semicond. Process.* **2018**, *75*, 157–165, doi:10.1016/j.mssp.2017.11.035.

60. J. Wang, P. Mulligan, L. Brillson, L.R. Cao, Review of using gallium nitride for ionizing radiation detection, Appl. Phys. Rev. 2 (2015) 31102. doi:10.1063/1.4929913.

61. V. Moroz, H.Y. Wong, M. Choi, N. Braga, R. V. Mickevicius, Y. Zhang, T. Palacios, The impact of defects on GaN device behavior: modeling dislocations, traps, and pits, ECS J. Solid State Sci. Technol. 5 (2016) P3142–P3148. doi:10.1149/2.0211604jss.

62. M. Huhtinen, Simulation of non-ionising energy loss and defect formation in silicon, Nucl. Instruments Methods Phys. Res. Sect. A Accel. Spectrometers, Detect. Assoc. Equip. 491 (2002) 194–215. doi:10.1016/S0168-9002(02)01227-5.

63. C. Inguimbert, P. Arnolda, T. Nuns, G. Rolland, “Effective NIEL” in silicon: calculation using molecular dynamics simulation results, IEEE Trans. Nucl. Sci. 57 (2010) 1915–1923. doi:10.1109/TNS.2010.2049581.

64. M. Frentrup, L.Y. Lee, S.-L. Sahonta, M.J. Kappers, F. Massabuau, P. Gupta, R.A. Oliver, C.J. Humphreys, D.J. Wallis, X-ray diffraction analysis of cubic zincblende III-nitrides, J. Phys. D. Appl. Phys. 50 (2017) 433002. doi:10.1088/1361-6463/aa865e.

65. S.A. Kukushkin, A. V Osipov, V.N. Bessolov, B.K. Medvedev, V.K. Nevolin, K.A. Tcarik, Substrates for epitaxy of gallium nitride: new materials and techniques, Rev.Adv.Mater.Sci. 17 (2008) 1–32. doi:10.1016/S0927-796X(02)00008-6.

66. C. Chang, S. Lien, C. Liu, C. Shih, N.- Chen, P. Chang, H. Peng, T. Tang, W. Lien, Y. Wu, K. Wu, J. Chen, C. Liang, Y. Chen, T. Lu, T. Lin, Effect of buffer layers on electrical, optical and structural properties of AlGaN/GaN heterostructures grown on Si, Jpn. J. Appl. Phys. 48 (2006) 2616. doi:10.1143/JJAP.45.2516.

67. A. Sakai, H. Sunakawa, A. Usui, Defect structure in selectively grown GaN films with low threading dislocation density, Appl. Phys. Lett. 71 (1998) 2259. doi:10.1063/1.120044.

68. C. Boney, A. Carreno, A. Bensaoula, Z. Zhang, H.D. Lee, W.K. Chu, A. Vigliante, Reduction of defects in RF-MBE grown GaN on sapphire by optimization of nitridation temperature and intermediate layer parameters, in: Int. Conf. Mol. Bean Ep., IEEE, San Francisco, 2002: pp. 205–206. doi:10.1109/MBE.2002.1037831.

69. F.K. Yam, L.L. Low, S.A. Oh, Z. Hassan, Gallium nitride: an overview of structural defects, INTECH Open Access Publisher, 2011. http://cdn.intechweb.org/pdfs/20503.pdf (accessed February 13, 2018).

70. K. Motoki, T. Okahisa, S. Nakahata, N. Matsumoto, H. Kimura, H. Kasai, K. Takemoto, K. Uematsu, M. Ueno, Y. Kumagai, A. Koukitu, H. Seki, Growth and characterization of freestanding GaN substrates, J. Cryst. Growth. 237–239 (2002) 912–921. doi:10.1016/S0022-0248(01)02078-4.

71. Y. Oshima, T. Eri, M. Shibata, H. Sunakawa, K. Kobayashi, T. Ichihashi, A. Usui, Preparation of freestanding GaN wafers by hydride vapor phase epitaxy with void-assisted separation, Jpn. J. Appl. Phys. 42 (2003) L1–L3. doi:10.1143/JJAP.42.L1.

72. T. Wei, J. Yang, Y. Wei, Z. Huo, X. Ji, Y. Zhang, J. Wang, J. Li, S. Fan, Cross-stacked carbon nanotubes assisted self-separation of free-standing GaN substrates by hydride vapor phase epitaxy, Sci. Rep. 6 (2016) 28620. doi:10.1038/srep28620.

73. D. Ehrentraut, E. Meissner, M. Bockowski, Technology of gallium nitride crystal growth, Springer-Verlag, 2010.

74. K. Xu, J.-F. Wang, G.-Q. Ren, Progress in bulk GaN growth, Chinese Phys. B. 24 (2015) 66105. doi:10.1088/1674-1056/24/6/066105.

75. M.E. Levinshtein, S.L. Rumyantsev, M. Shur, Properties of advanced semiconductor materials : GaN, AlN, InN, BN, SiC, SiGe, Wiley, 2001.

76. V. Avrutin, D.J. Silversmith, Y. Mori, F. Kawamura, Y. Kitaoka, H. Morkoc, Growth of bulk GaN and AlN: progress and challenges, Proc. IEEE. 98 (2010) 1302–1315. doi:10.1109/JPROC.2010.2044967.

77. P. Boguslawski, E.L. Briggs, J. Bernholc, Amphoteric properties of substitutional carbon impurity in GaN and AlN, Appl. Phys. Lett. 69 (1998) 233. doi:10.1063/1.117934.

78. R.S. Sussmann, CVD diamond for electronic devices and sensors, J. Wiley, 2009.

79. E.A. Jones, F.F. Wang, D. Costinett, Review of commercial GaN power devices and GaN-based converter design challenges, IEEE J. Emerg. Sel. Top. Power Electron. 4 (2016) 707–719. doi:10.1109/JESTPE.2016.2582685.

80. S. Suihkonen, S. Pimputkar, J.S. Speck, S. Nakamura, Infrared absorption of hydrogen-related defects in ammonothermal GaN, Appl. Phys. Lett. 108 (2016) 202105. doi:10.1063/1.4952388.

81. M. Sumiya, S. Fuke, Review of polarity determination and control of GaN, MRS Internet J. Nitride Semicond. Res. 9 (2004) e1. doi:10.1557/S1092578300000363.

82. R. Velazquez, A. Aldalbahi, M. Rivera, P. Feng, Fabrications and application of single crystalline GaN for high-performance deep UV photodetectors, AIP Adv. 6 (2016) 85117. doi:10.1063/1.4961878.

83. Pearton S J, Kang B S, Kim S, Ren F, Gila B P, Abernathy C R, Lin J and Chu S N G 2004 GaN-based diodes and transistors for chemical, gas, biological and pressure sensing *J. Phys. Condens. Matter* **16** R961–94.

84. Gaubas E, Ceponis T, Jasiunas A, Kovalevskij V, Meskauskaite D, Pavlov J, Remeikis V, Tekorius A and Vaitkus J 2014 Correlative analysis of the in situ changes of carrier decay and proton induced photoluminescence characteristics in chemical vapor deposition grown GaN *Appl. Phys. Lett.* **104** 62104

85. Fujita S 2015 Wide-bandgap semiconductor materials: For their full bloom *Jpn. J. Appl. Phys.* **54** 030101-12.

86. Gaubas E, Kazlauskas K, Tomašiūnas R, Vaitkus J and Žukauskas A 2004 Radiation-defect-dependent photoconductivity transients and photoluminescence in semi-insulating GaN *Appl. Phys. Lett.* **84** 5258.

87. Gaubas E, Kovalevskij V, Kadys A, Gaspariunas M, Mickevicius J, Jasiunas A, Remeikis V, Uleckas A, Tekorius A, Vaitkus J and Velicka A 2013 In situ variations of recombination characteristics in MOCVD grown GaN epi-layers during 1.7 MeV protons irradiation *Nucl. Instrum. Methods B* **307** 370–2.

88. Gaubas E, Brytavskyi I, Ceponis T, Jasiunas A, Kalesinskas V, Kovalevskij V, Meskauskaite D, Pavlov J, Remeikis V, Tamulaitis G and Tekorius A 2014 In situ variations of carrier decay and proton induced luminescence characteristics in polycrystalline CdS *J. Appl. Phys.* **115** 243507.

89. Polyakov A, Usikov A, Theys B, Smirnov N, Govorkov A, Jomard F, Shmidt N and Lundin W 2000 Effects of proton implantation on electrical and recombination properties of n-GaN *Solid. State. Electron.* **44** 1971–83.

90. Gaubas E, Ceponis T, Kalesinskas V, Pavlov J and Vysniauskas J 2015 Simulations of operation dynamics of different type GaN particle sensors *Sensors* **15** 5429–73

91. R. Kucharski, M. Zajac, A. Puchalski, T. Sochacki, M. Bockowski, J.L. Weyher, M. Iwinska, J. Serafinczuk, R. Kudrawiec, Z. Siemiątkowski, Ammonothermal growth of GaN crystals on HVPE-GaN seeds prepared with the use of ammonothermal substrates, J. Cryst. Growth. 427 (2015) 1–6. doi:10.1016/j.jcrysgro.2015.06.019.

92. Bockowski M, Iwinska M, Amilusik M, Fijalkowski M, Lucznik B and Sochacki T 2016 Challenges and future perspectives in HVPE-GaN growth on ammonothermal GaN seeds *Semicond. Sci. Technol.* **31** 93002.

93. J.B.Baliga, Power Semiconductor devices (PWS Publishing company, Boston, 1996).

94. S.M.Sze, Physics of Semiconductor Devices. (John Wiley & Sons, Inc., Hoboken, New Jersey 2007).

95. D. K. Schroder, *Semiconductor Material and Device Characterization* (John Wiley & Sons, New Jersey, 2006).

96. Peaker, A.R.; Markevich, V.P.; Coutinho, J. Tutorial: Junction spectroscopy techniques and deep-level defects in semiconductors. *J. Appl. Phys.* **2018**, *123*, 161559.

97. Gaubas, E.; Ceponis, T.; Vaitkus, J-V. *Pulsed Capacitance Technique for Evaluation of Barrier Structure*, LAP Lampert Academic Publishing: Berlin, Germany, 2013.

98. G. Lutz, *Semiconductor radiation detectors – device physics* (Springer, Heidelberg, 2007).

99. S. Ramo, *Currents induced by electron motion*, Associate member, I.R.E. **73** (1939).

100. W. Shockley, *Currents to conductors induced by a moving point charge*, J. Appl. Phys. **9** (1938) 635.

101. V. Eremin, N. Strokan, E. Verbitskaya, Z. Li, Nucl. *Development of transient current and charge techniques for the measurement of effective net concentration of ionized charges N_{eff} in the space charge region of p-n junction detectors*, Nucl. Instrum. Meth. A **372** (1996) 388.

102. C. Leroy, P. Roy, G. Casse, M. Glaser, E. Grigoriev, F. Lemeilleur, *Study of charge transport in non-irradiated and irradiated silicon detectors*, Nucl. Instrum. Meth. A **426** (1999) 99-108.

103. S. Uxa, R. Grill, and E. Belas, *Evaluation of the mobility-lifetime product in CdTe and CdZnTe detectors by the transient-current technique*, J. Appl. Phys. **114** (2013) 094511.

104. S. Uxa, E. Belas, R. Grill, P. Praus and R. B. James, *Effect of contact preparation on the profile of the electric field in CdZnTe detectors*, J. Phys. D: Appl. Phys. **46** (2013) 395102.

105. Z. Li, *Generalization of the modeling and design considerations of concentric and spiral Si drift detectors*, Nucl. Instrum. Meth. A 730 (2013) 73.

106. E. Verbitskaya, V. Eremin, A. Zabrodskii, Z. Li, P. Luukka, *Restriction on the gain in collected charge due to carrier avalanche multiplication in heavily irradiated Si strip detectors*, Nucl. Instrum. Meth. A **730** (2013) 66–72.

107. E. Verbitskaya, G. Ruggiero, I. Eremin, I. Ilyashenko, A. Cavallini, A. Castaldini, G. Pellegrini, M. Lozano, S. Golubkov, N. Egorov, K. Konkov, T. Tuuva, *Electrical properties of the sensitive side in Si edgeless detectors*, Nucl. Instrum. Meth. A **604** (2009) 246–249.

108. G. Kramberger, V. Cindro, I. Mandic, M. Mikuz, M. Milovanovic, M. Zavrtanik, K. Zagar, *Investigation of irradiated silicon detectors by edge-TCT*, IEEE Tractions on nuclear science, **57** (2010) 4.

109. E. Gaubas, T. Ceponis, V. Kalesinskas, *Currents induced by injected charge in junction detectors*, Sensors 13, 12295 (2013).

110. R. Smith, Semiconductors, 2nd ed. (Cambridge Univ. Press, London – New York, 1982).

111. Alkauskas, A.; McCluskey, M.D.; Van de Walle, C.G. Tutorial: Defects in semiconductors-combining experiment and theory. *J. Appl. Phys.* **2016**, *119*, 181101.

112. Kopylov, A.A.; Pikhtin, A.N. Effect of temperature on the optical-absorption spectra of deep centres in semiconductors. *Sov. Phys. Solid State* **1975**, *16*, 1200–1203.

113. Zangenberg, N.; Larsen, A.N. On-line DLTS investigations of vacancy related defects in low-temperature electron irradiated, boron-doped Si. *Appl. Phys. A* **2005**, *80*, 1081–1086, doi:10.1007/s00339-003-2358-3.

114. Makarenko, L.F.; Korshunov, F.P.; Lastovskii, S.B.; Murin, L.I.; Moll, M.; Pintilie, I. Formation and annealing of metastable (interstitial oxygen)-(interstitial carbon) complexes in n- and p-type silicon. *Semiconductors* **2014**, *48*, 1456–1462, doi:10.1134/s1063782614110141.

115. Pedersen, T.P.L.; Larsen, A.N.; Mesli, A. Carbon-related defects in proton-irradiated, n-type epitaxial Si1−xGex. *Appl. Phys. Lett.* **1999**, *75*, 4085–4087, doi:10.1063/1.125544.

116. Lastovsky, S.; Markevich, V.P.; Yakushevich, H.S.; Murin, L.I.; Krylov, V.P. Radiation-induced bistable centers with deep levels in silicon n^+-p structures. *Semiconductors* **2016**, *50*, 751–755, doi:10.1134/s1063782616060130.

117. Gaubas, E.; Čeponis, T.; Vaitkus, J. Impact of generation current on the evaluation of the depletion width in heavily irradiated Si detectors. *J. Appl. Phys.* **2011**, *110*, 033719, doi:10.1063/1.3619802.

118. Kolkovsky, V.I.; Mesli, A.; Dobaczewski, L.; Abrosimov, N.V.; Zytkiewicz, Z.R.; Peaker, A.R. Interaction of iron with the local environment in SiGe alloys investigated with Laplace transform deep level spectroscopy. *Phys. Rev. B* **2006**, *74*, 195204.

119. Mesli, A.; Kolkovsky, V.; Dobaczewski, L.; Larsen, A.N.; Abrosimov, N. Defects and impurities in SiGe: The effect of alloying. *Nucl. Instrum. Methods Phys. Res. Sect. B: Beam Interact. Mater. Atoms* **2006**, *253*, 154–161, doi:10.1016/j.nimb.2006.10.025.

120. Stubner, R.; Kolkovsky, V.; Weber, J.; Abrosimov, N.V. Carbon-hydrogen complexes in n- and p-type SiGe-alloys studied by Laplace deep level transient spectroscopy. *Solid State Phenom.* **2016**, *242*, 184–189.

121. Markevich, V.P.; Peaker, A.R.; Murin, L.I.; Abrosimov, N.V. Oxygen-related radiation-induced defects in SiGe alloys. *J. Physics: Condens. Matter* **2003**, *15*, S2835–S2842, doi:10.1088/0953-8984/15/39/008.

122. Markevich, V.P.; Peaker, A.R.; Coutinho, J.; Jones, R.; Torres, V.J.B.; Structure and properties of vacancy-oxygen complexes in Si1-xGex alloys. *Phys. Rev. B* **2004**, *69*, 125218.

123. Gaubas, E.; Ceponis, T.; Deveikis, L.; Meskauskaite, D.; Pavlov, J.; Rumbauskas, V.; Vaitkus, J.; Moll, M.; Ravotti, F. Anneal induced transformations of defects in hadron irradiated Si wafers and Schottky diodes. *Mater. Sci. Semicond. Process.* **2018**, *75*, 157–165, doi:10.1016/j.mssp.2017.11.035.

124. Ullan, M.; Diez, S.; Lozano, M.; Pellegrini, G.; Knoll, D.; Heinemann, B. Combined effect of bias and annealing in gamma and neutron radiation assurance tests of SiGe bipolar transistors for HEP applications. *Solid State Electron.* **2011**, *56*, 179–184, doi:10.1016/j.sse.2010.11.014.

125. Heinemann, B.; Rucker, H.; Barth, R.; Barwolf, F.; Drews, J.; Fischer, G.G.; Fox, A.; Fursenko, O.; Grabolla, T.; Herzel, F.; et al. SiGe HBT with fx/fmax of 505 GHz/720 GHz. In Proceedings of the 2016 IEEE International Electron Devices Meeting (IEDM); San Francisco, CA, USA, 3–7 December 2016.

126. Li, Y.; Li, J.; Du, J.; Han, J.; Xiang, Q.; Zhang, C. Influence of fast neutron and gamma irradiation on the thermoelectric properties of n-type and p-type SiGe alloy. *J. Nucl. Mater.* **2020**, *528*, 151856.

127. Pintilie, I.; Fretwurst, E.; Lindsrom, G.; Stahl, J. Second-order generation of point defects in gamma-irradiated float-zone silicon, an explanation for „type inversion“. *Appl. Phys. Lett.* **2003**, *82*, 2169–2171.

128. Lopez, P.; Aboy, M.; Munoz, I.; Santos, I.; Marques, L.A.; Fernandez-Martinez, P.; Ullan, M.; Pelaz, L. Atomistic simulations of acceptor removal in p-type Si irradited with neutrons. Nucl. Instrum. Methods Phys. Res. B **2022**, *512*, 42–48.

129. Nylandsted Larsen, A.; Bro Hansen, A.; Mesli, A. Irradiation induced defects in SiGe. *Mat. Sci.Eng. B* **2008**, *154–155*, 85–89.

130 Mamor, M.; Pipeleers, B.; Auret, F.D.; Vantomme, A. Defect production in strained p-type $Si_{1-x}Ge_x$ by Er implantation. *J. Appl. Phys.* **2011**, *109*, 013715.

131. Sadoh, T.; Fitrianto; Kunigami, M.; Kenjo, A.; Miyauchi, A.; Inoue, H.; Miyao, M. Thermal stability of B in poly-SiGe on SiON. *Mater. Sci. Eng.* **2005**, *275*, 91–98.

132. Bennett, N.S.; Ahn, C.; Cowern, N.E.B.; Pichler, P. Review of stress effects on dopant solubility in silicon and silicon-germanium layers. *Solid State Phenomena* **2010**, *156–158*, 173.

133. Besleaga, C.; Kuncser, A.; Nitescu, A.; Kramberger, G.; Moll, M.; Pintilie, I. Bistability of the BiOi complex and its implications on evaluating the "acceptor removal" process in p-type silicon. *Nucl. Instrum. Methods Phys. Res. Sect. A Accel. Spectrom. Detect. Assoc. Equip.* **2021**, *1017*, 165809.

134. Liao, C.; Fretwurst, E.; Garutti, E.; Schwandt, J.; Moll, M.; Himmerlich, A.; Gurimskaya, Y.; Pintilie, I.; Nitescu, A.; Li, Z.; et al. The boron-oxygen (BiOi) defect complex induced by irradiation with 23 GeV protons in p-type epitaxial silicon diodes. *IEEE Trans. Nucl. Sci.* **2021**.

135. Moll, M. Acceptor removal—Displacement damage effects involving the shallow acceptor doping of p-type silicon devices.

136. Zhu, J.; Liu, F.; Stringfellow, G.B.; Wei, S.-H. Strain-enhanced doping in semiconductors: Effects of dopant size and charge state. *Phys. Rev. Lett.* **2010**, *105*, 195503.

137. Mori, N. Electronic band structures of silicon-germanium (SiGe) alloys. In *Silicon-Germanium (SiGe) Nanostructures. Production, Properties and Application in Electronics*, 1st ed.; Shiraki, Y., Usami, N., Eds.; Woodhead Publishing: Sawston, UK, 2011; pp. 26–42.

138. Fadaly, E.M.T.; Dijkstra, A.; Suskert, J.R.; Ziss, D.; van Tilburg, M.A.J.; Mao, C.; Ren, Y.; van Lange, V.T.; Korzun, K.; Kolling, S.; et al.

Direct-bandgap emission from hexagonal Ge and SiGe alloys. *Nature* **2020**, *580*, 205–209.

139. Popescu, V.; Zunger, A. Effective band structure of random alloys. *Phys. Rev. Lett.* **2010**, *104*, 236403.

140. Jin, S.; Park, H.-H.; Luisier, M.; Choi, W.; Kim, J.; Lee, K.-H. Band-to-band tunneling in SiGe: Influence of alloys scattering. *IEEE Electron Device Lett.* **2017**, *38*, 422–425.

141. Gaubas E, Kazlauskas K, Tomašiūnas R, Vaitkus J and Žukauskas A 2004 Radiation-defect-dependent photoconductivity transients and photoluminescence in semi-insulating GaN *Appl. Phys. Lett.* **84** 5258.

142. Gaubas E, Kovalevskij V, Kadys A, Gaspariunas M, Mickevicius J, Jasiunas A, Remeikis V, Uleckas A, Tekorius A, Vaitkus J and Velicka A 2013 In situ variations of recombination characteristics in MOCVD grown GaN epi-layers during 1.7 MeV protons irradiation *Nucl. Instrum. Methods B* **307** 370–2.

143. Gaubas E, Brytavskyi I, Ceponis T, Jasiunas A, Kalesinskas V, Kovalevskij V, Meskauskaite D, Pavlov J, Remeikis V, Tamulaitis G and Tekorius A 2014 In situ variations of carrier decay and proton induced luminescence characteristics in polycrystalline CdS *J. Appl. Phys.* **115** 243507.

144. Polyakov A, Usikov A, Theys B, Smirnov N, Govorkov A, Jomard F, Shmidt N and Lundin W 2000 Effects of proton implantation on electrical and recombination properties of n-GaN *Solid. State. Electron.* **44** 1971–83.

145. D. Baltas and N.Zamboglou. 2D and 3D planning in brachytherapy. New Technologies in Radiation Oncology (Editors: W. Schlegel, T. Bortfeld, A.-L.Grosu), Springer , pp 237-254, https://doi.org/10.1007/3-540-29999-8, Springer-Verlag Berlin Heidelberg 2006, ISBN 978-3-540-29999-8.

146. P.Pittet, P.Jalade, L.Gindraux, P.Guiral, R.Wang, J.-M.Galvan, G.-N.Lu. DoRGaN: development of quality assurance and quality control systems for high dose rate brachytherapy based on GaN dosimetry probes. IRBM 39 (2018) 279-290.

147. M.Carrara, D.Cutajar, S.Alnaghy, A.Espinoza, A.Romanyukha, S.Pressila, C.Tenconi, A.Cerrotta, C.Fallai, M.-Safavi-Naeini, M. Petasecca, A.Kejda, M. Lerch, S. Corde, M.Jackson, A.Howie, J.Bucci, A.B.Rosenfeld. Semiconductor real-time quality assurance dosimetry in brachytherapy. Brachytherapy, 17 (2018) 133-145.

148. J.Cherpak, IJ.E.Cygler, C.E, G.Perry. Real-time measurement of urethral dose and position during permanent seed implantation for prostate brachytherapy. Brachytherapy, 13 (2014) 169-177.

149. A. M. Franz, T.Haidegger, W.Birkfellner, K. Cleary, T. M. Peters, and L. Maier-Hein. Electromagnetic tracking in medicine—a review of technology, validation, and applications. IEEE TRANSACTIONS ON MEDICAL IMAGING, 33 (2014) 1702-1725.

150. K.Tanderup, S.Beddar, C.E.Andersen, G.Kertzscher, J.Cygler. *In vivo* dosimetry in brachytherapy. Med. Phys. 40 (2013) 070902-01 - 070902-15.

151. M.J.Rivard, B.M.Coursey, L.A.DeWerd, W.F.Hanson, M.S.Huq, G.S.Ibbott, M.G.Mitch, R.Nath, J.F.Williamson. Update of AAPM Task Group No. 43 Report: A revised AAPM protocol for brachytherapy dose calculations. Med. Phys. 31 (2004) 633-674.

152. Heron's formula – Wikipedia, https://en.wikipedia.org/wiki/Heron%27s_formula, accessed on 2021-10-18.

SANTRAUKA

Kornelijus PŪKAS

Dozimetrijos technologijos aukštųjų energijų fizikos ir radiacinės medicinos taikymams

Aktualiems modernios aukštųjų energijų fizikos ir radiacinės medicinos taikymams reikia naujos kartos didelio jautrio ir radiacinio atsparumo, didelės spartos sensorių su vidinio stiprinimo struktūra. Pagrindine problema yra radiacinių defektų nevaldomas susidarymas, kuris keičia krūvininkų rekombinacijos/prilipimo bei sklaidos centrų parametrus. Todėl detektorių fizikoje telkiamos didelės pastangos radiacinių pažaidų mechanizmų atskleidimui ir jų sąsajų su sensorių fizikinių charakteristikų nepageidaujamais pokyčiais. Viena iš krypčių šioms problemoms spręsti būtų naujų, radiacijai atsparių medžiagų paieška. GaN monokristaliniai dariniai ir SiGe kietieji tirpalai yra vienos perspektyviausių medžiagų didelio įtėkio spinduliuočių detektavimui. Ga bei Ge sunkiųjų elementų įtraukimas į šių medžiagų sudėtį ir yra vienas faktorių radiaciniam atsparumui didinti. GaN be to yra perspektyvus dvigubo, elektrinio ir optinio atsako sinchroniniam registravimui. Visgi, tik vidutinė GaN bei SiGe darinių auginimo technologijų branda neleidžia užtikrinti defektų sumažinimo iki elektronikos lygio technologinių reikmių. Iš kitos pusės, nepakankamos fundamentinės žinios apie priemaišų sąveikas su radiaciniais defektais neleidžia suvokti legirantų de-aktyvavimo procesų ir terminiais apdorojimais valdyti detektorių funkcines savybes. Iš kitos pusės, alternatyva radiacinių defektų neleistiniems kitimams galėtų būti inovacijos keičiant sensorių struktūrą, kai krūvininkų nykimą galima kompensuoti sukuriant papildomo vidinio stiprinimo sluoksnius matuojamo signalo sustiprinimui iki matuojamo dydžio. Šie sensorių struktūros modifikavimai leidžia kartu spartinti sensorių atsaką. Daliai paminėtų problemų sprendimui ir yra skirtas šis tyrimų ciklas. Papildomai specifinių charakteristikų matavimams teko tobulinti ir matavimų technologijas. Visos šios pastangos buvo skirtos praktinių technologijų sukūrimui, -būtent, naujos kartos LGAD (Low Gain Avalanche Diode) detektorių kūrimui vykdant CERN RD50 programą bei brachiterapijos planavimo verifikavo technologijos sukūrimui ir įdiegimui radiacinės medicinos taikymams Nacionaliniame Vėžio Institute. Paminėtų fundamentinių tyrimų sukurtos žinios ir buvo pasitelktos atrenkant detektorius brachiterapijos zondams.

Šio **darbo uždaviniai** buvo tokie:

- optimizuoti SiGe darinių iškaitinimo režimus radiacinių ir technologinių defektų transformacijoms valdyti varijuojant Ge elemento koncentraciją SiGe kietuosiuose tirpaluose ir keičiant taškinių defektų kompleksų būsenas pageidautinų legirantų aktyvumo stabilizavimui;
- surasti efektyvaus GaN kristalų legiravimo (Mg, Mn ,Fe) priemaišomis režimus siekiant suvaldyti savitųjų technologinių defektų pasireiškimą sensorių funkcinėse charakteristikose ir sukurti tinkamų parametrų GaN darinius;
- surasti LGAD detektorių sluoksnių formavimo struktūros optimalius sprendimus siekiant padidinti atsako dydį ir spartą;
- patobulinti ir pritaikyti impulsines metodikas defektų dinaminei spektroskopijai SiGe bei GaN dariniuose radiacinių defektų sąveikų įvertinimui;
- modernių radiacijos detektorių brachiterapijai atrinkimas ir programinės įrangos vienalaikiam radionuklidų lokalizacijos ir dozinių parametrų kontrolei sukūrimas.

Šio **darbo mokslinį naujumą** sudaro sukurtos žinios apie radiacinių defektų ir legirantų sąveikas bei pageidautinų legirantų aktyvumo stabilizavimas sukuriant lokalius įtempimų laukus įvedant Ge atomus į Si gardelę. Technologinį naujumą sudaro Mn bei Mg priemaišų įvedimas į ammono technologijos GaN medžiagas efektyvių tūrinių spinduliuočių detektorių formavimui. Mokslinį naujumą taip pat pagrindžia detektorių srovių sandų modeliai siekiant įvertinti krūvininkų transporto bei rekombinacijos režimų kitimus modifikuojant detektorių atsako charakteristikas. Metodinį naujumą sudaro sinchroninio radionuklidų lokalizacijos bei sukauptos dozės profiliavimo technologijos bei įrangos sukūrimas radiacinės medicinos taikymams.

Praktinė šio darbo svarba sietina su taikymo perspektyvų ir sričių įvertinimu sukuriant tūrinius ir plonasluoksnius SiGe bei GaN radiacijos sensorius. Technologinę reikšmę turi ir tikslingo defektų transformacijų valdymas terminių apdorojimų/iškaitinimų būdu sukuriant tinkamus taškinių defektų kompleksų legirantų stabilizavimui. Technologines inovacijas sudaro ir žinios apie Mn bei Mg priemaišų įterpimą ammono-technologijos GaN elektrinio laidumo charakteristikų ir atsako spartos valdymui. Darbe parodyta modelinių ir eksperimentinių charakteristikų derinimo svarba kuriant tinkamos struktūros LGAD sensorius. Praktinę reikšmę sudaro ir brachiterapijos verifikavimo technologijos įdiegimas NVI.

Šios **disertacinio darbo ginamieji teiginiai** būtų tokie:

1. Prilipimo centrų koncentracija $Si_{0.95}Ge_{0.05}$ detektoriuose po apšvitos elektronų pluošteliu yra 1.8 karto didesnė, negu tokiomis pat sąlygomis

paveiktų Si sensorių, dėl 15 meV seklesnių centrų susidarymo. Tuo pačiu, įterptinių anglies –deguonies metastabilūs kompleksai (C_iO_i *), iškaitinus 125 C temperatūroje 5 MeV elektronais apšvitintus SiGe darinius, transformuojasi į stabilius taškinių įterpinių atomų centrus (C_iO_i), o radiacinių centrų terminės aktyvacijos energija slenkasi į mažesnių verčių sparną, didėjant Ge elemento kiekiui SiGe kietajame tirpale.

2. Krūvininkų rekombinacijos trukmė, nulemta radiacinių defektų po SiGe darinių apšvitos stabdomais protonais, ilgėja didėjant Ge kiekiui kietajame tirpale dėl akceptorinių radiacinių defektų susidarymo p-laidumo medžiagoje.

3. Generacinės srovės sando išskyrimas BELIV kinetikose leidžia įvertinti terminės emisijos trukmę ir aktyvacijos energijos vertes E_{tr}.

4. Bistabilus įterptinio boro-deguonies (B_iO_i) kompleksas yra vyraujanti šalutinių krūvininkų gaudyklė *p*-tipo $Si_{1-x}Ge_x$ medžiagose, kuri nulemia boro legirantų de-aktyvavimą ir radiacinio detektorių atsparumo degradaciją. Boru legiruotieji $Si_{0.95}Ge_{0.05}$ dariniai yra atsparesni legirantų radiacinei de-aktyvacijai palyginant su boru legiruotais Si ir$Si_{0.99}Ge_{0.01}$darinias. B_iO_i komplekso vaidmuo $Si_{0.95}Ge_{0.05}$ darinio radiacinio atsparumo charakteristikose yra mažesnis dėl lokalių įtempimų sukurtų įterpiant daugiau Ge elemento. Tai gali pagrįsti radiacinio SiGe darinių atsparumo didinimo technologiją, spinduliuote transformuojantis B_iO_i kompleksams modifikuojant lokalius įtempimus Ge komponentu.

Autoriaus indėlis:

Vykdant šį tyrimų ciklą disertacijos autorius išanalizavo krūvininkų prilipimo ir rekombinacijos charakteristikas kombinuojant įvairius matavimo metodus. Autorius modeliavo ir eksperimentiškais ištyrė voltamperines, voltfaradines ir impulsinių srovių kinetikų charakteristikas, dalinai analizavo DLTS charakteristikas pin ir LGAD Si bei SiGe dariniuose. Autorius atliko daugumą disertacijoje aprašytų tyrimų. Didžiuma rezultatų buvo aprobuota nacionalinės konferencijos ir doktorantų konferencijų pranešimuose.

Kai kurie medžiagotyros eksperimentai buvo įvykdyti bendradarbiaujant su FNI doktorantais D. Meškauskaite ir L. Deveikiu. DLTS tyrimai įgyvendinti drauge su dr. J. Pavlov. K. Pūkas sukūrė programinę įrangą brachiterapijos verifikavimo technologijai. Autorius drauge su konsultantu dr. T. Čeponiu ir dr. V. Rumbausku tobulino ir diegė įrangą brachiterapijos technologijai. Visa tyrimų ideologija, rezultatų analizė ir publikacijų rankraščiai buvo ruošiami su doktorantūros vadovu prof. habil. dr. E. Gaubu.

Publikacijų sąrašą sudaro:

- **straipsniai** moksliniuose žurnaluose:

A1. J. Pavlov, T. Ceponis, **K.Pukas**, L.Makarenko, and E. Gaubas,. 5.5 MeV Electron irradiation-induced transformation of minority carrier traps in p-type Si and $Si_{1-x}Ge_x$ alloys. Materials 2022, 15, 1861. https://doi.org/10.3390/ma15051861.

A2. T. Ceponis, L. Deveikis, S. Lastovskii, L. Makarenko, J. Pavlov, **K. Pukas**, V. Rumbauskas, E. Gaubas, *Transient electrical and optical characteristics of electron and proton irradiated SiGe detectors*, Sensors **20** (2020) 6884.

A3. T. Ceponis, S. Lastovskii, L. Makarenko, J. Pavlov, **K. Pukas**, E. Gaubas, *Study of radiation-induced defects in p-type $Si_{1-x}Ge_x$ diodes before and after annealing*, Materials **13** (2020) 5684.

A4. E. Gaubas, T. Ceponis, L. Deveikis, D. Meskauskaite, S. Miasojedovas, J. Mickevicius, J. Pavlov, **K. Pukas**, J. Vaitkus, M. Velicka, M. Zajac, and R. Kucharski, *Study of neutron irradiated structures of ammonothermal GaN*, J. Phys. D: Appl. Phys. 50 (2017) 135102.

- **EPO patentas**:

EPO-1 E.Gaubas, T.Ceponis, **K.Pukas**, V.Rumbauskas, M.Uzgirytė, J.Venius, K.Akelaitis, A.Cicinas, *System and method for brachytherapy procedure planning and verification*, Application for EU patent V83-82 EP

- **pranešimai doktorantų konferencijose** ir mokyklose:

P1. **K.Pukas**, T. Ceponis, E. Gaubas; TCAD simulations of p-type Si and Si(1-x)Ge(x) low gain avalanche detector characteristics; Open Readings 2021; March 16-19, Vilnius (nuotolinė).

P2. **K.Pukas**, T. Čeponis, E. Gaubas; Comparison of Simulated p-type Si1−xGex and Si LGAD with Traps; Advanced materials and Technologies 2021, August 23-27, Palanga, Lietuva.

P3. **K. Pukas**, L.Dundulis, J.Vyšniauskas, E.Gaubas, TCAD simulations of functional characteristics for silicon low gain avalanche detectors, LNFK, 2018, Vilnius.

Disertacijos aprašą sudaro penki skyriai.

Pirmame skyriuje yra pateiktas įvadas nusakant bendras disertacijos charakteristikas, aptariant tyrimų aktualumą, darbo tikslą bei uždavinius, atskleidžiant šio darbo mokslinę ir praktinę svarbą. Įvade suformuluoti 4-i disertacijos ginamieji teiginiai. Čia taip pat nurodytas disertanto autorinis indėlis ir publikacijų sąrašas, kurį sudaro 4-straipniai WOS moksliniuose žurnaluose, viena EPO patento paraiška bei trys pranešimai konferencijose.

Antrame skyriuje aptarta SiGe bei GaN medžiagų moderniems spinduliuočių detektoriams charakteristikų aktualių tyrimų motyvacija. Pirmame paragrafe pateikta spinduliuotėmis indukuotų sąveikų ir radiacinės pažaidos mechanizmų trumpa apžvalga. Antrame paragrafe aptarta priemaišų

ir defektų SiGe dariniuose įtaka funkcinių šių medžiagų charakteristikų formavimui. Trečiame skirsnyje apžvelgti defektų GaN kristaluose spektrai ir GaN detektorių funkcinės charakteristikos.

Trečiame skyriuje pateiktas darbe pasitelktų **matavimo metodų pagrindimas**. Čia aptarti voltameperinių (I-V) bei voltafaradinių (C-V) charakteristikų matavimo režimai, elektrinių medžiagos parametrų įvertinimo galimybės. Trumpai pagrįsta giliųjų lygmenų talpinės spektroskopijos (DLTS) metodika bei įranga ir papildanti impulsinė barjerinės talpos (BELIV) analizės metodika. Aptarta ir mikrobangomis zonduojamo fotolaidumo kinetikų (MW-PC) metodika ir įranga krūvininkų rekombinacijos, prilipimo trukmių matavimui. Detektorių charakterizavimui svarbūs srovių analizės metodai. Todėl trečiame skyriuje įvairiapusiškai aptarti nenuostoviųjų srovių kinetikų (TCT) matavimo ir srovės sandų iškyrimo būdai, medžiagų ir detektorių funkcinių parametrų įvertinimui. Spektrinių defektų charakteristikų įvertinimui šiame darbe buvo pasitelkta nuostoviosios ir impulsinės fotojonizacjos (PIS) metodas, ir šiame disertacijos skyriuje aptarti spektrinių fotojonizacijos charakteristikų analizės ypatumai. Galiausiai trumpai aptarta Synopsys TCAD platforma detektorių struktūroms ir pin bei LGAD detektorių charakteristikų įvairiapusiams modeliavimams.

Ketvirtame skyriuje pateikti ir aptarti esminiai eksperimentinių tyrimų rezultatai. Pirmame paragrafe aptartos nenuostovios elektrinės charakteristikos, DLTS metodu apibūdinančios pagrindinių krūvininkų gaudyklių SiGe detektoriuose kaitą po apšvitos elektronų pluošteliu. Aptiktas 7-ių gaudyklių spektras ir C_iO_i gaudyklių transformacijos iš metastabilių į stabilias būsenas. Išnagrinėta gaudyklių terminės aktyvacijos energijų kaita varijuojant Ge kiekį SiGe dariniuose. Antrame skirsnyje aptartos elektronų pluošteliu indukuotos šalutinių krūvininkų gaudyklių transformacijos p-laidumo Si bei SiGe dariniuose. DLTS metodu įvertintos centrų terminės aktyvacijos energijos ir identifikuota gaudyklių prigimtis. Iš BELIV generacinės srovės sando temperatūrinių kitimų generacinė krūvininkų gyvavimo trukmė. Trečiame paragrafe pateikta elektrinių ir optinių charakteristikų palyginamoji analizė elektronais ir protonais apšvitintuose Si ir SiGe dariniuose. Buvo sudaryta konfiguracinė diagrama nusakanti tų pačių centrų dalyvavimą fotojonizacijos ir terminės aktyvacijos procesuose. Ketvirtame skirsnyje pateiktos ir aptartos ammono technologijos GaN, apšvitinto branduolinio reaktoriaus neutronais, rekombinacinės ir scintiliacinės charakteristikos, siekiant optimizuoti medžiagų parinkimą tūrinių GaN dvigubo atsako sensorių gamybai. Penktame šio skyriaus paragrafe aptarti pin ir LGAD detektorių charakteristikų TCAD modeliavimo ir eksperimentinių tyrimų rezultatai. Šio skyriaus rezultatų pagrindu yra

suformuluoti esminiai ginamieji teiginiai apie C_iO_i centrų transformacijas temperatūrinių apdorojimų pasekoje, apie bistabilius įterptinio boro-deguonies B_iO_i kompleksus ir jų raidos priklausomybę nuo Ge kiekio SiGe kietuosiuose tirpaluose. Taip pat keletas išvadų suformuluota šio skyriaus rezultatų pagrindu apie I_2O kompleksus, deguonies –vakansijos VO ir boro-deguonies B_iO_i kompleksus SiGe dariniuose, kintant Ge kiekiui, apie MW-PC, PL and CCE charakteristikų koreliacijas kintant neutronų įtėkiui, kai ammono-technologijos GaN dariniai apšvitinami didelio įtėkio branduolinio reaktoriaus neutronais.

Penktame skyriuje trumpai aptarti brachiterapijos technologijos ir įrangos kūrimo bei patentavimo esminiai bruožai. Pirmame paragrafe apžvelgtos brachiterapijos planavimo verifikacijos problemos ir tokios technologijos reikmė. Antrame paragrafe aptarta bandomosios įrangos struktūra momentiškai registruojant radionuklido pozicionavimą erdvėje ir apšvitos ekspoziciją. Trečiame paragrafe aptarti radioaktyvių emiterių pozicionavimo kontrolės bei dozimetrinio skenavimo principai. Čia pateikiamos kalibracinių matavimų ir testų rezultatų iliustracijos. Ketvirtame paragrafe pateikti matematiniai algoritmai, pasitelkiami kuriant spartaus dozimetrijos plano verifikavimo programinę įrangą prototipinių instrumentų bei brachiterapijos technologijos įdiegimams.

Disertacijos aprašo pabaigoje reziumuojami pagrindiniai tyrimų rezultatai pateikiant 12-ką išvadų.

Disertacija baigiama 152 – pozicijų literatūros nuorodų sąrašu.

CURRICULUM VITAE

Kornelijus Pūkas
Kornelijus.pukas@tmi.vu.lt
+37062392490
Vilnius, Lithuania

Education

Bachelor of Physics, Vilnius University (2013 – 2017).

Master of Materials and Technology of Optoelectronics, Vilnius University (2017 – 2019).

Experience

Technician - group of radiation defects and detectors, Vilnius University Faculty of Physics Institute of Photonics and Nanotechnology (2015 – 2017).

Engineer – group of radiation defects and detectors, Vilnius University Faculty of Physics Institute of Photonics and Nanotechnology (2015 – 2020).

Junior researcher – group of photoelectric phenomena, Vilnius University Faculty of Physics Institute of Photonics and Nanotechnology (2020 – present).

NOTES

Vilniaus universiteto leidykla
Saulėtekio al. 9, III rūmai, LT-10222 Vilnius
El. p. info@leidykla.vu.lt, www.leidykla.vu.lt
bookshop.vu.lt, journals.vu.lt
Tiražas 25 egz.